5-2023

Single-Mode Distributed-Feedback Lasing In Coupled Dissimilar Photonic Waveguides

Bryce A. Tennant
bat3289@rit.edu

Recommended Citation

Tennant, Bryce A., "Single-Mode Distributed-Feedback Lasing In Coupled Dissimilar Photonic Waveguides" (2023). Thesis. Rochester Institute of Technology. Accessed from

Single-Mode Distributed-Feedback Lasing In Coupled Dissimilar Photonic Waveguides

by

Bryce A. Tennant

A Dissertation Submitted in Partial Fulfillment of the
Requirements for the Degree of Doctor of Philosophy in Microsystems Engineering

Supervised by

Drew N. Maywar, PhD

Microsystems Engineering PhD Program

Kate Gleason College of Engineering

Rochester Institute of Technology

Rochester, New York

May, 2023

Single-Mode Distributed-Feedback Lasing In Coupled Dissimilar Photonic Waveguides

by

Bryce A. Tennant

Committee Approval:

We, the undersigned committee members, certify that we have advised and/or supervised the candidate on the work described in this dissertation. We further certify that we have reviewed the dissertation manuscript and approve it in partial fulfillment of the requirements of the degree of Doctor of Philosophy in Engineering.

Dr. Drew Maywar Date
Dissertation Advisor

Dr. Mishkat Bhattacharya Date
Dissertation Committee Member

Dr. Parsian K. Mohseni Date
Dissertation Committee Member

Dr. Jing Zhang Date
Dissertation Committee Member

Dr. Drew Maywar Date
Dissertation Defense Chairperson

Certified by:

Dr. Stefan Preble Date
Ph.D. Program Director, Microsystems Engineering

Acknowledgments

Firstly, I would like to express my deepest gratitude to my advisor, Professor Drew Maywar. I simply could not have had a better guide and mentor through this incredible and amazing campaign. His scientific rigor, attention to detail, master of process, laser focus, and passion for teaching is second to none. I look forward to the many years of continued collaboration, friendship, and casting ahead.

For decades now, my mother (and number one advocate) has spent countless hours engaging, asking great questions, and listening to me ramble on and on about the beauty of mathematics and physics. My father, who inspired me to get into the field way back in his days at Digital Equipment Corporation, has taken a deep technical interest in my work and is always curious as to where I will be taking it next. I thank you and love you both for your support through this entire endeavor.

I must thank my extended family at Maria's Mexican, who have all been a huge constant in my life for so many years now. I love ending every week with them and am so grateful they have each become such close and dear friends. Many thanks and much love to Stella, Heiko, Stephany, Heiko Karl, Grete, Don Julio, V, Valerie, Iris, and Gloria.

I would like to recognize all my friends who have stood by and remained constant even when I have repeatedly flaked out or been overly absorbed in my work. Specifically, I would like to thank both Joe Shaver and Chris Page, who have been dear friends for so many years now. The have both kept me grounded, inspired, somewhat sane, and, most importantly, always smiling and laughing.

My gratitude to L3Harris for their continued flexibility over the past several years. In particular, many thanks to Jon Leombrone and Dana Mehnert for their patience and support as I worked hard to balance my available capacity between L3Harris and my degree. They recognized and respected my passion for photonics research, which allowed to focus deeply on the work I wanted to do.

Finally, none of my work would be possible without the unbelievable love, support, and patience from my wife and best friend, Jess; I love you so much. Jess was present, constant, supportive, and understanding through the entire journey. She worked tirelessly, *every single day*, to make sure I had the energy, space, time, and confidence to complete my research. This dissertation is, without question, as much hers as it is mine. I am forever grateful to her and her constant unwavering love, inspiration, and dedication.

How do you want to do this?

Curriculum Vitae

The author, Bryce A. Tennant, completed his undergraduate study in electrical engineering at the Rochester Institute of Technology (RIT) from 1992 to 1997. He started with Harris Corporation in 1996 as a software engineer and continued with the company through 2013 where he ended his term as the senior-principal signal-processing and acoustics architect. During this time, the author completed his Master's degree in electrical engineering at RIT in 2003 with his thesis on orthogonal M-band bandlimited wavelet transform basis functions.

In 2011, the author became Chief Technology Officer for Precision Optical Transceivers, located in Rochester New York. In 2015, he co-founded Veluxsys Inc., focusing on integrated photonics for Department of Defense (DoD) applications. In 2016, he started his PhD at RIT under his advisor, Dr. Drew Maywar.

In 2018, the author was recruited by L3Harris Corporation to be the Director of Strategy, Growth, and Innovations, where he is responsible for their research portfolio, rapid-prototyping efforts, and strategic development of nascent DoD opportunities. Furthermore, the author is a technical advisor for L3Harris's venture-capital arm, Shield Capital, where he evaluates small businesses and start-ups seeking collaborative alignment with the organization.

Peer-reviewed journal papers based on PhD research:

- Bryce A Tennant and Drew N Maywar, "Analytical model of direct-Bragg, exchange-Bragg, and evanescent coupling in a dual-waveguide structure and its application to single-mode lasing," submitted to the Journal of the Optical Society of America B (Optical Physics)
- Bryce A Tennant and Drew N Maywar, "Single-mode distributed feedback lasing using photonic bandgaps to suppress degenerate modes," Optics Letters, vol. 47, no. 13, pp. 3367–3370, 2022
- Bryce A Tennant, Riffat Ara, Abdulaziz Atwiri, Govind P Agrawal, Natalia M Litchinitser, and Drew N Maywar, "Distributed feedback lasing based on a negative-index metamaterial waveguide," Optics Letters, Vol. 44, no. 18, pp. 4586–4589, 2019

International conference presentations based on PhD research:

- Bryce A Tennant, Govind P Agrawal, Natalia M Litchinitser, and Drew N Maywar, "Metamaterial-enabled distributed feedback lasing without a diffraction grating," CLEO QELS — Fundamental Science, 2020

Abstract

Distributed-feedback (DFB) lasers support a wide range of applications including fiber-optic and free-space optical communications, sensing and measurement, military warfare, and manufacturing and metrology. The desire for a reduction in size, weight, power, and cost (SWAP-C) for each of these applications continues to aggressively drive integrated- and silicon-photonic circuit development. Since DFB lasers based on uniform refractive-index diffraction gratings are naturally dual-mode, a variety of techniques have been introduced to impose single-mode operation, including the currently ubiquitous $\lambda/4$-grating phase-shift technique. This grating phase shift, however, creates an undesirable peaky-power profile within the laser cavity resulting in nonlinear behavior ultimately limiting single-mode operation above threshold.

Seeking to specifically address the limitations associated with $\lambda/4$-phase shifted lasers, this dissertation introduces the following *three* scientific advancements:

1. Introduces two novel single-mode DFB lasing concepts based on new physical principles
2. Derives parameterized mathematical models and their closed-form analytic solutions for each concept
3. Predicts excellent lasing performance at threshold for one lasing concept while avoiding the detrimental issues associated with a peaky-power profile

One of the two single-mode DFB lasing concepts places a passive photonic waveguide in proximity to a uniform-grating DFB lasing structure to form direct-Bragg coupling, exchange-Bragg coupling, and evanescent coupling among the optical modes of the structure's two waveguides. Waveguide loss, gain, wavenumbers, and the semiconductor nonlinearity along with the lasing structure's coupling coefficients are the fundamental quantities of the structure. The waveguide-wavenumber detuning is used to position the exchange-Bragg photonic bandgap (PBG), suppressing the degenerate mode associated with the active-waveguide direct-Bragg PBG resulting in single-mode lasing.

The second introduced single-mode DFB lasing concept makes use of a negative-index material (NIM) waveguide placed in proximity to an active positive-index material (PIM) waveguide. The electric field in the NIM waveguide has a Poynting vector oriented in the direction opposite to its wave vector and, when evanescently coupled to the PIM waveguide, yields distributed feedback and an associated PBG without using a diffraction grating. Unlike the uniform-grating DFB laser, the NIM-PIM laser has a mode spectrum defined by the difference in waveguide wavenumbers, yielding single-mode operation for waveguides whose wavenumbers never match.

A set of newly introduced coupled-mode equations (CMEs) whose solutions generate closed-form parameterized analytical expressions describe each lasing concept and capture structure behaviors. The fourth-order uniform-grating-based lasing structure CMEs are solved using a custom developed mathematical method whereas, solutions for the second-order metamaterial-based lasing structure CMEs are arrived at using traditional eigenvalue-analysis techniques. For both structures, the coupled-mode equations and derived solutions are entirely new to the literature.

The uniform-grating based lasing solution predicts a peak gain margin of $\alpha L = 1.05$ and associated longitudinal power flatness of $F = 0.017$, surpassing the performance of the industry-standard $\lambda/4$-shifted DFB laser of maximum $\alpha L = 0.735$ with the associated longitudinal power flatness of $F = 0.215$. Moreover, this dissertation predicts that high-performance single-mode lasing occurs in spite of the introduction of evanescent coupling and, in some cases, marginal amounts can actually help to improve upon the longitudinal power flatness. The impact of exchange-Bragg coupling and secondary-lasing mode competition is also revealed and mitigated. The required dual waveguide geometry of the lasing structure is compelling for both III-V and heterogeneous III-V-on-silicon devices.

The predicted performance motivates further research of these novel lasing concepts while the established mathematical models are tools to aid in this future work.

Table of Contents

List of Tables

List of Figures

1. Introduction

1.1 Motivation and Background

1.1.1 Applications & Market

Fiber-Optic Communications

Single-mode distributed feedback (DFB) lasers are the primary light source used in fiber-optic networks forming the backbone of modern internet communications. These fiber-optic cables interconnect network data devices and can be as short as a couple meters to connect adjacent rack-mounted switches to as long as tens of kilometers traversing oceans or circumnavigating continents [1], [2]. The single-mode laser is included in the transmit optical sub-assembly (TOSA) of an optical transceiver and, when coupled to a single-mode fiber, can support commercially available data-rates as high as 400 gigabits per second (Gbps) on a single wavelength [3]. Multiple laser wavelengths can be supported on a single optical fiber, further increasing the data capacity for each wavelength added.

Modern semiconductor processes are used to create the features of DFB lasers including active waveguides, which provide for optical gain, and diffraction gratings, which provide the required optical feedback [4]–[7]. DFB lasers can be packaged as stand-alone devices or included directly onto photonic-integrated circuits through micro-packing [8], [9], flip-chip integration [10], [11], wafer bonding [12]–[14], direct or molecular bonding [15], [16], backside integration [17], [18], or, recently, using transfer-printing techniques [19]–[21].

Sensing and Measurement

Touchless measurement techniques determine the time of flight between a light pulse emitted by a laser and its received reflected power to accurately measure the distance to an objects surface. These techniques aid in the measurement of surface roughness, film thickness, defect detection, vibration distortion, and surface topography to accuracy of less than a nanometer [22]. This time of arrival method forms the basis for light detection and ranging (LIDAR) systems capable of performing 2D and 3D map generation. LIDAR systems are not only used as tools for terrestrial mapping and planing but also for precision navigation and timing (PNT) in automotive and robotic applications where they either augment GPS based systems or act as an alternate in GPS denied environments [23].

A single mode laser can also be used to detect vibrations, pressure changes, temperature changes, and other dynamics in mechanical structures when passed through a Bragg fiber. Periodic diffraction gratings within the optical fiber create reflections along the length of the fiber. Laser pulses traveling along these Bragg fibers create a pattern of expected reflections under a baseline condition. As the baseline condition changes, the reflection timing and spectrum also changes. When correlated to an environmental parameter of interest, these reflections may provide details about system dynamics. Such fibers are commonly used in aircraft to determine bend distribution or even rotation along the length of the fuselage and wings [24].

Military Warfare

Single-mode lasers provide the light source for free-space optical (FSO) communications systems. FSO is most commonly used in commercial low-earth orbit (LEO) satellite networks such as Starlink or Kuiper. Lasers are pointed and tracked using a mechanical gimbal system from one satellite to another creating a network of optical space interconnects. The department of defence (DoD) supports highly specialized and classified FSO systems connecting multiple satellites, aircraft, ground stations, and other transmitter/receivers for command, control, communications, computers, intelligence, surveillance, and reconnaissance (C4ISR) applications [25].

Military targeting solutions rely on lasers to target and mark and adversarial asset with a pulse coded laser for a tracking munition to lock and destroy. Laser targeted bombs (LTBs) and other precision-guided munitions are accurate to areas less than five meters due to the point precision nature of these targeting systems [26]. Laser-illumination devices are used in concert with night-vision goggles to illuminate a target area for improved optical stand-off. A illumination laser, operating at a wavelength which is not visible to the human eye but is detectable by highly sensitive night-vision equipment, can be used to scan and light up areas without combative forces being aware. These same laser wavelengths are used in military-grade precision-targeting range-finding equipment to calculate the distance to an adversarial target for accurate positioning of ballistic and mortar fire.

Silicon Photonics

Silicon photonics, the integrated-photonic circuit development process using a traditional CMOS manufacturing processes and materials, has continued to demonstrate significant promise for complicated and compact photonic solutions. Because these integrated-photonic circuits are based off well-understood silicon-based process-design kits and manufacturing tools, they provide promise for a reduction in size, weight, power, and cost of final product offerings through wafer-level production and CMOS co-integration [27]. The primary limiter for large scale silicon-photonic adoption remains to be the complexity, cost, and yield associated with laser integration. As silicon is an indirect-bandgap material and is not capable of optical gain, integration of external light sources or heterogeneous integration, that is III-V on silicon based approaches, need to be considered [28]. Each embedment option still faces many challenges, remain at a low technology-readiness level (TRL), and are not suitable for high-volume commercial production where economic scale can be fully realized [29], [30].

The market demand for high-quality single-mode lasers and the need for effective embedment of these light sources drives research in novel lasing structures, materials, and manufacturing processes. Characterizing the fundamental behaviors of a lasing structure under variable quantities is paramount to the success of a structure's performance and, ultimately, its integration. As the demand for on-chip lasers continues to increase, novel lasing structures which compliment established manufacturing processes and seek to address integration and performance limitations will become attractive to the industry.

1.1.2 Modeling

Fundamental physics and mathematical models provide for a conceptual understanding of new lasing structures and present a foundation from which basic requirements can be derived. Proper physical models result in parameterized closed-form mathematical solutions describing lasing behaviors through relevant and controllable quantities. Such models and solutions can predict and optimize electromagnetic fields, longitudinal power profiles, lasing conditions, and other important at-threshold or above-threshold behaviors using a parameter-driven analysis which directly correlates to structure quantities. These closed-form mathematical models present lasing behaviors in a compact language which is accessible for both direct and clear understanding.

Finite-difference time domain (FDTD) modeling, experimental methods, and system integration should ideally all be built upon a closed-form predictive analytical model rooting results in the structure physics. Executing higher-level simulation or prototyping before a mathematical model is developed and understood can result in an open-loop iterative development process not grounded in expectation. Developing and maintaining a mathematical model will ultimately accelerate the adoption of new lasing structures for standalone and integrated-photonic applications.

In recent years, finite-difference time domain (FDTD) simulation methods have become more prevalent due to increased compute capability and robust, accessible, commercially-available software-modeling applications [31]. These methods have proven to be very powerful and yield meaningful empirical results, even for highly complicated photonic structures. The widespread use of FDTD simulation methods and their ability to allow for rapid digital prototyping has dominated publications over the past couple decades [31]–[33], making the more rigours closed-form modeling based approaches, such as coupled-mode equations (CMEs), fewer and further between. As powerful as modern FDTD simulation methods are, they do not provide for a deep parameter-based physical understanding of novel structures and, instead, rely on iterative design methodologies which tend to abstract results from the underlying mathematical physical principles.

1.1.3 DFB Lasing

Many seminal works in DFB lasers utilize CMEs to mathematically model optical-mode interactions, ultimately generating the structure's electric-field expressions [4], [5], [34]. These field expressions allow for the development of longitudinal-power profiles, transmittivity and reflectivity expressions, lasing-threshold calculations, single-mode operation expectations, and nonlinear semiconductor-gain-based behaviors such as spatial-hole burning [35].

The pioneering work on DFB lasers use a uniform grating reflector to generate direct-Bragg coupling between the forward and backward modes of an adjacent *active* waveguide as schematically captured in Fig. 1.1(a) [4]. The active waveguide provides for optical gain while the coupled diffraction grating produces the required optical feedback. CMEs were used to characterize the structure and ultimately predict lasing behaviors on either side of a photonic bandgap (PBG).

The quantity of gain margin at threshold is proportional to the difference between the gain values of the two lowest-order lasing modes. Gain margin is used as a predictor of side-mode suppression ratio (SMSR) [35]. As the uniform-grating DFB lasing structure has two symmetric lasing modes for one value of threshold gain, as seen in Fig. 1.1(b) for various values of normalized direct-Bragg coupling coefficient $\kappa_a L$, the gain margin is zero.

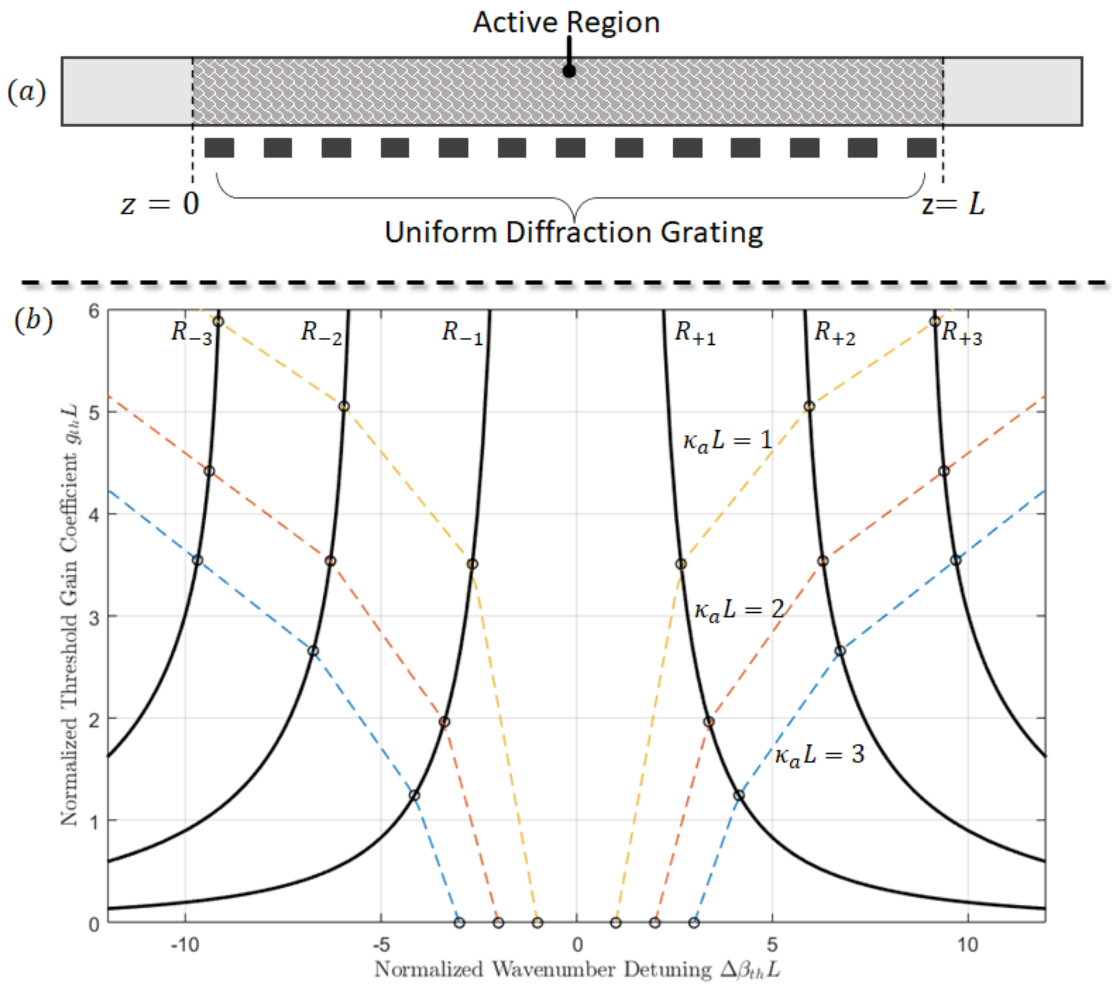

Figure 1.1 The uniform-grating distributed feedback (DFB) laser structure and mode spectrum demonstrating the mode degeneracy. (a) Adding an active region to the grating reflector provides for optical gain and, with the feedback provided by the diffraction grating, forms a DFB laser. (b) The mode spectrum of a uniform-grating DFB laser demonstrating degeneracy due to the symmetric pairs of modes on either side of the photonic bandgap. For a given normalized coupling $\kappa_a L$, the structure will seek to lase at two points on either side of the photonic bandgap when operated at its gain threshold. The dashed lines indicate the constant-coupling curves connecting across multiple lasing modes.

1.1.4 Methods of Single-Mode DFB Lasing

As high gain margin is desired for stable single-mode performance [36], and the seminal work on semiconductor DFB lasers demonstrate lasing but result in degenerate lasing modes [4], a $\lambda/4$-phase shift was introduced into the center of the diffraction grating resulting in single-mode operation with moderately high gain margin, as shown in Fig. 1.2(a) [5]. The

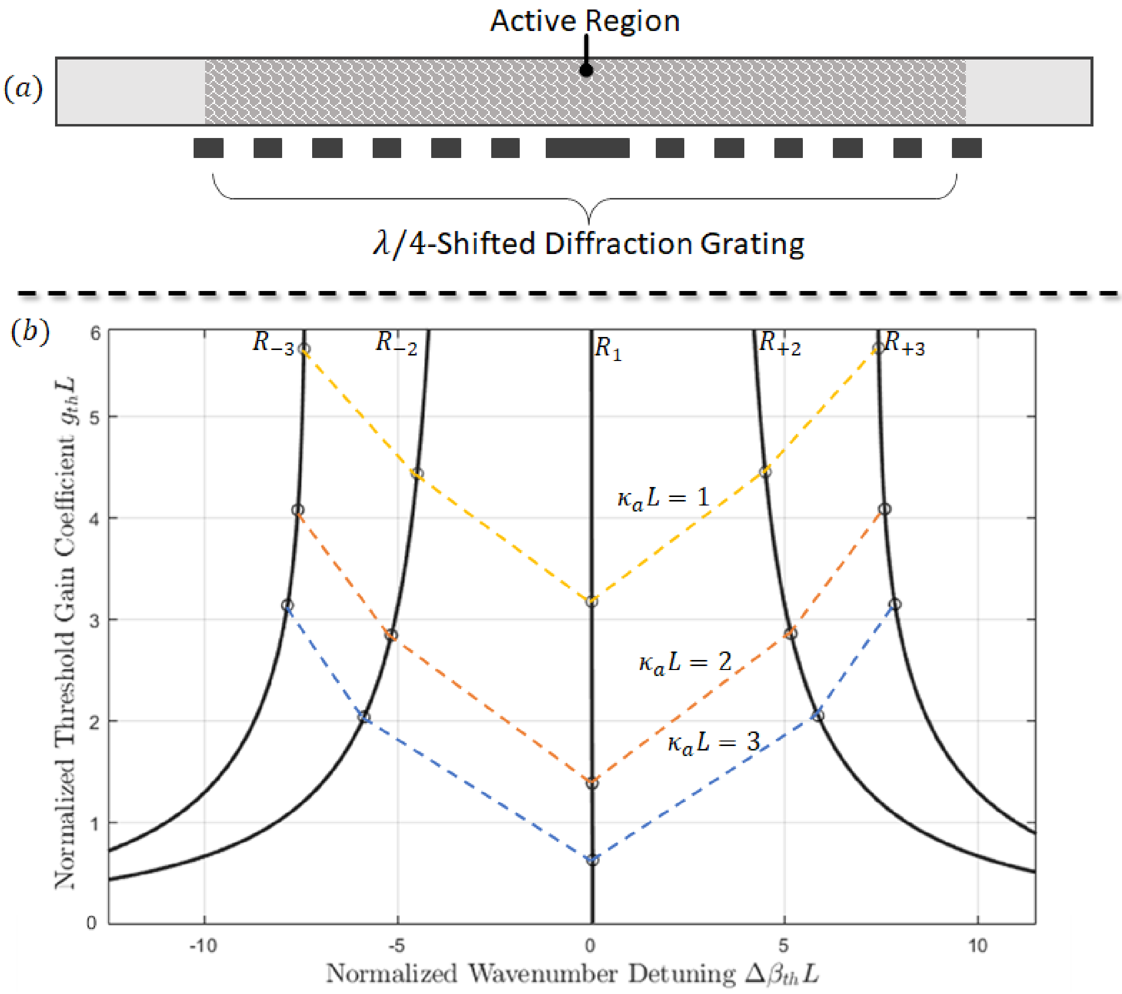

Figure 1.2 The $\lambda/4$-shifted grating distributed feedback (DFB) lasing structure and associated mode spectrum. (a) Including a $\lambda/4$-shift in the center of the diffraction grating breaks the mode degeneracy resulting in single-mode lasing. (b) Unlike the uniform diffraction grating, the $\lambda/4$-shifted DFB laser has a single mode centered at the normalized waveguide detuning $\Delta\beta_a L = 0$.

associated mode spectrum reveals a single mode at the center of the waveguide detuning $\Delta\beta_a L = 0$, as seen in Fig. 1.2(b). Unlike the uniform-grating DFB laser, this structure demonstrates gain margin between its fundamental mode and the first degenerate mode.

Gain margin changes as $\kappa_a L$ increases and depends upon the relationship between the fundamental lasing mode and the next closest lasing mode for a given $\kappa_a L$ value. The gain margin for the $\lambda/4$-shifted DFB laser is shown in Fig. 1.3 and demonstrates a peak gain margin of $\Delta\alpha L = 0.735$ at a normalized direct-Bragg coupling of $\kappa_a L = 2.2$.

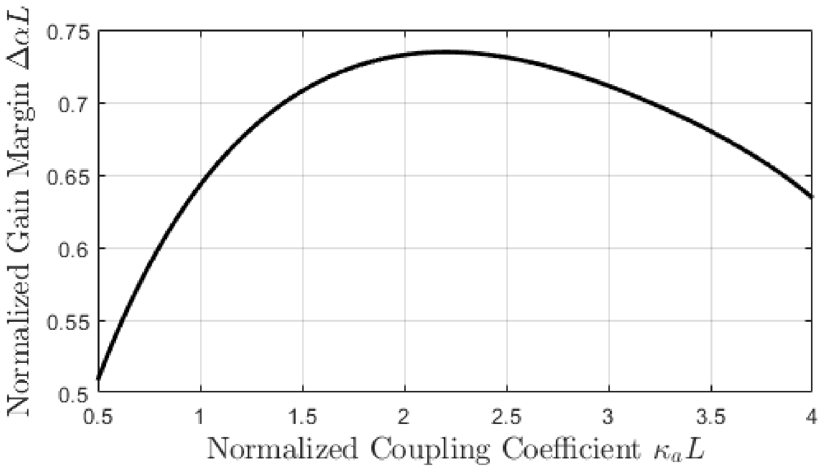

Figure 1.3 The gain margin $\Delta\alpha L$ for the $\lambda/4$-shifted DFB laser as a function of the normalized direct-Bragg coupling coefficient $\kappa_a L$. A peak gain margin of $\Delta\alpha L = 0.735$ occurs a $\kappa_a L = 2.2$.

The nonmonotonic nature of gain margin can be seen by tracing the mode-spectrum plot across various values of $\kappa_a L$. As the direct-Bragg coupling increases from smaller values up to the value of $\kappa_a L = 2.2$, the separation from the fundamental mode to the first degenerate mode increases as seen by the yellow and orange dotted lines of Fig. 1.2(b). As coupling continues to increase, the degenerate modes enter compression, as seen by the blue dotted line, causing gain margin to decline.

1.1.5 Issues with λ/4-Shifted DFB Lasing

Though single-mode lasing was achieved, industry-standard lasing devices based on a $\lambda/4$-shift exhibit power peaks in the active region of the waveguide centered at the diffraction grating phase-shift [34]. These peaky-power profiles, as shown by the blue curve in Fig. 1.4(a) for the $\lambda/4$-shifted DFB lasing structure, result in spatial-hole burning of gain along the length of the laser cavity.

The Henry's α_H nonlinearity, also known as the linewidth enhancement factor, quantifies a gain-dependent phase shift due to carrier injection in the active waveguide region due to a change in refractive index [37]. Peaky power within the active region, and its associated spatial-hole burning effect, results in a localized change in refractive index [35]. This localized change alters the $\lambda/4$-phase shift, thereby worsening gain margin.

A single value to represent the longitudinal power flatness F, when paired with gain margin $\Delta\alpha L$, provides for a set of metrics to predict and optimize for expected above-threshold lasing stability and performance. Laser cavity designs seek to minimize on flatness while maximizing on gain margin. For the traditional $\lambda/4$-shifted DFB laser, flatness is typically specified to be less than $F = 0.05$ to maintain good single-mode performance above gain threshold [38], [39]. The minimum flatness of the $\lambda/4$-shifted laser is $F = 0.012$ but does not correspond to the peak gain margin and instead has a lower $\Delta\alpha L = 0.68$.

The importance of gain margin as a predictor of above-threshold performance is well documented in the literature [36]; maximizing gain margin at threshold provides for a buffer of single-mode operation as laser power output increases. Nonlinear effects in the active region due to spatial-hole burning impact laser stability and the side-mode suppression ratio (SMSR) as long as Henry's alpha α_H remains non-zero. Active regions have non-zero values of Henry's alpha $\alpha_H \sim 1.5$ for quantum well based regions, though highly dependent on wavelength and well width [40], [41], and on the order of $\alpha_H \sim 5$ for bulk III-V materials [42]. Though recent work in quantum dots has predicted a near-zero-valued α_H, such materials continue to be relegated to academic research and appear to be several years away from commercial foundry integration.

Areas of high power can cause catastrophic laser failure if longitudinal power peaks coincide with dislocations or defects within the active region resulting in localized heating and, in worst case, cavity burnout [43]. Though mitigated though mature material processing in monolithic standalone devices, heterogeneous silicon-photonic lasers integration based on epitaxial growth or molecular bonding can result in threading dislocations which propagate through the active region due to a lattice mismatch between the silicon and III-V material boundaries [44]. Vertical and horizontal aspect ratio trapping (ART) and nano-ridge engineering seek to minimize on these defects but continue to remain an active and nascent area

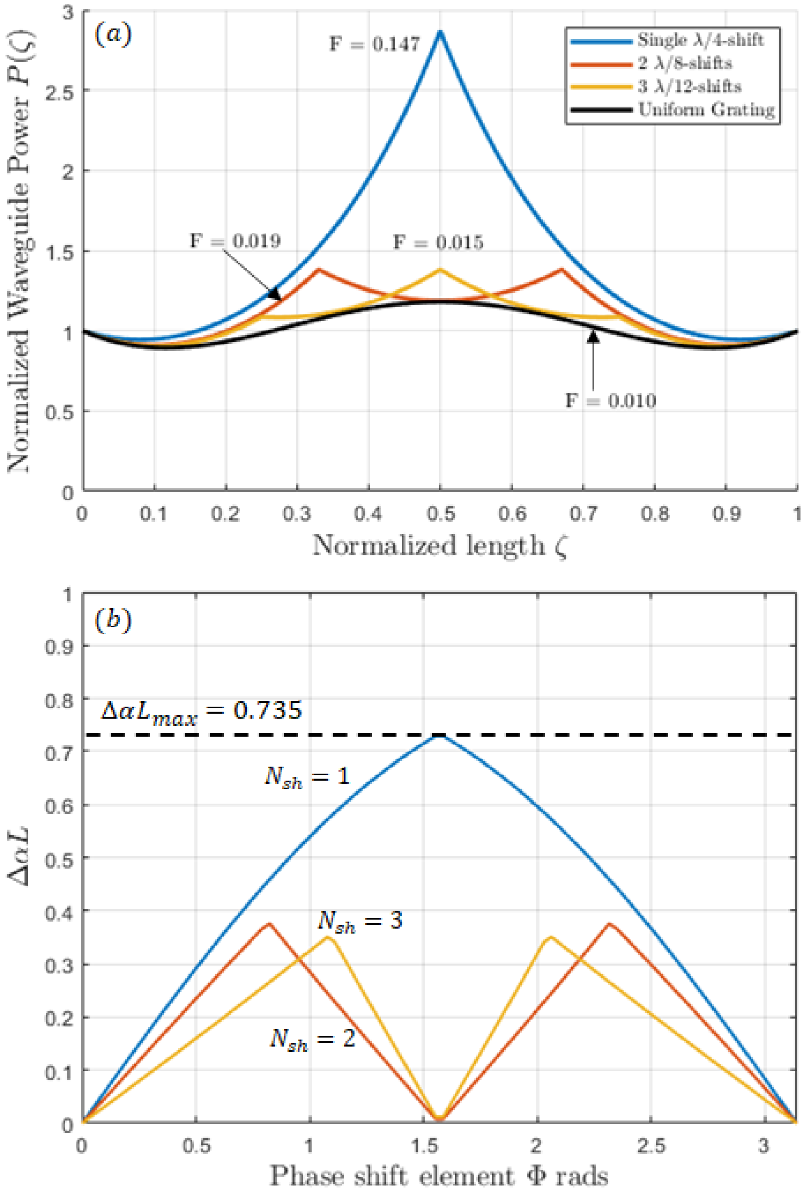

Figure 1.4 Longitudinal power profiles and gain margin for three DFB lasers with different phase-shift elements. (a) The longitudinal power profile of the $\lambda/4$-shifted DFB laser has a peaky power profile centered on the phase-shift region. Including additional phase-shift elements reduces the peaky profile. (b) The gain margin for the $\lambda/4$-shifted DFB peaks at $\Delta\alpha L = 0.735$ for a single $\pi/2$ element and declines dramatically as additional elements are included. The normalized direct-Bragg coupling is $\kappa_a L = 2.2$ for all cases shown.

of research [45], [46]. Minimizing on flatness within the laser cavity reduces the peak power and lowers the likelihood of critical failure due to cavity burnout.

1.1.6 Attempted Fixes

Additional phase elements and other variations in diffraction-grating geometries were studied, intent on flattening the power profile and, thereby, maintaining single-mode performance as gain increased above its threshold value. These structures improve on power flatness as shown by the red and yellow curves of Fig. 1.4(a) for the inclusion of two and three grating phase shifts respectively. The flatness values of each power profile for $\kappa_a L = 2.2$ are included in Fig. 1.4(a) and the degenerate uniform-grating DFB laser power profile is shown in black for reference.

An unfortunate trade of adding the additional phase-shift elements is a reduction in peak gain margin and an increase in diffraction-grating complexity [34]. The maximum gain margin occurs for a single phase shift in the diffraction grating. As additional elements are included gain margin dramatically drops as seen in Fig. 1.4(b). The blue and yellow curves with $N_{sh} = 1$ and $N_{sh} = 3$ are the gain margins across element phase shift value for a DFB laser with $\kappa_a L = 2.2$.

Additional grating phase shifts [36], [38], longitudinal variation in coupling strength [47], [48], spreading of the required phase shift through corrugation pitch modulation (CPM) [34], [49], and longitudinal variations in wavenumber detuning using traditional or machine-learning based methods to generate optimal complex grating structures [36], [39], were all considered to improve on the power flatness. Though each proposed solution improved upon flatness, they all did so at the expense of a reduction in gain margin and an increase in diffraction-grating complexity. The $\lambda/4$-phase shifted DFB lasers form the bulk of commercially available semiconductor-based solutions whether for stand-alone devices or those embedded in integrated- or silicon-photonic circuit offerings and, as such, all suffer from these limitations.

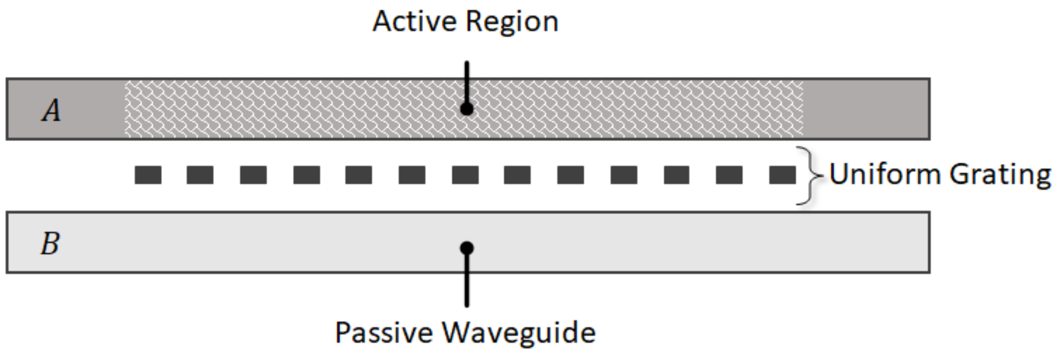

Figure 1.5 The first novel single-mode lasing structure. A uniform diffraction grating is sandwiched between a waveguide A having an active region and a passive waveguide B. Single-mode behavior is derived from direct-Bragg coupling providing the optical feedback and exchange-Bragg coupling working to suppress the degenerate mode.

1.2 Overview of Dissertation

1.2.1 Single-Mode DFB Lasing using Photonic-Bandgap Alignment

This dissertation models and explores two novel single-mode lasing structures using coupled dissimilar waveguides. The first structure is comprised of an active waveguide coupled to a uniform diffraction grating coupled to a passive waveguide as shown in Fig. 1.5. In this structure, direct-Bragg coupling provides for optical feedback while exchange-Bragg coupling provides for degenerate mode suppression presenting an entirely new method for achieving single-mode distributed-feedback lasing using photonic bandgaps (PBGs). This structure eliminates the $\lambda/4$-phase shift introduced into the diffraction grating of legacy DFB lasers and, therefore, avoids the associated peaky power profile and its nonlinear effects.

Waveguide A contains the active region for lasing, and therefore direct-Bragg coupling within A is expected to exhibit strong, degenerate resonances on either side of its PBG. Through the proper selection of waveguide wavenumber detuning, these degenerate modes are suppressed by aligning the exchange-Bragg PBG_χ and the passive waveguide B direct-

Bragg PBG$_b$ on top of the undesired resonance, resulting in single-mode lasing. By using a uniform grating, the $\lambda/4$-phase shift, spatial chirp, and other non-uniformities, as well as the exacerbated nonlinear spatial-hole burning problem are each avoided.

Coupled-mode equations (CMEs) are introduced that include gain and the associated nonlinearity of the active region to solve for the key lasing characteristics of gain threshold, gain margin, and longitudinal power flatness [50]. Furthermore, the impact of exchange-Bragg-coupling strength as well as evanescent-coupling strength is considered in the lasing model. Using an at-threshold analysis, closed-form analytic solutions are formed at lasing threshold for this dual-waveguide, four-port structure revealing a high normalized gain margin accompanied by a low power flatness along the active region, outperforming the $\lambda/4$-shifted DFB laser structure.

The closed-form mathematical models for the new single-mode lasing structure are developed, behaviors presented, and performance optimized. The developed model is used to characterize and predict lasing behaviors using quantities such as waveguide detuning, coupling strength, gain, loss, and the Henry's α_H nonlinearity. Optimizing desired behaviors, such as gain margin and longitudinal power flatness, is accomplished using minimization techniques across the model quantities. A physical understanding of why specific quantities results in optimal behaviors becomes apparent when the mathematical model for the structure is dissected.

This single-mode lasing mechanism is compelling for both standalone III/V and heterogeneous III/V-on-silicon platforms.

1.2.2 Single-Mode DFB Lasing using a Coupled NIM Waveguide

The second of the two novel structures presented in this dissertation models an active waveguide coupled to a negative-index material (NIM) waveguide to provide optical feedback without using a diffraction grating. Here, single-mode behavior is predicted through intentional design of waveguide wavenumber detuning between the active positive-index material

(PIM) waveguide and the NIM waveguides. Unlike Bragg based DFB lasers, where the waveguide wavenumber detuning is relative to a fixed Bragg wavelength, detuning for the PIM-NIM lasing structure is based on the difference between each waveguides dispersion characteristics. By ensuring detuning is always positive or always negative one of the degenerate modes can be avoided resulting in single-mode lasing behavior.

A new method for achieving DFB has been recently proposed and modeled based on the evanescent coupling of PIM waveguide to a NIM waveguide [51]–[53]. Metamaterials offer remarkable electrodynamic behavior stemming from a *negative* refractive index [54]; despite having a negative refractive index, a NIM sandwiched between PIM has been predicted to support the propagation of a transverse optical mode [55]–[57]. Notably, the Poynting vector of an optical field traveling through a NIM waveguide can have the *opposite* direction as the associated wave vector [53], [55]. Such a NIM waveguide, when evanescently coupled to PIM waveguide, creates a distributed coupling region where power flows in either longitudinal direction [51].

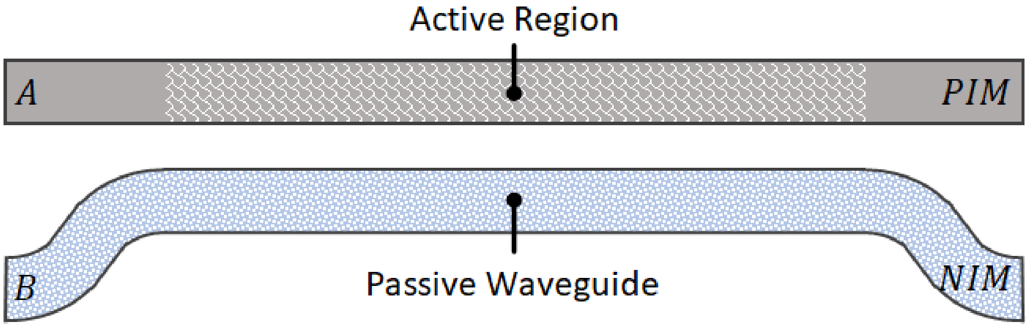

Figure 1.6 The second novel lasing structure. A schematic of the PIM-NIM DFB laser, where the active region of a PIM waveguide A is evanescently coupled to a lossy NIM waveguide B over length L. The (white) cladding regions surrounding the waveguides are PIM. The counter-directional nature of the Poynting vectors in either waveguide results in distributed feedback, resonant optical gain, and, ultimately, lasing.

The inclusion of optical gain to PIM waveguide over the length of the coupling region L generates the proposed *active* PIM-NIM lasing structure shown in Fig. 1.6. To study this active structure, the PIM-NIM coupled-mode equations are expanded to include gain for the PIM waveguide and loss for the NIM waveguide. This model predicts the occurrence of lasing with unique dependencies on waveguide parameters not found in traditional active DFB structures.

Closed-form mathematical models for the new single-mode PIM-NIM lasing structure are developed and behaviors presented. The developed model is used to characterize and predict lasing behaviors using quantities such as waveguide detuning, coupling strength, gain, and loss. A transcendental lasing condition is derived which supports the prediction of the lasing structures threshold gain and its at-threshold mode spectrum.

1.2.3 Methodologies: Research Design & Strategy of Inquiry

This dissertation focuses on coupled-mode theory to derive the physical relationships between the modes of the novel lasing structures. Presented mathematical solutions provide closed-form expressions for electric-fields, longitudinal power profiles, transmittivity, lasing thresholds, gain-margin, and power flatness for at-threshold analysis. An entirely new solution method is developed and presented which solves for the fourth-order CMEs of the active-passive uniform grating coupled structure. Each solution exposes new lasing behaviors for both structures and provides design requirements for future work.

1.2.4 Outline

This dissertation dedicates Chapter 2 to fundamental mathematics of coupled-mode theory. Coupled-mode theory is presented and each constituent quantity of the general formulation is discussed. The theory is used to develop models for the well-understood directional coupler, grating reflector, and DFB laser. Two independent coupled-mode equation solution processes are showcased in the development of the electric-field expressions for the directional coupler and the grating reflector; both processes are used in the later chapters of this work. The concepts for complex detuning, mode spectrum, gain-margin, and power flatness are introduced using the DFB laser.

Chapter 3 presents the first novel lasing structure based on an active waveguide coupled to a uniform diffraction grating coupled to a passive waveguide. Coupled-mode equations and coupling coefficients are defined and the electric-field, longitudinal power, and transmittivity expressions are derived. The new solution process developed explicitly to solve these fourth-order coupled differential equations is first executed for the three-coupling case, where evanescent coupling is neglected, and then executed for the more complicated and inclusive four-coupling case which includes all Bragg-based coupling as well as evanescent coupling.

Chapter 4 uses the expressions developed in Chapter 3 to understand and optimize on lasing behavior for the structure while accounting for the semiconductor non-linearity in the lasing model. The exchange-Bragg photonic bandgap is aligned and shown to suppress the degenerate mode resulting in single-mode lasing behavior. It is a primary objective for the presented lasing structures to maintain a highly flat longitudinal power profile and, thereby, minimizing the spatial-hole burning nonlinear impacts. The presented mathematical models predict and optimize the structure quantities of gain margin and longitudinal power flatness. The lasing-mode spectrum is presented and gain margin is then demonstrated which exceeds that of the industry standard $\lambda/4$-shifted DFB laser. Furthermore, the parameterized model demonstrates extremely low longitudinal power flatness again outperforming the $\lambda/4$-shifted DFB laser. Further characterization of lasing behaviors is provided over changes exchange-Bragg coupling strength κ_χ and evanescent coupling strength κ_e. This lasing structure demonstrates highly compelling at-threshold results and is applicable for silicon-photonic or integrated-photonic platforms and integration.

Chapter 5 presents CMEs and solutions for the second novel lasing structure, one based on the evanescent coupling between an active positive-index material (PIM) waveguide and a passive negative index material (NIM) waveguide. Solutions presented are shown to be remarkably similar to the traditional uniform-grating DFB laser, however, achieve feedback without the use of a diffraction grating. Eigenvalues and the associated photonic bandgap expression introduce a round-trip gain and a disparity from transparency not seen in grating-based DFB lasers.

Chapter 6 examines the behaviors of the PIM-NIM lasing structure and provides motivation for single-mode operation. It is shown that through the insightful design of the PIM-NIM's dispersion relationship over the gain bandwidth of the PIM's active region, the detuning between the waveguides can be made always positive or always negative, resulting in single-mode operation.

Chapter 7 concludes the dissertation, presenting potential future work and summarizing the main contributions of the research.

2. Basic Theory

2.1 Introduction

Coupled-mode theory and the associated differential coupled-mode equations (CMEs) are well established in the photonics and laser research communities. They have been employed in various passive structures such as directional couplers [58]–[60], narrow-band reflectors [61], [62], filters [63], [64], and add-drop multiplexers [65]. CMEs have been used to develop the mathematical models and predict the associated behaviors of active devices including distributed feedback (DFB) lasers [4], [5], [35], [66], [67]. These works demonstrate that CMEs provide for relevant and appropriate models to understand photonic structures and, in particular, lasing behaviors.

Unlike finite-difference time-domain methods (FDTD) and finite-element methods (FEM), which approximate behaviors by breaking a structure into many small parts and solving numerically for localized electric-fields or other quantities, CMEs seek to derive parameterized solutions of a structure in a more global fashion. Though the closed-form parameterized solutions typically limit CMEs to fundamental devices of one to several perturbations and modes, they provided for unparalleled physical insight into structure behavior. Devices such as differential couplers or traditional distributed feedback lasers are modeled with two coupled modes and result in a second-order differential equation which can be solved in closed-form using quadratic methods [4], [5], [62], [68].

In this chapter, the mathematical foundation for coupled-mode theory, coupled-mode

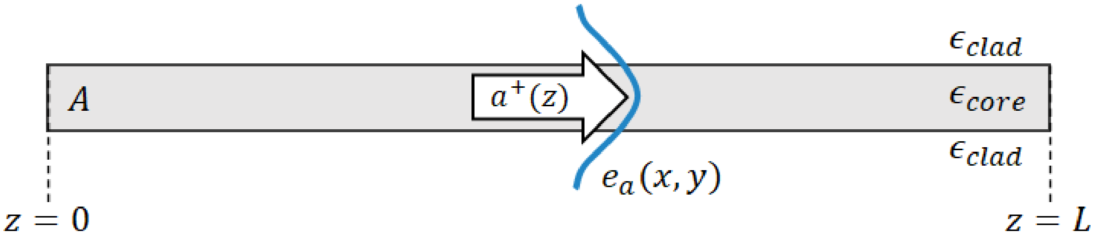

Figure 2.1 The unperturbed waveguide A and its associated modes form the well-understood baseline for perturbation theory. The waveguide has a permittivity of ε_{core} and is surrounded by cladding material of permittivity ε_{clad}. The forward-traveling longitudinal mode $a^+(z)$, shown as the arrow, has a transverse mode profile $\mathbf{e}_a^+(x,y)$, shown symbolically with the blue curve. The structure is of length L.

equations, coupling coefficients, and wavenumber detuning will be introduced. The grating coupler, the distributed feedback laser, the contra-directional coupler, and the directional coupler will each be developed and examined using coupled-mode theory. For the grating coupler, electric-field solutions are found using an ansatz-based approach, while for the directional coupler, an eigenvalue-based approach is taken to isolate electric-field solutions. These two mathematical methods are presented deliberately so as to showcase both the underlying coupled-mode theory as well as the basics of the solutions processes which will be used in this work.

As a matter of notation, vectors and vector fields are presented in bold font though out this work. The longitudinal direction of propagation will be $\hat{\mathbf{z}}$ and the transverse directions will be $\hat{\mathbf{x}}$ and $\hat{\mathbf{y}}$. All quantities which are marked with a $\tilde{}$ are assumed to be complex valued.

2.2 Coupled-Mode Theory

2.2.1 Geometry

Coupled-mode theory presents a mathematical model describing the change in a guided mode's electromagnetic-field envelope when subject to a perturbation in the local refractive index [68]. The guided mode is typically given as an optical mode longitudinally propagating along a section of waveguide with the longitudinal direction of propagation given by z. The forward-propagating unperturbed mode $a^{+}(z)$ has a transverse electric-field profile $\mathbf{e}_a^{+}(x,y)$ which is a function of the core permittivity, cladding permittivity, and the physical waveguide geometry as shown in Fig. 2.1. This structure and its associated mode provide a reference by which more complicated structures are modeled.

Coupled-mode theory seeks to mathematically model the modes of a new perturbed structure as created through the introduction of permittivity changes and new guided modes to the original well-understood unperturbed geometry. Two examples of such perturbations are shown in Fig. 2.2. The first example couples a uniform diffraction grating, built on a material with permittivity ε_3, to the original waveguide. The second example introduces an adjacent waveguide B made of a permittivity ε_{core_2} which has its own guided mode $b^{+}(z)$. In both cases, coupled-mode theory seeks to model and understand the modal power transfer which occurs along the length of the perturbed structure. A detailed mathematical formulation of each of these two structures will be presented in the sections below.

2.2.2 Lorentz Reciprocity Theorem

This dissertation uses the sign convention of $e^{-i\omega t}$, such that the electric and magnetic fields are given by $\mathbf{E}(x,y,z,t) = \mathbf{e}(x,y)e^{-i\omega t+i\beta z}$ and $\mathbf{H}(x,y,z,t) = \mathbf{h}(x,y)e^{-i\omega t+i\beta z}$. Note that the only z dependence of $\mathbf{E}$ and $\mathbf{H}$ is in the phase term and not in the amplitude term. In this sense, the expressions represent the eigenmodes of the unperturbed waveguides. Ignoring the time component and focusing on the longitudinal direction of propagation z, the basic field expressions become:

$$\mathbf{E}_p(x,y,z) = \mathbf{e}_p(x,y)e^{i\beta_p z} \tag{2.1a}$$

$$\mathbf{H}_p(x,y,z) = \mathbf{h}_p(x,y)e^{i\beta_p z}, \tag{2.1b}$$

where p is the propagation mode index and $\beta_p = \text{sgn}(p)\ 2\pi n/\lambda_0$ is the modal wavenumber, n is the modal refractive index of the waveguide, and λ_0 is the free-space wavelength.

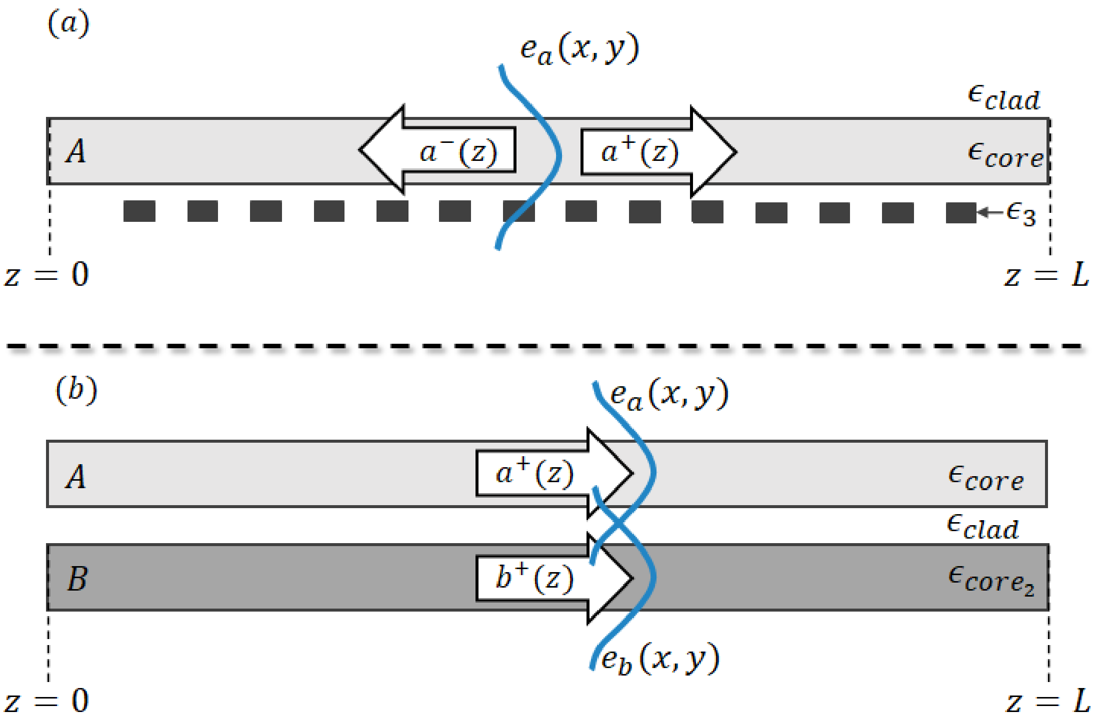

Figure 2.2 Two examples of perturbations introduced to the original unperturbed geometry. (a) A uniform diffraction grating with permittivity ε_3 working to couple power back into mode $a^-(z)$. (b) A second adjacent waveguide with permittivity ε_{core_2} and its associated mode $b^+(z)$. In both cases, the transverse mode profile associated with the unperturbed region overlaps with the second transverse mode in the region of perturbation. This modal overlap will define the coupling coefficient capturing the power transfer capability between the two modes.

The expression $\mathrm{sgn}(p) = +$ for $p > 0$, where $p \in \mathbb{Z}$, implying $\beta_p > 0$, corresponding to forward-propagating waves. Moreover, $\mathrm{sgn}(p) = -$ for $p < 0$, where $p \in \mathbb{Z}$, implying $\beta_p < 0$, corresponding to backward-propagating waves and, thus, $\beta_{-p} = -\beta_p$.

Coupled-mode equations represent the perturbed system as a linear combination of the unperturbed modes. It is assumed that the modes are and remain orthogonal when under the introduction of the perturbation. This assumption provides for a reasonable first-order approximation such that physical behaviors can be well understood even if the exact calculated values are only approximate. Fields of the unperturbed system will be noted as $\mathbf{E}$ and $\mathbf{H}$ and fields of the perturbed system are noted with an apostrophe as $\mathbf{E}'$ and $\mathbf{H}'$.

The Maxwell-Heaviside curl equations for the unperturbed system are written as

$$\nabla \times \mathbf{E} = -i\omega\mu\mathbf{H}, \tag{2.2a}$$

$$\nabla \times \mathbf{H} = i\omega\varepsilon\mathbf{E}, \tag{2.2b}$$

and for the perturbed system are written as

$$\nabla \times \mathbf{E}' = -i\omega\mu\mathbf{H}', \tag{2.3a}$$

$$\nabla \times \mathbf{H}' = i\omega\varepsilon'\mathbf{E}', \tag{2.3b}$$

where ε' is the permittivity of the introduced perturbation. The permeability is assumed to be that of free space $\mu(x,y,z) = \mu_0$ in both the unperturbed and perturbed spaces.

The dot product of the conjugate (*) of each unperturbed field and the opposite curl equation for the perturbed field in Eq. (2.3) provides:

$$\mathbf{E}^* \cdot (\nabla \times \mathbf{H}') = i\omega\varepsilon'\mathbf{E}^* \cdot \mathbf{E}', \tag{2.4a}$$

$$\mathbf{H}^* \cdot (\nabla \times \mathbf{E}') = -i\omega\mu\mathbf{H}^* \cdot \mathbf{H}'. \tag{2.4b}$$

Similarly, the dot product of each perturbed field can be taken with the conjugate of the opposite curl equation of the unperturbed field is Eq. (2.2) to arrive at:

$$\mathbf{E}' \cdot (\nabla \times \mathbf{H}^*) = i\omega\varepsilon'\mathbf{E}' \cdot \mathbf{E}^*, \tag{2.5a}$$

$$\mathbf{H}' \cdot (\nabla \times \mathbf{E}^*) = -i\omega\mu\mathbf{H}' \cdot \mathbf{H}^*. \tag{2.5b}$$

The equations above can be combined as (2.4a) − (2.4b) + (2.5a) − (2.5b) and, with the use of the vector calculus cross-product identity

$$\nabla \cdot (\mathbf{A} \times \mathbf{B}) = (\nabla \times \mathbf{A}) \cdot \mathbf{B} - (\nabla \times \mathbf{B}) \cdot \mathbf{A}, \tag{2.6}$$

and some simplification, produces the expression

$$\nabla \cdot \left(\mathbf{E}^* \times \mathbf{H}' + \mathbf{E}' \times \mathbf{H}^*\right) = -i\omega(\varepsilon' - \varepsilon)E^* \cdot E'. \tag{2.7}$$

The volume integral of the above expression along the unperturbed waveguide after application of Gauss's law and further manipulation, ultimately generates the relationship

$$\iint_\Xi \frac{\partial}{\partial z}\left(\mathbf{E}_t^* \times \mathbf{H}_t' + \mathbf{E}_t' \times \mathbf{H}_t^*\right) \cdot \hat{\mathbf{z}}\, d\Xi = -i\omega \iint_\Xi \left(\varepsilon' - \varepsilon\right) \mathbf{E}' \cdot \mathbf{E}^*\, d\Xi. \tag{2.8}$$

where $\mathbf{E}_t$ and $\mathbf{H}_t$ are the transverse field components of the electric and magnetic fields respectively and Ξ is the surface surrounding the volume of integration. The variable $\varepsilon'(x,y,z)$ represents the permittivity of the perturbation and can be arbitrarily complicated. The field components in the $\hat{\mathbf{x}}$ and $\hat{\mathbf{y}}$ directions do not contribute to the integral expression as they are evanescent and become zero valued infinitely far away from the waveguide. As the vector cross product produces a resultant vector which is orthogonal to the constituent input vectors, only the transverse mode components $\mathbf{E}_t$, $\mathbf{H}_t$, $\mathbf{E}_t^*$ and $\mathbf{H}_t^*$ contribute to the surface integral along the $\hat{\mathbf{z}}$ direction of Eq. (2.8). This expression is known as the Lorentz reciprocity theorem and provide the foundation from which the coupled-mode equations, used throughout this document, are based.

2.2.3 Mode Kernels

By examining the condition where both the perturbed and unperturbed geometries are identical, that is $\varepsilon'(x,y,z) = \varepsilon$, the Lorentz reciprocity theorem can be reduced to:

$$\iint_\Xi \frac{\partial}{\partial z}\left(\mathbf{E}_t^* \times \mathbf{H}_t' + \mathbf{E}_t' \times \mathbf{H}_t^*\right) \cdot \hat{\mathbf{z}} d\Xi = 0. \tag{2.9}$$

Substituting back in the expressions for both the electric and magnetic field of the unperturbed modes indexed by r, and the perturbed modes indexed by s, as shown in Eq. (2.1), and reducing results in two expressions; one for forward-traveling modes ($s > 0$):

$$(\beta_r - \beta_s) \iint_{\Xi} (\mathbf{E}_{rt}^* \times \mathbf{H}_{st} + \mathbf{E}_{st} \times \mathbf{H}_{rt}^*) \cdot \hat{\mathbf{z}} \, d\Xi = 0, \tag{2.10}$$

and one for reverse-traveling modes ($s < 0$):

$$(\beta_r + \beta_s) \iint_{\Xi} (-\mathbf{E}_{rt}^* \times \mathbf{H}_{st} + \mathbf{E}_{st} \times \mathbf{H}_{rt}^*) \cdot \hat{\mathbf{z}} \, d\Xi = 0, \tag{2.11}$$

where $\mathbf{E}_t$ and $\mathbf{H}_t$ represent any viable transverse mode-profile pair indexed by either r or s.

The above expressions are valid under two conditions. The first condition occurs where $r \neq s$ and $\beta_r \neq \beta_s$; the integral itself must then resolve to zero. The sum of the forward and reverse-traveling wave equations under this condition becomes:

$$\iint_{\Xi} (\mathbf{E}_{st} \times \mathbf{H}_{rt}^*) \cdot \hat{\mathbf{z}} \, d\Xi = 0. \tag{2.12}$$

The second condition occurs when either $r = s$ or $r = -s$ and the integral can be non-zero as $\beta_r = \beta_{\pm s} = \pm\beta_s$. The expression in the integral for both forward and reverse traveling waves under this condition reduces to the Poynting vector $\mathbb{S}$ and denotes the optical modes power P. The $\mathrm{sgn}(\mathbb{S})$ is present to ensure that the power is a positive result as the Poynting vector $\mathbb{S}$ will result in a negative value for backwards-traveling power. The expression of Eq. (2.12) then becomes

$$\Re \left[\iint_{\Xi} (\mathbf{E}_{rt} \times \mathbf{H}_{rt}^*) \cdot \hat{\mathbf{z}} \, d\Xi \right] = 2P \, \mathrm{sgn}(\mathbb{S}), \tag{2.13}$$

where $\Re$ denotes the real portion of the result. From this expression, any mode r is orthogonal to any other mode s when $r \neq s$ and, only when $r = s$, is power produced.

The transverse modes are each normalized by $\sqrt{2P}$ yielding

$$\mathbf{e}_{rt} = \frac{\mathbf{E}_{rt}}{\sqrt{2P}}, \tag{2.14a}$$

$$\mathbf{h}_{rt} = \frac{\mathbf{H}_{rt}}{\sqrt{2P}}, \tag{2.14b}$$

such that,

$$\Re\left[\iint_{\Xi} (\mathbf{e}_{rt} \times \mathbf{h}_{rt}^{*}) \cdot \hat{\mathbf{z}}\, d\Xi\right] = \operatorname{sgn}(\mathbb{S}), \tag{2.15}$$

where $\mathbf{e}_{rt}$ and $\mathbf{h}_{rt}$ are the normalized transverse electric- and magnetic-field components of the r^{th} modes. This is the necessary and sufficient condition to form a basis set spanning the signal space defined by the unperturbed mode fields. Each supported normalized mode can be considered as a mode-kernel function to form solutions for a perturbed system under the approximation that an introduced perturbation does not alter the original unperturbed mode.

2.2.4 Coupled-Mode Equations

For each mode indexed by r, a complex function $a_r(z)$ is found which adjusts both the power and phase of perturbed mode along the longitudinal position z:

$$\left.\begin{matrix} \mathbf{E}'(x,y,z) \\ \\ \mathbf{H}'(x,y,z) \end{matrix}\right\} = \sum_r a_r(z) \left\{\begin{matrix} \mathbf{e}_r(x,y) \\ \\ \mathbf{h}_r(x,y) \end{matrix}\right\} e^{i\beta_r z}. \tag{2.16}$$

Taking advantage of the orthogonality relationship and returning to the Lorentz reciprocity theorem in Eq. (2.8) under the condition where now $\varepsilon'(x,y,z)$ represents the perturbed system, it can be found that the modal field envelopes are described by the family of coupled-mode differential equations:

$$\frac{da_r(z)}{dz} = i\operatorname{sgn}(\mathbb{S}) \sum_s a_s(z) e^{-i2\Delta\beta_{rs}z} \kappa_{sr}, \tag{2.17}$$

where $\Delta\beta_{rs} = (\beta_r - \beta_s)/2$, sgn($\mathbb{S}$) is the sign of the receive mode power flow as shown in Eq. (2.15), and κ_{sr}, defined further in the section below, are the coupling coefficients between sending and receiving modes.

The detuning parameter $\Delta\beta_{rs}$ captures the difference between wavenumbers of the "receive" mode r to the wavenumber of the "send" mode s. When solved, each value of $a_r(z)$ will express the slow-moving envelope for the r^{th} mode in the perturbed system [68] as

$$\mathbf{E}'_r(z) = a_r(z)e^{i\Delta\beta_{rs}z}\,\mathbf{e}_r(x,y)e^{i\bar{\beta}z}, \tag{2.18a}$$

$$\mathbf{H}'_r(z) = a_r(z)e^{i\Delta\beta_{rs}z}\,\mathbf{h}_r(x,y)e^{i\bar{\beta}z}, \tag{2.18b}$$

where $\bar{\beta} = (\beta_r + \beta_s)/2$.

Summing across all modes r provides for the composite electromagnetic field of the perturbed structure as:

$$\left.\begin{matrix}\mathbf{E}'(x,y,z)\\ \\ \mathbf{H}'(x,y,z)\end{matrix}\right\} = \sum_r \left\{\begin{matrix}\mathbf{E}'_r(x,y)\\ \\ \mathbf{H}'_r(x,y)\end{matrix}\right\} = \sum_r a_r(z)e^{i\Delta\beta_{rs}z} \left\{\begin{matrix}\mathbf{e}_r(x,y)\\ \\ \mathbf{h}_r(x,y)\end{matrix}\right\} e^{i\bar{\beta}z}. \tag{2.19}$$

The slow moving envelope expression on the right-hand side is in a rotated frame and can be captured by defining the quantity

$$\hat{a}(z) = a(z)e^{i\Delta\beta_{rs}z}. \tag{2.20}$$

Using this rotated-frame form leads to linear variants of the coupled-mode equations in Eq. (2.16), as will be seen in later sections.

2.3 Coupling Coefficients

Each coupling coefficient κ_{sr} is defined by a transverse-mode-overlap integral of a normalized power-sending mode profile $\mathbf{e}_s(x,y)$ and a normalized power-receiving mode profile

$\mathbf{e}_r(x,y)$, as [68]

$$\kappa_{sr} = \frac{\omega\varepsilon_0}{2} \int\limits_{-\infty}^{\infty} \int\limits_{-\infty}^{\infty} \Delta\bar{\varepsilon}(x,y)\mathbf{e}_s(x,y) \cdot \mathbf{e}_r^*(x,y)\; dy\; dx, \tag{2.21}$$

where $\mathbf{e}_s(x,y)$ and $\mathbf{e}_r(x,y)$ are the normalized transverse electric-field components of the sending and receiving modes with scalar amplitudes of $e_s(x,y)$ and $e_r(x,y)$ respectively, $\Delta\bar{\varepsilon}(x,y) = \bar{\varepsilon}'(x,y) - \bar{\varepsilon}(x,y)$ is change in relative permittivity of the perturbation region relative to the unperturbed region, $\bar{\varepsilon}' = \varepsilon'/\varepsilon_0$ is the relative permittivity of the perturbed region, $\bar{\varepsilon} = \varepsilon/\varepsilon_0$ is the relative permittivity of the unperturbed region, ε_0 is the permittivity of free-space, ω the angular frequency, and * denotes the complex conjugate. If the transverse modes $e_s(x,y)$ and $e_r(x,y)$ occupy the same waveguide and experience the same perturbations then their mode profiles are the same whether traveling in the $+$ or $-\ z$ direction.

Coupling coefficients capture the field coupling between a sending and receiving mode and may be estimated using Eq. (2.21). Though the definitions of coupling coefficients are provided, all coupling values are treated phenomenologically throughout this dissertation and their mode-overlap integrals are not explicitly calculated. Presented coupling-coefficient values are considered as design requirements for future experimental or fabrication efforts. Furthermore, the approximation is made that the unperturbed modes match the actual mode profiles and are orthogonal. These approximations have allowed for insightful modeling of passive and active structures having evanescent, direct-Bragg, and exchange-Bragg coupling [4], [5], [35], [58]–[66].

2.4 Wavenumbers & Detunings

The wavenumber, given as β_p in Eq. (2.1), is associated with either a receiving or sending mode in the coupled-mode equations and is denoted as

$$\beta_{(r,s)} = \text{sgn}(\mathbb{S}_r, \mathbb{S}_s)\, \frac{2\pi n}{\lambda_0}, \tag{2.22}$$

where r or s indicates a receiving or sending mode, n is the effective refractive index of the waveguide associated with the mode, and λ_0 is the free-space wavelength.

The coupled-mode equations in Eq. (2.17) contain a real-valued wavenumber detuning in the exponent defined as

$$\Delta\beta_{rs} = (\beta_r - \beta_s)/2. \tag{2.23}$$

Loss in a waveguide is accounted for by introducing an imaginary component to the wavenumber as

$$\tilde{\beta}_{(r,s)} = \beta_{(r,s)} + i\alpha/2, \tag{2.24}$$

where α is the power loss coefficient of the waveguide and $\tilde{}$ indicates a complex-valued wavenumber. Wavenumbers for active waveguides, that is waveguides with optical gain, can similarly be written as

$$\tilde{\beta}_{(r,s)} = \beta_{(r,s)} - ig/2, \tag{2.25}$$

where g is the power gain coefficient.

In semiconductor media, the increase in carrier density within the active region drives an increase in optical gain and an undesired decrease in the waveguides refractive index. The rate of change in refractive index as gain increases is accounted for in the complex wavenumber by including a constant gain multiplier $(1-\alpha_H)$ where α_H is Henry's alpha, also referred to as the linewidth enhancement factor [37]. A complex waveguide wavenumber which considers Henry's alpha is given by

$$\begin{aligned} \tilde{\beta}_{(r,s)} &= \beta_{(r,s)} - ig(1-i\alpha_H)/2, \qquad (2.26a) \\ &= \beta_{(r,s)} - g\alpha_H/2 - ig/2. \qquad (2.26b) \end{aligned}$$

When expanding out the gain phase relationships as above, the impact on detuning becomes apparent; as gain increases the injected carriers work to shift the waveguide wavenumber.

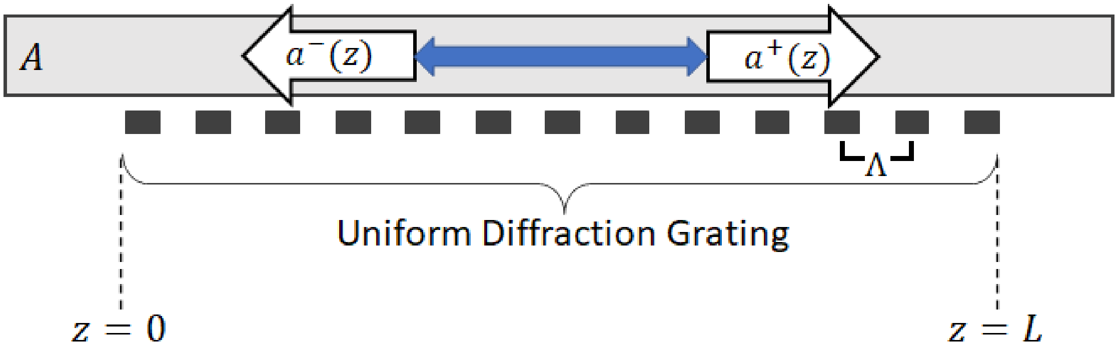

Figure 2.3 A grating reflector of length L demonstrating direct-Bragg coupling (symbolically represented by the blue arrow) between a forward-traveling mode a^+ in the A waveguide to a backward-traveling mode a^- also in the A waveguide.

2.5 Grating Reflector & Direct-Bragg Coupling

2.5.1 Theory

Grating reflectors couple an optical waveguide with a diffraction grating to selectively reflect wavelengths at the center of the grating's bandgap while passing other wavelengths through the structure [61]. Grating reflectors form the primary structural component found in passive devices such as optical filters [69], [70], frequency selective couplers [59], [60], [71], channel-dropping filters [62]–[64], distributed feedback lasers [4], [5], [35], [38].

A schematic for a grating reflector is shown in Fig. 2.3 where direct-Bragg coupling is formed between the forward-traveling mode $a^+(z)$ and backward-traveling mode $a^-(z)$ shown symbolically as the blue arrow. The diffraction grating has a grating period of Λ establishing the Bragg wavelength $\beta_\Lambda = \pi/\Lambda$ as described in the sections above.

The Electric Field

The electric field expression for the grating-reflector shown in Fig. 2.3 is written as:

$$\mathbf{E}(x,y,z) = a^+(z)\mathbf{e}_a(x,y)e^{+i\beta_p z} + a^-(z)\mathbf{e}_a(x,y)e^{+i\beta_{-p} z}, \tag{2.27}$$

where $a^{\pm}(z)$ are the longitudinal field envelopes, $\mathbf{e}_a(x,y)$ are the normalized transverse mode profiles, β_p is the wavenumber of the forward-traveling mode, and β_{-p} is the wavenumber of the backward-traveling mode. As shown in earlier sections, $\beta_{-p} = -\beta_p$, allowing the introduction of $\beta_a \equiv \beta_p$, such that:

$$\mathbf{E}(x,y,z) = a^{+}(z)\mathbf{e}_a(x,y)e^{+i\beta_a z} + a^{-}(z)\mathbf{e}_a(x,y)e^{-i\beta_a z}, \tag{2.28}$$

where $\beta_a = 2\pi n_a/\lambda_0$ is the wavenumber of the transverse-mode associated with the A waveguide, n_a is the effective refractive index of the A waveguide, and λ_0 is the wavelength.

Coupled-Mode Equations

The two coupled-mode equations for the grating reflector can be written directly from the CME definition in Eq. (2.17) as:

$$\begin{aligned}\frac{da^{+}(z)}{dz} &= i\,\mathrm{sgn}(\mathbb{S}_{+})\left(a^{+}(z)\kappa_{aa} + a^{-}(z)e^{-i(\beta_p-\beta_{-p})z}\kappa_{aa}\right),\\ \frac{da^{-}(z)}{dz} &= i\,\mathrm{sgn}(\mathbb{S}_{-})\left(a^{+}(z)e^{-i(\beta_{-p}-\beta_p)z}\kappa_{aa} + a^{-}(z)\kappa_{aa}\right),\end{aligned} \tag{2.29}$$

where the sgn function returns the sign associated with the mode's direction of power flow, captured by the exponent in the given mode notation, such that, $\mathrm{sgn}(\mathbb{S}_{+}) = +1$ and $\mathrm{sgn}(\mathbb{S}_{-}) = -1$.

Recalling again that $\beta_a \equiv \beta_p = -\beta_{-p}$, the coupled-mode equations can be rewritten as:

$$\begin{aligned}\frac{da^{+}(z)}{dz} &= i\,\mathrm{sgn}(\mathbb{S}_{+})\left(a^{+}(z)\kappa_{aa} + a^{-}(z)e^{-i(\beta_a+\beta_a)z}\kappa_{aa}\right),\\ \frac{da^{-}(z)}{dz} &= i\,\mathrm{sgn}(\mathbb{S}_{-})\left(a^{+}(z)e^{-i(-\beta_a-\beta_a)z}\kappa_{aa} + a^{-}(z)\kappa_{aa}\right),\end{aligned} \tag{2.30}$$

and further simplified as:

$$\begin{aligned}\frac{da^+(z)}{dz} &= i\left(a^+(z)\kappa_{aa} + a^-(z)e^{-i2\beta_a z}\kappa_{aa}\right),\\ \frac{da^-(z)}{dz} &= -i\left(a^+(z)e^{i2\beta_a z}\kappa_{aa} + a^-(z)\kappa_{aa}\right).\end{aligned} \tag{2.31}$$

Direct-Bragg Coupling Coefficients

The quantity κ_{aa} represents the coupling between any two modes pairs $\{a^\pm(z), a^\pm(z)\}$, each due to the presence of the diffraction-grating which has a grating period of Λ and a grating depth of h. The diffraction-grating's relative permittivity profile is defined as:

$$\Delta\bar{\varepsilon}(x,z) = u(x)\Delta\bar{\varepsilon}(z) \tag{2.32}$$

where

$$u(x) = \begin{cases} 1 & \text{for } |x - d/2| < h/2 \\ 0 & \text{otherwise} \end{cases}, \tag{2.33}$$

where $d/2$ is the fixed height of the unperturbed waveguide, x is the transverse-profile dimension, and z is the direction of propagation. The permittivity changes due to the diffraction grating are given through the cosine expansion:

$$\Delta\bar{\varepsilon}(z) = \Delta\bar{\varepsilon}_1 \cos\frac{2\pi}{\Lambda}z + \Delta\bar{\varepsilon}_2 \cos\frac{4\pi}{\Lambda}z + \cdots + \Delta\bar{\varepsilon}_p \cos\frac{2\pi p}{\Lambda}z, \tag{2.34}$$

where, for a rectangular shaped grating,

$$\Delta\bar{\varepsilon}_m = \begin{cases} \frac{4(\bar{\varepsilon}_2 - \bar{\varepsilon}_1)}{\pi m}(-1)^{\frac{m-1}{2}} & \text{m odd} \\ 0 & \text{m even} \end{cases}, \tag{2.35}$$

$\bar{\varepsilon}_2 = \varepsilon_2/\varepsilon_0$ is the diffraction grating relative permittivity, $\bar{\varepsilon}_1 = \varepsilon_1/\varepsilon_0$ is the cladding relative permittivity, ε_2 is the diffraction-grating permittivity, ε_1 is the cladding permittivity, and ε_0 is the permittivity of free space.

Considering only the first harmonic of the cosine expansion as an approximation, the relative change in permittivity becomes

$$\Delta\bar{\varepsilon}(z) = \Delta\bar{\varepsilon}_1 \cos\frac{2\pi}{\Lambda}z. \tag{2.36}$$

If the grating height is h is small then the transverse mode profile $\mathbf{e_a}$ can be assumed constant over the region of integration. The field value for each mode as a result of the integration, is equal to the respective field value at $x = d/2$.

Using the cosine-expansion approximation above and the definition in Eq. (2.21), the coupling coefficient κ_{aa} can be written as:

$$\kappa_{aa} = \frac{\omega\varepsilon_0}{2}\int\limits_{-\infty}^{\infty}\int\limits_{-\infty}^{\infty} \Delta\bar{\varepsilon}_1 \cos\left(\frac{2\pi z}{\Lambda}\right) \mathbf{e_a}(x,y)\cdot\mathbf{e}^*_{\mathbf{a}}(x,y)\; dy\; dx, \tag{2.37}$$

$$= \frac{\omega\varepsilon_0}{2}\Delta\bar{\varepsilon}_1 \cos\left(\frac{2\pi z}{\Lambda}\right)\int\limits_{-\infty}^{\infty}\int\limits_{-\infty}^{\infty} |\mathbf{e_a}(x,y)|^2\; dy\; dx, \tag{2.38}$$

$$= \frac{\omega\varepsilon_0}{2}\Delta\bar{\varepsilon}_1 \cos\left(\frac{2\pi z}{\Lambda}\right)\int_0^W \int_{(d-h)/2}^{(d+h)/2} |\mathbf{e_a}(x,y)|^2\; dy\; dx, \tag{2.39}$$

$$= C_{aa}\cos\left(\frac{2\pi z}{\Lambda}\right) \tag{2.40}$$

$$= C_{aa}\cos(2\beta_\Lambda z) \tag{2.41}$$

where, using Eq. (2.35) with $m = 1$ to isolate the first harmonic, yields:

$$C_{aa} = \frac{\omega\varepsilon_0}{2}\Delta\bar{\varepsilon}_1 \int_0^W \int_{(d-h)/2}^{(d+h)/2} |\mathbf{e_a}(x,y)|^2\;\; dy\; dx, \tag{2.42}$$

and

$$\beta_\Lambda = \frac{\pi}{\Lambda}. \tag{2.43}$$

As in general, $\bar{\varepsilon} = n^2$, the coupling coefficient becomes:

$$C_{aa} = \frac{\omega \varepsilon_0 \Delta n'}{2} \int_0^W \int_{(d-h)/2}^{(d+h)/2} |\mathbf{e_a}(x,y)|^2 \ \ dy\, dx, \tag{2.44}$$

where

$$\Delta n' = \frac{4(n_2^2 - n_1^2)}{\pi}, \tag{2.45}$$

n_1 is the refractive index of the cladding, and n_2 is the refractive index of the grating.

All three remaining direct-Bragg coupling coefficients follow the identical derivation shown above and will have a similar final expression.

Introduction of Coupling Coefficients into CMEs

Substituting the coupling coefficient definition in Eq. (2.41), the CMEs for the grating reflector become

$$\begin{aligned} \frac{da^+(z)}{dz} &= i\left(a^+(z) C_{aa} \cos(2\beta_\Lambda z) + a^-(z) e^{-i2\beta_a z} C_{aa} \cos(2\beta_\Lambda z)\right), \\ \frac{da^-(z)}{dz} &= -i\left(a^+(z) e^{i2\beta_a z} C_{aa} \cos(2\beta_\Lambda z) + a^-(z) C_{aa} \cos(2\beta_\Lambda z)\right). \end{aligned} \tag{2.46}$$

The isolated cos expressions will integrate out becoming zero valued, leaving:

$$\begin{aligned} \frac{da^+(z)}{dz} &= i a^-(z) e^{-i2\beta_a z} C_{aa} \cos(2\beta_\Lambda z), \\ \frac{da^-(z)}{dz} &= -i a^+(z) e^{i2\beta_a z} C_{aa} \cos(2\beta_\Lambda z), \end{aligned} \tag{2.47}$$

The wavenumber exponent $e^{\pm i2\beta_a z}$, in conjuction with the remaining cos on the right-hand side, produces slow-moving content when the waveguide wavenumber β_a is close to the Bragg wavenumber β_Λ. This can be seen by writing the cosine in the exponential form

$$\cos(2\beta_\Lambda z) = \frac{e^{i2\beta_\Lambda z} + e^{-i2\beta_\Lambda z}}{2}, \tag{2.48}$$

and distributing the waveguide wavenumber exponent through the expansion of Eq. (2.47) to become:

$$\begin{aligned} \frac{da^+(z)}{dz} &= ia^-(z)C_{aa}\frac{e^{-i2(\beta_a-\beta_\Lambda)z} + e^{-i2(\beta_a+\beta_\Lambda)z}}{2}, \\ -\frac{da^-(z)}{dz} &= ia^+(z)C_{aa}\frac{e^{i2(\beta_a+\beta_\Lambda)z} + e^{i2(\beta_a-\beta_\Lambda)z}}{2}. \end{aligned} \tag{2.49}$$

Defining the wavenumber detuning and wavenumber mean valued quantities

$$\Delta\beta_a = \beta_a - \beta_\Lambda, \tag{2.50a}$$

$$\bar{\beta}_a = \frac{\beta_a + \beta_\Lambda}{2}, \tag{2.50b}$$

results in the CMEs

$$\begin{aligned} \frac{da^+(z)}{dz} &= ia^-(z)\frac{C_{aa}}{2}\left(e^{-i2\Delta\beta_a z} + e^{-i4\bar{\beta}_a z}\right), \\ -\frac{da^-(z)}{dz} &= ia^+(z)\frac{C_{aa}}{2}\left(e^{i4\bar{\beta}_a z} + e^{i2\Delta\beta_a z}\right). \end{aligned} \tag{2.51}$$

The Bragg condition is met when $\beta_a = \beta_\Lambda$, where the guided longitudinal propagating optical wavefront is optimally reflected back to its opposite longitudinally propagating mode. This Bragg reflection sets up a photonic bandgap within the coupled structure that ultimately hinders light propagation.

As the waveguide wavenumber is a positive quantity, the exponents including the $\bar{\beta}_a$

terms will be large such that they integrate out to zero and can be discounted, resulting in:

$$\begin{aligned}\frac{da^+(z)}{dz} &= ia^-(z)\kappa_a e^{-i2\Delta\beta_a z},\\ -\frac{da^-(z)}{dz} &= ia^+(z)\kappa_a e^{i2\Delta\beta_a z},\end{aligned} \tag{2.52}$$

where, from Eq. (2.44):

$$\kappa_a = \frac{C_{aa}}{2} = \frac{\omega\varepsilon_0\Delta n'}{4}\int_0^W \int_{(d-h)/2}^{(d+h)/2} |\mathbf{e_a}(x,y)|^2 \;\; dy\, dx. \tag{2.53}$$

This derivation of the Bragg detuning and the Bragg-coupling coefficient is applicable throughout the remainder of this dissertation for *all* Bragg-based coupling mechanisms presented.

Solution using an Ansatz Approach

Though the CMEs Eq. (2.52) can be solved using rotated-frames and eigenvalues, an alternate solution method using an *ansatz* approach will be instead demonstrated. Using this method, a general solution to the CMEs is assumed to take the form

$$a^+(z) = a_0^+ e^{i\theta_+ z}, \tag{2.54a}$$

$$a^-(z) = a_0^- e^{i\theta_- z}, \tag{2.54b}$$

where $a_0^\pm$ and $\theta_\pm$ are both complex constants. These assumed solutions are propagated through the CMEs in Eq. (2.76) to arrive at

$$i\theta_+ a_0^+ e^{i\theta_+ z} = \kappa_a e^{-i2\Delta\beta_a z} a_0^- e^{i\theta_- z}, \tag{2.55a}$$

$$i\theta_- a_0^- e^{i\theta_- z} = \kappa_a e^{i2\Delta\beta_a z} a_0^+ e^{i\theta_+ z}. \tag{2.55b}$$

Moving the exponents to the right-hand side:

$$i\theta_+ a_0^+ = \kappa_a e^{-i2\Delta\beta_a z} a_0^- e^{i\theta_- z} e^{-i\theta_+ z}, \tag{2.56a}$$

$$i\theta_- a_0^- = \kappa_a e^{i2\Delta\beta_a z} a_0^+ e^{i\theta_+ z} e^{-i\theta_- z}, \tag{2.56b}$$

consolidating,

$$i\theta_+ a_0^+ = \kappa_a a_0^- e^{-i(2\Delta\beta_a + \theta_+ - \theta_-)z}, \tag{2.57a}$$

$$i\theta_- a_0^- = \kappa_a a_0^+ e^{i(2\Delta\beta_a + \theta_+ - \theta_-)z}, \tag{2.57b}$$

and diving through by the imaginary coefficient provides:

$$\theta_+ a_0^+ = -i\kappa_a a_0^- e^{-i(2\Delta\beta_a + \theta_+ - \theta_-)z}, \tag{2.58a}$$

$$\theta_- a_0^- = -i\kappa_a a_0^+ e^{i(2\Delta\beta_a + \theta_+ - \theta_-)z}. \tag{2.58b}$$

For a solution to the CMEs to be valid, it must be valid for *all* value of z [68]. This can only occur if the exponents of Eq. (2.58b) are themselves zero valued, implying

$$2\Delta\beta_a + \theta_- - \theta_+ = 0, \tag{2.59}$$

providing the relationship

$$\theta_- = \theta_+ - 2\Delta\beta_a. \tag{2.60}$$

Under this condition Eq. (2.58b) reduces to simply become

$$\theta_+ a_0^+ = -i\kappa_a a_0^-, \tag{2.61a}$$

$$\theta_- a_0^- = -i\kappa_a a_0^+. \tag{2.61b}$$

The relationship in Eq. (2.60) is substituted into Eq. (2.61b) to arrive at:

$$(\theta_+ - 2\Delta\beta_a)a_0^- = -i\kappa_a a_0^+. \tag{2.62}$$

Both sides of Eq. (2.62) are multiplied by θ_+ to produce:

$$\theta_+^2 a_0^- - 2\Delta\beta_a\ \theta_+ a_0^- = -i\kappa_a \theta_+ a_0^+. \tag{2.63}$$

The right-hand side of the above expression contains a $\theta_+ a_0^+$ which can be eliminated using the definition in Eq. (2.61a):

$$\theta_+^2 a_0^- - 2\Delta\beta_a\ \theta_+ a_0^- = -i\kappa_a(-i\kappa_a a_0^-) = -\kappa_a^2 a_0^-. \tag{2.64}$$

The unknown constant a_0^- can be divided out and all terms brought to the left-hand side to reveal a quadratic polynomial in θ_+:

$$\theta_+^2 - 2\Delta\beta_a\ \theta_+ a_0^- + \kappa_a^2 a_0^- = 0. \tag{2.65}$$

The roots of this quadratic produce values for θ_+ as:

$$\theta_+ = \Delta\beta_a \mp \sqrt{\Delta\beta_a^2 - \kappa_a^2}. \tag{2.66}$$

The value of θ_- can be then found using the relationship Eq. (2.60) to arrive at:

$$\theta_- = -\Delta\beta_a \mp \sqrt{\Delta\beta_a^2 - \kappa_a^2}. \tag{2.67}$$

Electric-Field Expressions

The general solutions in $a^+(z)$ and $a^-(z)$ of Eq. (2.54) will be a linear combination of the kernels given by the two expressions for θ_+ and the two expressions for θ_-, respectively:

$$a^+(z) = e^{i\Delta\beta_a z}\left(a_1^+ e^{-i\sqrt{\Delta\beta_a^2-\kappa_a^2}\,z} + a_2^+ e^{i\sqrt{\Delta\beta_a^2-\kappa_a^2}\,z}\right), \tag{2.68a}$$

$$a^-(z) = e^{-i\Delta\beta_a z}\left(a_1^- e^{-i\sqrt{\Delta\beta_a^2-\kappa_a^2}\,z} + a_2^- e^{i\sqrt{\Delta\beta_a^2-\kappa_a^2}\,z}\right), \tag{2.68b}$$

where each $a_n^\pm$ is a complex value which can be found by imposing boundary conditions on the structure.

The electric-field expressions for the grating coupler are

$$a^+(z) = \frac{-2B_1}{\kappa_a e^{-i\eta}}\left(\Delta\beta_a \sinh(i\eta(z-L)) + \eta\cosh(i\eta(z-L))\right), \tag{2.69a}$$

$$a^-(z) = \frac{2B_1}{e^{-i\eta}}\sinh(i\eta(z-L)), \tag{2.69b}$$

where

$$\eta = \sqrt{\Delta\beta_a^2 - \kappa_a^2}, \tag{2.70}$$

and L is the length of the coupling region. The derivation method to arrive at the electric-field expression is fully detailed in Section 2.8 below.

Power, Transmittivity, and Reflectivity Expressions

The power expressions are determined as the magnitude squared of the field expressions and are given as:

$$P_a^+(z) = P_0\frac{\left|\Delta\beta_a \sinh(i\eta(z-L)) + \eta\cosh(i\eta(z-L))\right|^2}{\left|\Delta\beta_a \sinh(-i\eta) + \eta\cosh(-i\eta)\right|^2}, \tag{2.71a}$$

$$P_a^-(z) = P_0\frac{|\kappa_a|^2\left|\sinh(i\eta(z-L))\right|^2}{\left|\Delta\beta_a \sinh(-i\eta) + \eta\cosh(-i\eta)\right|^2}. \tag{2.71b}$$

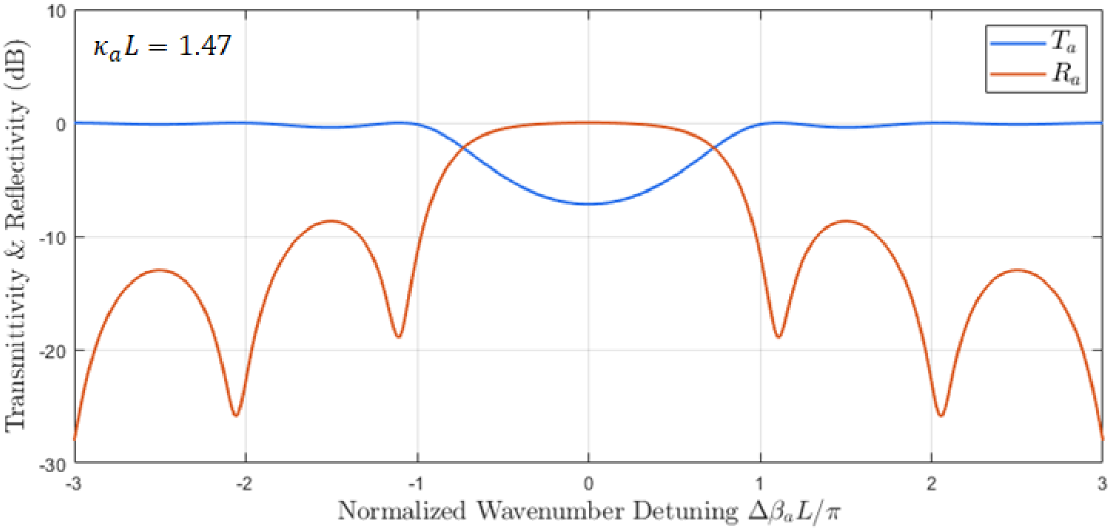

Figure 2.4 The transmittivity T_a and reflectivity R_a of a direct-Bragg grating reflector with a normalized coupling coefficient $\kappa_a L = 1.47$. The photonic bandgap is seen in the transmittivity centered at the normalized wavenumber detuning $\Delta\beta_a L = 0$. The depth and the width of the PBG increases with the Bragg-coupling strength $\kappa_a L$.

The transmittivity of a structure is defined as the ratio of an output power to an input power and, when examined over a change in detuning $\Delta\beta_a$, shows the wavenumber response of the structure. For the grating reflector, the input is taken as $P_a^+(z=0)$, the output is given by $P_a^+(z=L)$, and reflected power as $P_a^-(z=0)$ giving rise to the transmittivity and reflectivity

$$T_a = \frac{P_a^+(z=L)}{P_a^+(z=0)} = \frac{\left|\sqrt{\Delta\beta_a^2-\kappa_a^2}\right|^2}{\left|\Delta\beta_a \sinh\left(-i\sqrt{\Delta\beta_a^2-\kappa_a^2}\right)+\sqrt{\Delta\beta_a^2-\kappa_a^2}\cosh\left(-i\sqrt{\Delta\beta_a^2-\kappa_a^2}\right)\right|^2}, \tag{2.72a}$$

$$R_a = \frac{P_a^-(z=0)}{P_a^+(z=0)} = \frac{|\kappa_a|^2\left|\sinh\left(-i\sqrt{\Delta\beta_a^2-\kappa_a^2}\right)\right|^2}{\left|\Delta\beta_a \sinh\left(-i\sqrt{\Delta\beta_a^2-\kappa_a^2}\right)+\sqrt{\Delta\beta_a^2-\kappa_a^2}\cosh\left(-i\sqrt{\Delta\beta_a^2-\kappa_a^2}\right)\right|^2}. \tag{2.72b}$$

2.5.2 Behavior

Plotting the transmittivity T_a as over waveguide detuning $\Delta\beta_a$ for a constant coupling κ_a results in the transmittivity spectrum shown in Fig. 2.4. The counter-directional Bragg-coupling processes of the grating reflector produces a photonic bandgap (PBG) centered at the waveguide detuning value $\Delta\beta_a = 0$. The width and depth of the PBG is established by the coupling strength which, for an index grating, is itself a function of the separation of the diffraction grating to the coupled waveguide, the grating width and depth, and the grating material index. The center of the PBG is characterized by a low transmittivity T_a through the structure as seen in Fig. 2.4. The power in this band of detuning is efficiently coupled into the $a^-(z)$ field and appears as a reflected signal as seen by the reflectivity R_a in Fig. 2.4. The wings of the transmittivity become 0 dB outside the photonic bandgap for a lossless waveguide, indicating that the device is transparent at values of wavenumber detuning well away from zero. For the lossless passive structure the sum of the transmittivity and reflectivity must be unity. The symmetrical solution for $a^-(z)$ injection at $z = L$ mirrors this response and is not detailed here.

2.6 Traditional DFB Laser & Direct-Bragg Coupling

2.6.1 Theory

Distributed feedback (DFB) lasers utilizing a uniform grating to generate direct-Bragg coupling between the forward and backward modes of an adjacent *active* waveguide as depicted in Fig. 2.5(a) [4]. The electric field expressions are written as:

$$\mathbf{E}(x,y,z) = a^+(z)\mathbf{e}_a(x,y)e^{+i\beta_p z} + a^-(z)\mathbf{e}_a(x,y)e^{+i\beta_{-p} z}, \tag{2.73}$$

where $a^{\pm}(z)$ are the longitudinal field envelopes, $\mathbf{e}_a(x,y)$ is the normalized transverse mode profile, and $\beta_{\pm p}$ are the wavenumbers associated with the forward- and backward-

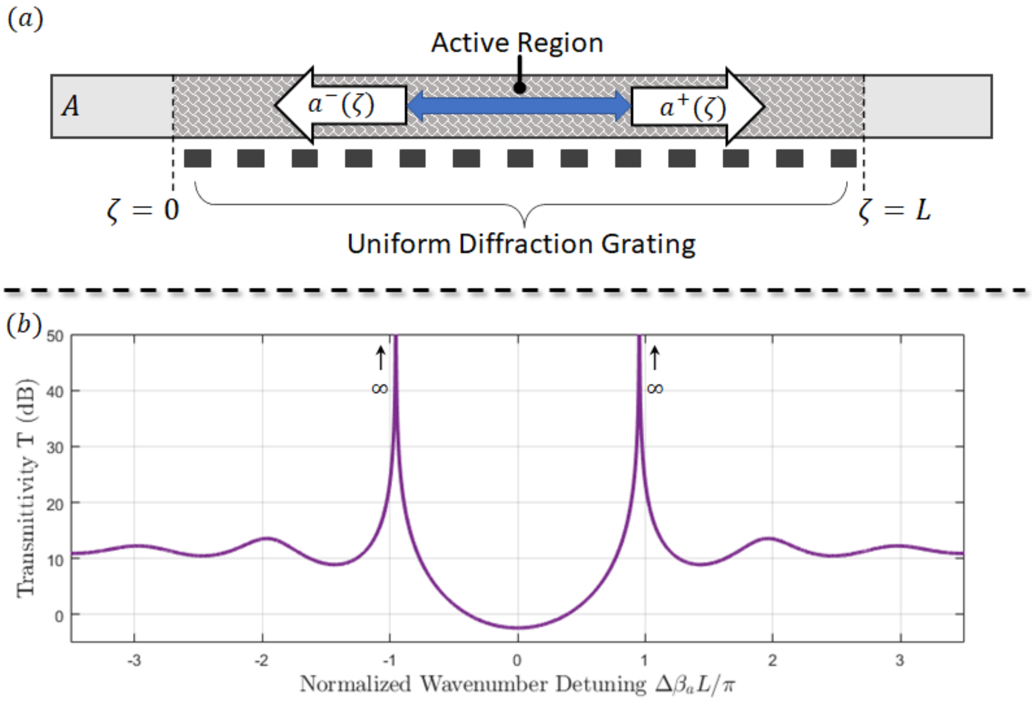

Figure 2.5 The uniform-grating distributed feedback (DFB) laser structure and mode spectrum demonstrating the mode degeneracy. (a) Adding an active region to the grating reflector provides for optical gain and, with the feedback provided by the diffraction grating, forms a DFB laser. (b) Increasing gain gL in the active region demonstrates resonant behavior in the direct-Bragg coupled structure. Lasing occurs at a gain threshold $gL = g_{th}L$ where two degenerate lasing modes are formed separated from the center of the photonic bandgap. The structure shown has a normalized coupling coefficient $\kappa_a L = 1.47$, and lasing occurs at a gain $gL = g_{th}L = 2.61$.

propagating modes respectively. Substituting $\beta_a \equiv \beta_p = -\beta_{-p}$ equivalently yields

$$\mathbf{E}(x,y,z) = a^+(z)\mathbf{e}_a(x,y)e^{+i\beta_a z} + a^-(z)\mathbf{e}_a(x,y)e^{-i\beta_a z}, \tag{2.74}$$

where $\beta_a = 2\pi n_a/\lambda_0$ is the wavenumber of the transverse mode associated with the A waveguide, n_a is the effective refractive index of the A waveguide, and λ_0 is the wavelength.

Coupled-Mode Equations

The CMEs describing lasing behavior follow from those of the grating reflector in Eq. (2.52) and are written as:

$$\frac{da^+}{dz} = i\,\mathrm{sgn}(\mathbb{S}_+)\kappa_a a^-(z)e^{-i2\Delta\tilde{\beta}_a z}, \tag{2.75a}$$

$$\frac{da^-}{dz} = i\,\mathrm{sgn}(\mathbb{S}_-)\kappa_a a^+(z)e^{i2\Delta\tilde{\beta}_a z}, \tag{2.75b}$$

where sgn returns the sign associated with the direction of modal power flow, $\Delta\tilde{\beta}_a = \tilde{\beta}_a - \beta_\Lambda$ is the complex wavenumber detuning, $\tilde{\beta}_a = (\beta_a - ig/2)$ is the complex wavenumber, $\beta_a = 2\pi n_a/\lambda_0$ is the wavenumber, n_a is the effective refractive index of the A waveguide, $\beta_\Lambda = \pi/\Lambda$ is the Bragg wavenumber, g is the gain coefficient, and κ_a is the direct-Bragg coupling coefficient. Expressions for the coupling coefficients remain unchanged from the grating coupler example above as the only modification to the structure is the inclusion of an active region into the optical waveguide.

Evaluating the sgn function and pulling the resulting sign to the left-hand side results in:

$$\frac{da^+}{dz} = i\kappa_a a^-(z)e^{-i2\Delta\tilde{\beta}_a z}, \tag{2.76a}$$

$$-\frac{da^-}{dz} = i\kappa_a a^+(z)e^{i2\Delta\tilde{\beta}_a z}. \tag{2.76b}$$

A rotated-frame form of the coupled-mode equations can be generated by propagating the rotated-envelope expressions from Eq. (2.20), rewritten here as

$$a^+(z) = \hat{a}^+(z)e^{-i\Delta\beta_a z}, \tag{2.77a}$$

$$a^-(z) = \hat{a}^-(z)e^{+i\Delta\beta_a z}, \tag{2.77b}$$

through the CMEs of Eq. (2.76). Performing this substitution and simplifying eliminates the common exponential and results in a set of linear differential equations in the rotated frame:

$$\frac{d\hat{a}^+}{dz} = i\Delta\tilde{\beta}_a \hat{a}^+ + i\kappa_a \hat{a}^-, \tag{2.78a}$$

$$-\frac{d\hat{a}^-}{dz} = i\Delta\tilde{\beta}_a \hat{a}^- + i\kappa_a \hat{a}^+. \tag{2.78b}$$

A normalized length quantity $\zeta = z/L$ is now introduced. Normalizing in this manner also normalizes all coefficient values to unitless quantities such that the CMEs in Eq. (2.78) become

$$\frac{d\hat{a}^+}{d\zeta} = i\Delta\tilde{\beta}_a L\hat{a}^+ + i\kappa_a L\hat{a}^-, \tag{2.79a}$$

$$-\frac{d\hat{a}^-}{d\zeta} = i\Delta\tilde{\beta}_a L\hat{a}^- + i\kappa_a L\hat{a}^+. \tag{2.79b}$$

It is typical to analyze structures and present their associated quantities in a normalized form and, unless stated otherwise, will be done so moving forward.

Direct-Bragg Coupling Coefficients

The coupling coefficients for the uniform-grating DFB lasing structure are unchanged from the grating reflector. Details for their derivation can be found in that section and will not be repeated here.

Solution using an Eigenvalue Approach

The CMEs in Eqs. (2.79) can be written in a matrix form as:

$$\frac{d\vec{v}}{d\zeta} = \mathbb{A}\vec{v}, \tag{2.80}$$

where

$$\vec{v} = \begin{bmatrix} \hat{a}^+ \\ \hat{a}^- \end{bmatrix}, \tag{2.81}$$

is the slow-moving envelope vector and $\mathbb{A}$ is the characteristic matrix or Hamiltonian matrix of the DFB laser, given as

$$\mathbb{A} = \begin{bmatrix} i\Delta\tilde{\beta}_a L & i\kappa_a L \\ -i\kappa_a L & -i\Delta\tilde{\beta}_a L \end{bmatrix}. \tag{2.82}$$

The eigenvalues of the $\mathbb{A}$ matrix are

$$q_1 = +i\sqrt{\left(\Delta\beta_a L - i\frac{gL}{2}\right)^2 - (\kappa_a L)^2} \tag{2.83a}$$

$$q_2 = -i\sqrt{\left(\Delta\beta_a L - i\frac{gL}{2}\right)^2 - (\kappa_a L)^2}. \tag{2.83b}$$

The eigenvalues displayed here align with the ansatz approach results for the grating coupler shown in Eq. (2.66), understanding that the leading $e^{i\Delta\beta_a z}$ term, seen in Eq. (2.68) term of the ansatz approach, is the frame rotation pulled out to arrive at the linear CMEs above. Furthermore, the imaginary term preceding the square-root of the eigenvalues above is explicitly written in the original ansatz exponent of Eq. (2.54), and the complex detuning for the DFB laser includes the normalized gain coefficient gL unlike the passive grating coupler.

Electric-Field Expressions

The field expressions for the DFB laser are again similar to the grating coupler and are written as:

$$a^+(\zeta) = \frac{-2B_1}{\kappa_a L e^{-i\tilde{\eta}L}} \left(\tilde{\psi}L \sinh(i\tilde{\eta}L(\zeta-1)) + \tilde{\eta}L \cosh(i\tilde{\eta}L(\zeta-1))\right), \tag{2.84a}$$

$$a^-(\zeta) = \frac{2B_1}{e^{-i\tilde{\eta}L}} \sinh(i\tilde{\eta}L(\zeta-1)), \tag{2.84b}$$

where now

$$\tilde{\eta}L = \sqrt{(\tilde{\psi}L)^2 - (\kappa_a L)^2}, \tag{2.85a}$$

$$\tilde{\psi}L = (\Delta\beta_a L - igL/2). \tag{2.85b}$$

Power, Transmittivity, and Reflectivity Expressions

The unidirectional modal power expressions for the DFB laser are given by the magnitude squared of the field expressions:

$$P_a^+(\zeta) = P_0 \frac{|\tilde{\psi}L\sinh(i\tilde{\eta}L(\zeta-1)) + \tilde{\eta}L\cosh(i\tilde{\eta}L(\zeta-1))|^2}{|\tilde{\psi}L\sinh(-i\tilde{\eta}L) + \tilde{\eta}L\cosh(-i\tilde{\eta}L)|^2} \tag{2.86a}$$

$$P_a^-(\zeta) = P_0 \frac{|\kappa_a L|^2 |\sinh(i\tilde{\eta}L(\zeta-1))|^2}{|\tilde{\psi}L\sinh(-i\tilde{\eta}L) + \tilde{\eta}L\cosh(-i\tilde{\eta}L)|^2}, \tag{2.86b}$$

The longitudinal power profile within the laser cavity is the sum of the unidirectional modal powers, where carrier diffusion is assumed to fill any longitudinal interference pattern: [4], [5], [35]:

$$\mathbb{P}_a(\zeta) = P_a^+(\zeta) + P_a^-(\zeta). \tag{2.87}$$

A single value capturing the flatness F of the longitudinal power profile within the laser cavity provides an indicator for above-threshold lasing stability and is defined as

$$F = \int_0^1 (\mathbb{P}_A(\zeta) - \mu)^2/\mu^2, \tag{2.88}$$

where $\mu = \int_0^1 \mathbb{P}_A(\zeta)\, d\zeta$ [35]. High values of F indicate peaky longitudinal power profiles which may negatively impact above-threshold lasing performance. Lasing structures with low values of F are desired to maintain lasing stability for above-threshold operation.

The transmittivity and reflectivtity of the uniform grating DFB laser then becomes:

$$T_a = \frac{|\tilde{\eta}L|^2}{|\tilde{\psi}L\sinh(-i\tilde{\eta}L) + \tilde{\eta}L\cosh(-i\tilde{\eta}L)|^2}, \tag{2.89a}$$

$$R_a = \frac{|\kappa_a L|^2\,|\sinh(-i\tilde{\eta}L)|^2}{|\tilde{\psi}L\sinh(-i\tilde{\eta}L) + \tilde{\eta}L\cosh(-i\tilde{\eta}L)|^2}. \tag{2.89b}$$

When the uniform-grating DFB laser is brought to lasing threshold by increasing gain gL, the transmittivity demonstrates degenerate modes on either side of the photonic bandgap as seen in Fig. 2.5(b). Such a degeneracy results in a laser with no gain margin and, by extension, is not single mode [4].

Transcendental Lasing Conditions

Lasing occurs when the transmittivity expression goes to infinity which happens when the denominator of Eq. (2.89a) becomes zero or, equivalently, when

$$\tilde{\psi}_{th}L\sinh(i\tilde{\eta}_{th}L) = \tilde{\eta}_{th}L\cosh(i\tilde{\eta}_{th}L), \tag{2.90}$$

where the "$_{th}$" subscript denotes a lasing threshold value. Expanding the square of Eq. (2.90), applying Eqs. (2.85), and using the identity $\cosh^2 x - \sinh^2 x = 1$ yields, after some manipulation,

$$\frac{g_{th}L}{2} + i\Delta\beta_{th}L = \pm i\kappa_a L\cosh(i\tilde{\eta}_{th}L). \tag{2.91}$$

Substitution of Eq. (2.91) back into Eq. (2.90) ultimately generates the following transcendental equation relating $\tilde{\eta}_{th}L$ to the normalized coupling coefficient $\kappa_a L$:

$$\kappa_a L = \pm\frac{\tilde{\eta}_{th}L}{\sinh(i\tilde{\eta}_{th}L)}. \tag{2.92}$$

The solution pairs $\{\kappa_a L,\ \tilde{\eta}_{th}L\}$ are found from Eq. (2.92) by using a numerical solver.

These solution pairs are then fed into the right-hand side of Eq. (2.91), and the real and imaginary parts are used to determine $g_{th}L$ and $\Delta\beta_{th}L$. These threshold gain $g_{th}L$ and wavenumber detuning $\Delta\beta_{th}L$ pairs across a span of coupling coefficient values $\kappa_a L$ collectively form a mode spectrum.

Alternatively, for a fixed $\kappa_a L$, threshold pairs can be found by ramping the gain coefficient gL up from zero until the transmittivity, as plotted across wavenumber detuning $\Delta\beta_a L$, reaches infinity. The gain value and associated wavenumber detuning when this occurs provides for the first threshold pair. Additional threshold pairs are found by continuing to increase the structure's gain past the previous threshold value. Either approach will yield the collection of all threshold pairs for a span of coupling $\kappa_a L$ and provides the mode spectrum seen in Fig. 1.1(b).

The quantity of gain margin is defined as

$$\Delta\alpha L = (g_{th_2}L - g_{th}L)/2, \tag{2.93}$$

where $g_{th}L$ is the fundamental lasing-mode's gain threshold value and $g_{th_2}L$ is the next-highest lasing-mode's gain threshold value. Large values of gain margin provide an indication of above-threshold single-mode lasing stability. Values for gain margin across direct-Bragg coupling for the $\lambda/4$-shifted DFB laser are shown in Fig. 1.3 and peak with a value $\Delta\alpha L = 0.735$.

Transfer-Matrix Method

Closed-form expressions do not exists for some structures which include grating non-uniformities. For such structures, alternate methods must be used to find quantities like threshold gain, electric-fields, longitudinal powers, and transmittivity. One such method is the transfer-matrix method (TMM) which breaks non-uniform structures into smaller approximately uniform segments of normalized length $\ell = 1/N$, where N is the number of

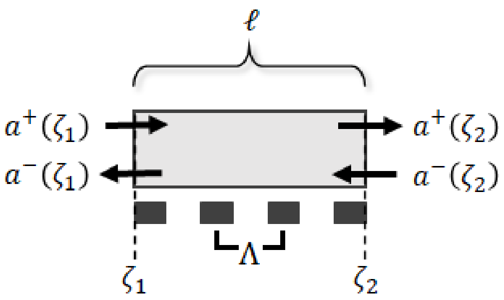

Figure 2.6 An approximately uniform section of a non-uniform DFB lasing structure. The uniform section is defines the transfer-matrix method used to model the non-uniform structure.

TMM segments used to model the structure.

For a photonic waveguide with a forward-traveling wave $a^+(\zeta)$ and a reverse-traveling wave $a^-(\zeta)$, the transform operation is given by:

$$\begin{bmatrix} a^+(\zeta_2) \\ a^-(\zeta_2) \end{bmatrix} = \begin{bmatrix} t_{11} & t_{12} \\ t_{21} & t_{22} \end{bmatrix} \begin{bmatrix} a^+(\zeta_1) \\ a^-(\zeta_1). \end{bmatrix} \tag{2.94}$$

The values of t_{jk} capture the self and cross-coupling values of the two slow-moving envelopes as they propagate through the region described by the matrix. The transfer matrix will be denoted as T and its elements as t_{jk}. As long as the region captured by T is approximately uniform and has a length much greater than the optical wavelength traversing the region, $\ell >> \lambda$, then the transfer produces meaningful results. Schematically this is shown for a section with a diffraction-grating period Λ in Fig. 2.6.

For the DFB lasing structure, the elements of T have been provided elsewhere and are given as [72]:

$$t_{11} = \frac{1}{1-(r\ell)^2}\left[e^{i\tilde{\eta}\ell} - (r\ell)^2 e^{-i\tilde{\eta}\ell}\right] \tag{2.95a}$$

$$t_{12} = -t_{21} = \frac{r\ell}{1-(r\ell)^2}\left[e^{i\tilde{\eta}\ell} - e^{-i\tilde{\eta}\ell}\right] \tag{2.95b}$$

$$t_{22} = \frac{1}{1-(r\ell)^2}\left[e^{-i\tilde{\eta}\ell} - (r\ell)^2 e^{i\tilde{\eta}\ell}\right] \tag{2.95c}$$

The value of $\tilde{\eta}\ell = \tilde{\eta}L/N$ where $\tilde{\eta}L$ is given in Eq. (2.85a). The reflection coefficients $r\ell$ are defined as

$$r\ell = \frac{\tilde{\eta}\ell - \tilde{\psi}\ell}{\kappa_a \ell} = -\frac{\kappa_a \ell}{\tilde{\eta}\ell + \tilde{\psi}\ell} \tag{2.96}$$

where $\tilde{\psi}\ell = \tilde{\psi}L/N$ and $\tilde{\psi}L$ is given in Eq. (2.85b) [72].

The transfer-matrix method divides the larger, non-uniform structure into smaller approximately linear segments. The structure taken in its entirety could have parameters which are variable with ζ or which induce nonlinearities impacting behaviors along the length of the waveguide. When segmented as described, the structure behaviors are determined through a linear combination of transforms for each approximately uniform segment. For system which does not include nonlinearities but does exhibit ζ dependent nonuniformities, the total system response is simply the product of the individual transfer matrices:

$$\begin{bmatrix} a^{+}(\zeta_N) \\ a_{-}(\zeta_N) \end{bmatrix} = T_1\, T_2 \ldots T_N \begin{bmatrix} a^{+}(\zeta_1) \\ a^{-}(\zeta_1) \end{bmatrix} = \prod_{n=1}^{N} T_n \begin{bmatrix} a^{+}(\zeta_1) \\ a^{-}(\zeta_1). \end{bmatrix} \tag{2.97}$$

In case where nonlinearities are involved, iterative methods are required. The linear system is first solved as described above with a initial set of values which do not consider the nonlinearities of the system. This solution provides a seed set of parameters for each segment in the structure and are used to isolate the first-order approximation of behaviors within each segment. These first-order approximations are used to calculate structure parameters which are dependent upon the nonlinearities. The transfer-matrix elements are updated once the impact of the nonlinearities on structure parameters is understood.

The above process represents one full iteration of the transfer-matrix method (TMM) when considering nonlinear effects. The transfer matrix elements, after a complete pass, will contain the second-order approximation of the nonlinear effects. The process repeats until all calculated parameters and behaviors converge on a solution with an acceptable error. The final set of equations provide a model for the nonlinear behaviors as well as non-uniformities along the structure longitudinal position ζ.

2.6.2 Behavior

The transmittivity of the uniform-grating DFB laser is shown in Fig. 2.5(b). Two degenerate lasing modes are seen rising to infinity on either side of the photonic bandgap centered at the wavenumber detuning $\Delta\beta_a L = 0$. The threshold gain $g_{th}L$ and the threshold detuning $\Delta\beta_{a_{th}}L$ depend upon the direct-Bragg coupling value $\kappa_a L$. Stronger coupling values increase the resonator strength and lower the gain threshold while also extending the photonic-bandgap width.

For a given direct-Bragg coupling strength, increasing threshold gain past the initial-threshold value $g_{th}L$ exposes other lasing modes in the structure at higher values of gain. Each of these modes is identified by a pair of threshold gain and detuning valued noted as $\{g_{th_m}, \Delta\beta_{th_m}\}$. The collection of all threshold pairs for all modes across all values of $\kappa_a L$ forms the mode spectrum plot shown in Fig. 1.1(b).

The longitudinal power profile, given by the expression in Eq. (2.87), is shown as the black curve in Fig. 1.4(a) and has a low flatness of $F = 0.010$ for a $\kappa_a L = 2.2$, the coupling which results in the largest gain margin for the $\lambda/4$-shifted DFB laser. There is no associated gain margin plot in Fig. 1.4(b) because the uniform-grating DFB laser has a degenerate mode spectrum which guarantees a gain margin $\Delta\alpha L = 0$ for all values of $\kappa_a L$.

Isolating the mode spectrum shown in Fig. 1.2, the gain margin shown in Fig. 1.3, and the longitudinal power profiles shown in Fig. 1.4, or other quantities, each for DFB-lasing structures which include phase shifts or other non-uniformities, requires the use of the transfer-matrix method (TMM) discussed in Section 2.6.1.

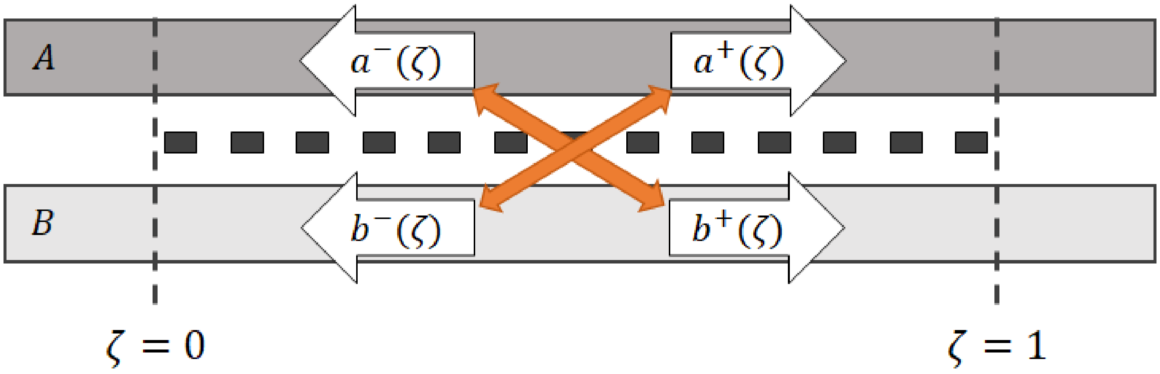

Figure 2.7 The contra-directional coupler utilizes a diffraction grating to couple reflected power across modes of one waveguide to the adjacent waveguide. The wavenumbers associated with each waveguide are not the same and will have an associated detuning $\Delta\beta_{ab}L$.

2.7 Contra-Directional Coupler & Exchange-Bragg Coupling

2.7.1 Theory

The Electric Field

The electric field of contra-directional coupler shown in Fig. 2.7 is written as:

$$\begin{aligned}\mathbf{E}(x,y,\zeta) = a^+(\zeta)\mathbf{e}_a(x,y)e^{+i\beta_p^a L\zeta} + a^-(\zeta)\mathbf{e}_a(x,y)e^{+i\beta_{-p}^a L\zeta} + \\ b^+(\zeta)\mathbf{e}_b(x,y)e^{+i\beta_p^b L\zeta} + b^-(\zeta)\mathbf{e}_b(x,y)e^{+i\beta_{-p}^b L\zeta},\end{aligned} \tag{2.98}$$

where $a^{\pm}(\zeta)$ are the longitudinal field envelopes of the A waveguide, $b^{\pm}(\zeta)$ are the longitudinal field envelopes of the B waveguide, $\mathbf{e}_a(x,y)$ is the transverse mode profile of the A waveguide, $\mathbf{e}_b(x,y)$ is the transverse mode profile of the B waveguide, $\beta_{\pm p}^a$ are the forward- and backward-propagating wavenumbers of the A waveguide, $\beta_{\pm p}^b$ are the forward- and backward-propagating wavenumbers of the B waveguide, and L is the length of the structure.

Making the substitutions $\beta_a \equiv \beta_p^a = -\beta_{-p}^a$ and $\beta_b \equiv \beta_p^b = -\beta_{-p}^b$ where $\beta_a = 2\pi n_a/\lambda_0$ is the wavenumber of the A waveguide, n_a is the effective refractive index of the A waveguide,

$\beta_b = 2\pi n_b/\lambda_0$ is the wavenumber of the B waveguide, n_b is the effective refractive index of the B waveguide, and λ_0 is the wavelength, gives:

$$\begin{aligned}\mathbf{E}(x,y,\zeta) = a^+(\zeta)\mathbf{e}_a(x,y)e^{+i\beta_a L\zeta} + a^-(\zeta)\mathbf{e}_a(x,y)e^{-i\beta_a L\zeta} + \\ b^+(\zeta)\mathbf{e}_b(x,y)e^{+i\beta_b L\zeta} + b^-(\zeta)\mathbf{e}_b(x,y)e^{-i\beta_b L\zeta},\end{aligned} \tag{2.99}$$

Coupled-Mode Equations

For this example, both direct-Bragg and evanescent coupling will be ignored. Focus will be solely on the exchange-Bragg coupling process which defines the contra-directional coupler behaviors. In practice, and as will be seen in future sections, all three coupling processes of direct-Bragg, exchange-Bragg, and evanescent coupling, should simultaneously be considered when analyzing or optimizing structure behaviors.

Following the same derivation process completed for the grating reflector in Section 2.5 and under the provided assumptions so as to isolate the exchange-Bragg coupling process, the four coupled-mode equations for the contra-directional coupler are written as:

$$\begin{aligned}\frac{da^+(\zeta)}{d\zeta} &= i\,\mathrm{sgn}(\mathbb{S}_a^+)\kappa_{\chi ba} L b^-(\zeta)e^{-i2\Delta\beta_\chi L\zeta},\\ \frac{db^+(\zeta)}{d\zeta} &= i\,\mathrm{sgn}(\mathbb{S}_b^+)\kappa_{\chi ab} L a^-(\zeta)e^{-i2\Delta\beta_\chi L\zeta},\\ \frac{da^-(\zeta)}{d\zeta} &= i\,\mathrm{sgn}(\mathbb{S}_a^-)\kappa_{\chi ba} L b^+(\zeta)e^{i2\Delta\beta_\chi L\zeta},\\ \frac{db^-(\zeta)}{d\zeta} &= i\,\mathrm{sgn}(\mathbb{S}_b^-)\kappa_{\chi ab} L a^+(\zeta)e^{i2\Delta\beta_\chi L\zeta},\end{aligned} \tag{2.100}$$

where $\kappa_{\chi(ab,ba)}$ are the exchange-Bragg coupling coefficients detailed in the section below, $\Delta\beta_\chi = \bar{\beta}_{ab} - \beta_\Lambda$ is the exchange detuning, $\bar{\beta}_{ab} = (\beta_a + \beta_b)/2$ is the average waveguide wavenumber of the A and B waveguides, $\beta_\Lambda = \pi/\Lambda$ is the Bragg wavenumber, Λ is the grating period, and L is the grating length.

Executing the sgn function and moving the resulting sign associated with the direction of power flow to the left-hand side provides the final form of the contra-directional coupler CMEs as

$$
\begin{aligned}
\frac{da^{+}(\zeta)}{d\zeta} &= i\kappa_{\chi ba} L b^{-}(\zeta) e^{-i2\Delta\beta_{\chi} L\zeta}, \\
\frac{db^{+}(\zeta)}{d\zeta} &= i\kappa_{\chi ab} L a^{-}(\zeta) e^{-i2\Delta\beta_{\chi} L\zeta}, \\
-\frac{da^{-}(\zeta)}{d\zeta} &= i\kappa_{\chi ba} L b^{+}(\zeta) e^{i2\Delta\beta_{\chi} L\zeta}, \\
-\frac{db^{-}(\zeta)}{d\zeta} &= i\kappa_{\chi ab} L a^{+}(\zeta) e^{i2\Delta\beta_{\chi} L\zeta}.
\end{aligned}
\tag{2.101}
$$

Examining the CMEs in the above set shows that there are two independent *symmetric* pairs of coupled equations, simplifying the solution process. As such, solutions will only be derived and explored for one pair of CMEs; the second set of CMEs will follow the identical solution process and have symmetric behaviors. The clockwise set of CMEs used for the remainder of this section is given by

$$
\begin{aligned}
\frac{da^{+}(\zeta)}{d\zeta} &= i\kappa_{\chi ba} L b^{-}(\zeta) e^{-i2\Delta\beta_{\chi} L\zeta}, \\
-\frac{db^{-}(\zeta)}{d\zeta} &= i\kappa_{\chi ab} L a^{+}(\zeta) e^{i2\Delta\beta_{\chi} L\zeta}.
\end{aligned}
\tag{2.102}
$$

Exchange-Bragg Coupling Coefficients

The exchange-Bragg coupling coefficients are determined as a mode overlap integral between $\mathbf{e}_a$ and $\mathbf{e}_b$ only over the diffraction grating perturbation region. Waveguide perturbations are not necessary for the determination of the exchange-Bragg coupling coefficients and are reserved solely for the evanescent coupling process shown in the next section.

Isolation of each exchange-Bragg coupling coefficient follows the same steps as shown in the direct-Bragg coupling-coefficient derivation in Section 2.5. The exchange-Bragg coupling coefficients in their raw form are written as

$$\kappa_{\chi_{ab}} = \frac{\omega\varepsilon_0\Delta n'}{2}\int_0^W \int_{(d-h)/2}^{(d+h)/2} \mathbf{e_a}(x,y)\cdot\mathbf{e_b^*}(x,y)\;dy\;dx, \tag{2.103a}$$

$$\kappa_{\chi_{ba}} = \frac{\omega\varepsilon_0\Delta n'}{2}\int_0^W \int_{(d-h)/2}^{(d+h)/2} \mathbf{e_b}(x,y)\cdot\mathbf{e_a^*}(x,y)\;dy\;dx, \tag{2.103b}$$

where

$$\Delta n' = \frac{4(n_2^2-n_1^2)}{\pi}, \tag{2.104}$$

where n_2 is the refractive index of the diffraction-grating core, and n_1 is the refractive index of the diffraction-grating cladding. Furthermore, the two expressions in Eq. (2.103) differ only by their integrands which are conjugates of one another, implying $\kappa_{\chi ab} = \kappa_{\chi ba}^*$, such that the CMEs of Eq. (2.102) become:

$$\begin{aligned}\frac{da^+(\zeta)}{d\zeta} &= i\kappa_{\chi ba}Lb^-(\zeta)e^{-i2\Delta\beta_\chi L\zeta},\\ -\frac{db^-(\zeta)}{d\zeta} &= i\kappa_{\chi ba}^*La^+(\zeta)e^{i2\Delta\beta_\chi L\zeta}.\end{aligned} \tag{2.105}$$

Solution using an Ansatz Approach

The contra-directional CMEs in Eq. (2.102) are the same form as the grating reflector, shown in Eq. (2.52), where $a^-(\zeta)\rightarrow b^-(\zeta)$, $\kappa_a L\rightarrow \kappa_{\chi(ab,ba)}L$, and $\Delta\beta_a L\rightarrow\Delta\beta_\chi L$ acts as a quantity mapping between the two structure's CMEs. Taking this approach provides the root solutions as a mapping from Eq. (2.66) as

$$\theta_+ = \Delta\beta_\chi L \mp \sqrt{(\Delta\beta_\chi L)^2 - (\kappa_{\chi ba}L\kappa_{\chi ab}L)}. \tag{2.106}$$

The value of θ_- can be then found using the relationship Eq. (2.60) to arrive at:

$$\theta_- = -(\Delta\beta_\chi L)\mp\sqrt{(\Delta\beta_\chi L)^2-(\kappa_\chi L)^2}, \tag{2.107}$$

where $\kappa_{\chi ba}\ \kappa_{\chi ab} = \kappa_{\chi ba}\ \kappa^*_{\chi ba} = |\kappa_{\chi ba}|^2 = \kappa^2_{\chi}$.

Electric-Field Expressions

The general solutions in $a^+(\zeta)$ and $b^-(\zeta)$ will be a linear combination of the kernels given by the two expressions for θ_+ and the two expressions for θ_-, respectively:

$$a^+(\zeta) = e^{i\Delta\beta_\chi L\zeta}\left(a_1^+ e^{-i\sqrt{(\Delta\beta_\chi L)^2-(\kappa_\chi L)^2}\ \zeta} + a_2^+ e^{i\sqrt{(\Delta\beta_\chi L)^2-(\kappa_\chi L)^2}\ \zeta}\right), \tag{2.108a}$$

$$b^-(\zeta) = e^{-i\Delta\beta_\chi L\zeta}\left(b_1^- e^{-i\sqrt{(\Delta\beta_\chi L)^2-(\kappa_\chi L)^2}\ \zeta} + b_2^- e^{i\sqrt{(\Delta\beta_\chi L)^2-(\kappa_\chi L)^2}\ \zeta}\right), \tag{2.108b}$$

where each a_n^+ and b_n^- are complex values which can be found by imposing boundary conditions on the structure. The electric-field expressions for the contra-directional coupler are

$$a^+(\zeta) = \frac{-2B_1}{\kappa_{\chi ab} L e^{-i\eta L}}\left(\Delta\beta_\chi L \sinh(i\eta L(\zeta-1)) + \eta L \cosh(i\eta L(\zeta-1))\right), \tag{2.109a}$$

$$b^-(\zeta) = \frac{2B_1}{e^{-i\eta L}} \sinh(i\eta L(\zeta-1)), \tag{2.109b}$$

where

$$\eta L = \sqrt{(\Delta\beta_\chi L)^2 - (\kappa_\chi L)^2}. \tag{2.110}$$

The derivation method to arrive at the electric-field expressions is fully detailed in Section 2.8 below.

Power, Transmittivity, and Reflectivity Expressions

The power expressions are determined as the magnitude squared of the field expressions and are given as:

$$P_a^+(\zeta) = P_0 \frac{\left|\Delta\beta_\chi L \sinh\left(i\eta L(\zeta-1)\right) + \eta L \cosh\left(i\eta L(\zeta-1)\right)\right|^2}{\left|\Delta\beta_\chi L \sinh\left(-i\eta L\right) + \eta L \cosh\left(-i\eta L\right)\right|^2}, \tag{2.111a}$$

$$P_b^-(\zeta) = P_0 \frac{|\kappa_{\chi ab} L|^2 \left|\sinh\left(i\eta L(\zeta-1)\right)\right|^2}{\left|\Delta\beta_\chi L \sinh\left(-i\eta L\right) + \eta L \cosh\left(-i\eta L\right)\right|^2}. \tag{2.111b}$$

The transmittivity of a structure is defined as the ratio of an output power to an input power and shows the wavenumber response of the structure. For the contra-directional coupler, the input is taken as $P_a^+(\zeta=0)$, the contra-directional output is given by $P_b^-(\zeta=0)$, and co-directional out power as $P_a^+(\zeta=1)$ giving rise to the two transmittivity expressions

$$T_{contra} = \frac{P_b^-(\zeta=0)}{P_a^+(\zeta=0)} = \\ \frac{\left|\kappa_{\chi ab} L\right|^2 \left|\sinh\left(-i\sqrt{(\Delta\beta_\chi L)^2-(\kappa_\chi L)^2}\right)\right|^2}{\left|\Delta\beta_\chi L \sinh\left(-i\sqrt{(\Delta\beta_\chi L)^2-(\kappa_\chi L)^2}\right) + \sqrt{(\Delta\beta_\chi L)^2-(\kappa_\chi L)^2}\cosh\left(-i\sqrt{(\Delta\beta_\chi L)^2-(\kappa_\chi L)^2}\right)\right|^2}, \tag{2.112a}$$

$$T_{co} = \frac{P_a^+(\zeta=1)}{P_a^+(\zeta=0)} = \\ \frac{\left|\sqrt{(\Delta\beta_\chi L)^2-(\kappa_\chi L)^2}\right|^2}{\left|\Delta\beta_\chi L \sinh\left(-i\sqrt{(\Delta\beta_\chi L)^2-(\kappa_\chi L)^2}\right) + \sqrt{(\Delta\beta_\chi L)^2-(\kappa_\chi L)^2}\cosh\left(-i\sqrt{(\Delta\beta_\chi L)^2-(\kappa_\chi L)^2}\right)\right|^2}. \tag{2.112b}$$

2.7.2 Behavior

Plotting both transmittivity responses as over waveguide detuning $\Delta\beta_a L$ for a constant coupling $\kappa_a L$ results in the transmittivity spectrums shown in Fig. 2.8. A band of signal

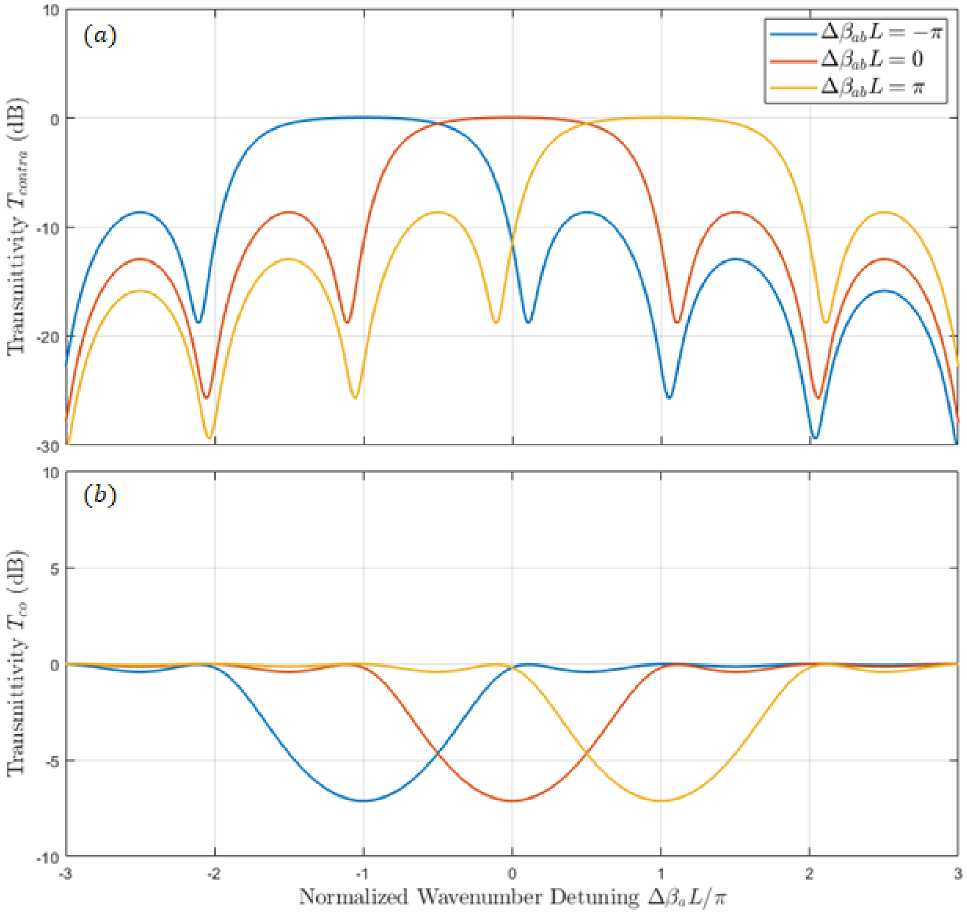

Figure 2.8 The transmittivity responses of a contra-directional coupler for three values of waveguide wavenumber detuning $\Delta\beta_{ab}L$. (a) The contra-directional transmittivity T_{contra} response shows a band of the optical power input at the A waveguide at $\zeta = 0$ coupled and output on the B waveguide also at $\zeta = 0$. (b) The photonic bandgap is clearly seen in the co-directional transmittivity response T_{co} centered at the normalized wavenumber detuning $\Delta\beta_a L = \Delta\beta_{ab}L = -\pi, 0, \pi$. For all parts $\kappa_\chi L = 1.47$.

presented at the input of waveguide A at $\zeta = 0$ is contra-directionally coupled to waveguide B and output at position $\zeta = 0$ as seen in Fig. 2.8(a). This exchange-Bragg coupling occurs between waveguides even when evanescent coupling is *not* present. Though the two coupling processes may co-exist, evanescent coupling is completely independent of exchange-Bragg coupling and one is not required for the other to function.

For a given wavenumber detuning $\Delta\beta_a L$, the photonic bandgap location is set by the waveguide wavenumber detuning $\Delta\beta_{ab}L$. The coupled-mode equations for the contra-directional coupler are functions of $\Delta\beta_\chi L = (\beta_a L + \beta_b L)/2 - \beta_\Lambda$ and therefore shift as

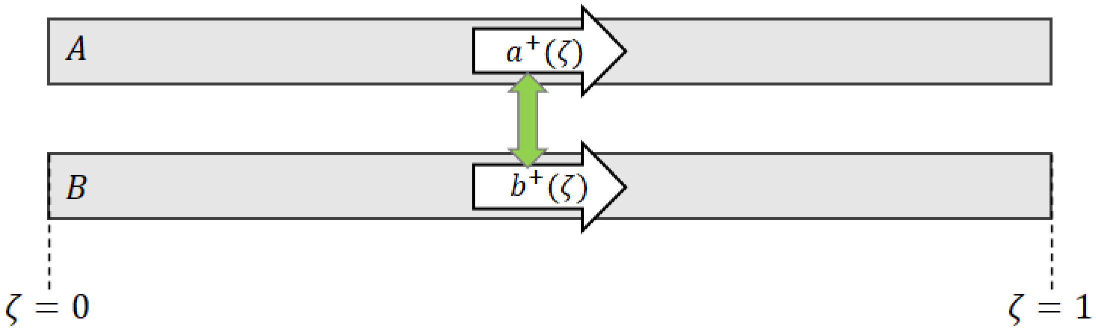

Figure 2.9 A directional coupler of length L demonstrating evanescent coupling (symbolically represented by the green arrow) between a forward-traveling mode a^+ in the A waveguide to a forward-traveling mode b^+ in the B waveguide. The symmetric coupling process of backwards-traveling modes is not shown.

$\Delta\beta_{ab}L$ changes. The PGBs are shown to shift for three different waveguide wavenumber detuning values in Fig. 2.8(b). For the grating-reflector, the center of the PBG is always located at $\Delta\beta_a L = 0$ as its CMEs are functions of $\Delta\beta_a L = \beta_a L - \beta_\Lambda$ which is completely independent of $\beta_b L$.

Structures which manifest both direct-Bragg and exchange-Bragg coupling may position their associated PBGs relative to one another through changes in the structures waveguide wavenumber detuning.

2.8 Directional Coupler & Evanescent Coupling

2.8.1 Theory

The Electric Field

The electric field expression for the directional coupler shown in Fig. 2.9 is written as:

$$\mathbf{E}(x,y,\zeta) = a^+(\zeta)\mathbf{e}_a(x,y)e^{+i\beta_p^a L\zeta} + b^+(\zeta)\mathbf{e}_b(x,y)e^{+i\beta_p^b L\zeta}, \tag{2.113}$$

where $(a,b)^+(\zeta)$ are the forward-propagating longitudinal field envelopes, $\mathbf{e}_{(a,b)}(x,y)$ are the normalized transverse mode profiles, $\beta_p^{(a,b)}$ are the wavenumbers for the forward-propagating modes associated with the A and B waveguides respectively and L is the length of the coupling region. Analysis for the forward propagating modes of the directional coupler will be provided in this section. The backwards-propagating solution for $a^{-}(\zeta)$ and $b^{-}(\zeta)$ is symmetric to what is presented here and will not shown.

As only the forward propagating modes are considered above, the substitutions of $\beta_a \equiv \beta_p^a$ and $\beta_b \equiv \beta_p^b$ result in the electric field expression:

$$\mathbf{E}(x,y,\zeta) = a^{+}(\zeta)\mathbf{e}_a(x,y)e^{+i\beta_a L\zeta} + b^{+}(\zeta)\mathbf{e}_b(x,y)e^{+i\beta_b L\zeta}, \tag{2.114}$$

where $\beta_a = 2\pi n_a/\lambda_0$ is the wavenumber of the A waveguide, n_a is the effective refractive index of the A waveguide, $\beta_b = 2\pi n_b/\lambda_0$ is the wavenumber of the B waveguide, n_b is the effective refractive index of the B waveguide, and λ_0 is the wavelength.

Coupled-Mode Equations

The directional coupler is a dual-waveguide photonic structure that transfers co-directional power across two coupled optical waveguides as shown in Fig. 2.9 [68], [73]. The amount of power transferred depends upon the distance between the two waveguides, the length of the structure, and the waveguide-wavenumber detuning.

The coupled-mode equations (CMEs) for the structure can be written from Eq. (2.17) as

$$\begin{aligned}
\frac{da^{+}}{d\zeta} &= i\,\mathrm{sgn}(\mathbb{S}_a^{+})\left(a^{+}(\zeta)\kappa_{aa}Le^{-i(\beta_p^a L-\beta_p^a L)\zeta} + b^{+}(\zeta)\kappa_{ba}Le^{-i(\beta_p^a L-\beta_p^b L)\zeta}\right),\\
\frac{db^{+}}{d\zeta} &= i\,\mathrm{sgn}(\mathbb{S}_b^{+})\left(a^{+}(\zeta)\kappa_{ab}Le^{-i(\beta_p^b L-\beta_p^a L)\zeta} + b^{+}(\zeta)\kappa_{bb}Le^{-i(\beta_p^b L-\beta_p^b L)\zeta}\right),
\end{aligned} \tag{2.115}$$

which reduces to:

$$\begin{aligned}\frac{da^+}{d\zeta} &= i\,\mathrm{sgn}(\mathbb{S}_a^+)\left(a^+(\zeta)\kappa_{aa}L + b^+(\zeta)\kappa_{ba}Le^{-i(\beta_p^a L-\beta_p^b L)\zeta}\right),\\ \frac{db^+}{d\zeta} &= i\,\mathrm{sgn}(\mathbb{S}_b^+)\left(a^+(\zeta)\kappa_{ab}Le^{-i(\beta_p^b L-\beta_p^a L)\zeta} + b^+(\zeta)\kappa_{bb}L\right),\end{aligned} \tag{2.116}$$

Making the substitutions of $\beta_a \equiv \beta_p^a$ and $\beta_b \equiv \beta_p^b$, where $\beta_a = 2\pi n_a/\lambda_0$ is the wavenumber of the A waveguide, n_a is the effective refractive index of the A waveguide, $\beta_b = 2\pi n_b/\lambda_0$ is the wavenumber of the B waveguide, n_b is the effective refractive index of the B waveguide, and λ_0 is the wavelength, yields:

$$\frac{da^+}{d\zeta} = i\,\mathrm{sgn}(\mathbb{S}_a^+)\left(a^+(\zeta)\kappa_{aa}L + b^+(\zeta)\kappa_{ba}Le^{-i2\Delta\beta_{ab}L\zeta}\right), \tag{2.117a}$$

$$\frac{db^+}{d\zeta} = i\,\mathrm{sgn}(\mathbb{S}_b^+)\left(a^+(\zeta)\kappa_{ab}Le^{i2\Delta\beta_{ab}L\zeta} + b^+(\zeta)\kappa_{bb}L\right). \tag{2.117b}$$

Resolving the sgn function and moving the sign associated with the direction of power flow to the left-hand side results in

$$\frac{da^+}{d\zeta} = i\left(a^+(\zeta)\kappa_{aa}L + b^+(\zeta)\kappa_{ba}Le^{-i2\Delta\beta_{ab}L\zeta}\right), \tag{2.118a}$$

$$\frac{db^+}{d\zeta} = i\left(a^+(\zeta)\kappa_{ab}Le^{i2\Delta\beta_{ab}L\zeta} + b^+(\zeta)\kappa_{bb}L\right). \tag{2.118b}$$

Evanescent Coupling Coefficients

The coupling coefficients for co-directional evanescent-coupling in the directional coupler CMEs consider the alternate waveguide as the region of perturbation. The change in relative permittivity $\Delta\bar{\varepsilon}$ is due to the sending-mode's waveguide perturbation as:

$$\Delta\bar{\varepsilon} = \bar{\varepsilon}_s - \bar{\varepsilon}_1, \tag{2.119}$$

where $\bar{\varepsilon}_s$ is the relative permittivity of the sending-mode's waveguide and $\bar{\varepsilon}_1$ is the relative permittivity of the cladding. These values are both constant across the transverse mode profile coordinates x and y and can be pulled out of the double integral. In general, $\bar{\varepsilon} = n^2$ where n is the refractive index, the coupling coefficient expression of Eq. (2.21) becomes:

$$\kappa_{sr} = \frac{\omega\varepsilon_0(n_s^2 - n_1^2)}{2} \int_{-\infty}^{\infty}\int_{-\infty}^{\infty} \mathbf{e}_s(x,y)\cdot\mathbf{e}_r^*(x,y)\;dy\;dx. \tag{2.120}$$

The evanescent-coupling coefficients for the directional coupler then become:

$$\kappa_{aa} = \frac{\omega\varepsilon_0(n_b^2 - n_1^2)}{2} \iint_B \mathbf{e}_a(x,y)\cdot\mathbf{e}_a^*(x,y)dx\;dy \tag{2.121a}$$

$$\kappa_{ab} = \frac{\omega\varepsilon_0(n_a^2 - n_1^2)}{2} \iint_A \mathbf{e}_a(x,y)\cdot\mathbf{e}_b^*(x,y)dx\;dy \tag{2.121b}$$

$$\kappa_{ba} = \frac{\omega\varepsilon_0(n_b^2 - n_1^2)}{2} \iint_B \mathbf{e}_b(x,y)\cdot\mathbf{e}_a^*(x,y)dx\;dy, \tag{2.121c}$$

$$\kappa_{bb} = \frac{\omega\varepsilon_0(n_a^2 - n_1^2)}{2} \iint_A \mathbf{e}_b(x,y)\cdot\mathbf{e}_b^*(x,y)dx\;dy, \tag{2.121d}$$

where $n_{(a,b)}$ is the constant material refractive index of the respective waveguide, n_1 is the refractive index of the cladding, ω is the angular frequency, ε_0 is the permittivity of free space, A is the region bounded by the A waveguide, and B is the region bounded by the B waveguide.

The coupling coefficients κ_{aa} and κ_{bb} are each determined by an overlap integral of a *single* mode over a region of integration bounded by the *adjacent* waveguide. In this region, only the *tail* of dot product $\mathbf{e}_{(a,b)}\cdot\mathbf{e}_{(a,b)}^* = |\mathbf{e}_{(a,b)}|^2$ contributes to the integral, which is assumed small such that $\kappa_{aa} = 0$ and $\kappa_{bb} = 0$.

The coupling coefficients $\kappa_{ab} = \kappa_{ba}^*$ occurs exactly when $n_a = n_b$ and $A = B$ or if there is a balance between an unmatched n_a and n_b and an unmatched $\iint_a$ and $\iint_B$.

Solution Using an Eigenvalue Approach

The coupled-mode equations of Eq. 2.118, assuming $\kappa_{aa}L = 0$ and $\kappa_{bb}L = 0$, become:

$$\frac{da^+}{d\zeta} = ib^+(\zeta)\kappa_{ba}Le^{-i2\Delta\beta_{ab}L\zeta}, \tag{2.122a}$$

$$\frac{db^+}{d\zeta} = ia^+(\zeta)\kappa_{ab}Le^{i2\Delta\beta_{ab}L\zeta}, \tag{2.122b}$$

which may be expressed in a rotated frame by substituting the envelope expressions from Eq. (2.20), rewritten here as

$$a^+(\zeta) = \hat{a}^+(\zeta)e^{-i\Delta\beta_{ab}L\zeta}, \tag{2.123a}$$

$$b^+(\zeta) = \hat{b}^+(\zeta)e^{+i\Delta\beta_{ab}L\zeta}. \tag{2.123b}$$

Performing this substitution and simplifying results in differential equations in the rotating frame as

$$\frac{d\hat{a}^+}{d\zeta} = i\Delta\beta_{ab}L\hat{a}^+ + i\kappa_{ba}L\hat{b}^+, \tag{2.124a}$$

$$\frac{d\hat{b}^+}{dz\zeta} = -i\Delta\beta_{ab}L\hat{b}^+ + i\kappa_{ab}L\hat{a}^+. \tag{2.124b}$$

The CMEs of Eq. (2.124) have been written in a linear form and can be expressed in matrix notation as

$$\frac{d}{dz}\vec{s} = \mathbb{A}\vec{s}, \tag{2.125}$$

where

$$\vec{s} = \begin{bmatrix} \hat{a}^+ \\ \hat{a}^- \end{bmatrix}, \tag{2.126}$$

and

$$\mathbb{A} = \begin{bmatrix} i\Delta\beta_{ab}L & i\kappa_{ba}L \\ i\kappa_{ab}L & -i\Delta\beta_{ab}L \end{bmatrix}, \tag{2.127}$$

where the explicit function of ζ has been dropped for notational simplicity.

Solutions to Eq. (2.125) can be found using an eigenvalue approach and takes the general form:

$$\vec{s}_n = \vec{v}_n e^{q_n \zeta} \quad \text{where} \quad n \in \{1,2\}, \tag{2.128}$$

$\vec{v}_n = [v_{n1},\ v_{n2}]^\dagger$ is an eigenvector, q_n is an eigenvalue, n takes on integer values up to the rank of the matrix $\mathbb{A}$, and † is the matrix transpose operator.

Eigenvalues are scalar values such that

$$\mathbb{A}\vec{s} = q\vec{s}, \tag{2.129a}$$

$$\mathbb{A}\vec{s} - q\vec{s} = 0, \tag{2.129b}$$

$$(\mathbb{A} - Iq)\vec{s} = 0, \tag{2.129c}$$

where I is the identity matrix, here of dimension 2×2. Non-trivial solutions occur when the left hand matrix is singular

$$\det(\mathbb{A} - Iq) = 0. \tag{2.130}$$

The determinant for the 2×2 case shown above expands out as:

$$\det \begin{vmatrix} a_{11} - q & a_{12} \\ a_{21} & a_{22} - q \end{vmatrix} = 0, \tag{2.131}$$

where a_{nm} are the elements of $\mathbb{A}$ for $n,m \in (1,2)$. The determinant for the 2×2 matrix is straightforward to calculate as the difference between the products of cross elements:

$$\text{Step 1}: \quad (a_{11}-q)(a_{22}-q)-a_{21}a_{12}=0, \tag{2.132a}$$

$$\text{Step 2}: \quad a_{11}a_{22}-a_{11}q-a_{22}q+q^2-a_{21}a_{12}=0, \tag{2.132b}$$

$$\text{Step 3}: \quad q^2-(a_{11}+a_{22})q+(a_{11}a_{22}-a_{21}a_{12})=0. \tag{2.132c}$$

The expression in Eq. (2.132c) is called the characteristic equation whose roots provide the eigenvalues for the general solutions in Eq. (2.128). The two roots of a second-order characteristic equation are given by the quadratic formula as:

$$q_1=\frac{a_{11}+a_{22}}{2}+\tfrac{1}{2}\sqrt{(a_{11}+a_{22})^2-4(a_{11}a_{22}-a_{21}a_{12})}, \tag{2.133a}$$

$$q_2=\frac{a_{11}+a_{22}}{2}-\tfrac{1}{2}\sqrt{(a_{11}+a_{22})^2-4(a_{11}a_{22}-a_{21}a_{12})}, \tag{2.133b}$$

$$\tag{2.133c}$$

or

$$q_1=\frac{a_{11}+a_{22}}{2}+i\sqrt{(a_{11}a_{22}-a_{21}a_{12})-\left(\frac{a_{11}+a_{22}}{2}\right)^2}, \tag{2.134a}$$

$$q_2=\frac{a_{11}+a_{22}}{2}-i\sqrt{(a_{11}a_{22}-a_{21}a_{12})-\left(\frac{a_{11}+a_{22}}{2}\right)^2}. \tag{2.134b}$$

The eigenvalues for the directional-coupler case given by the matrix $\mathbb{A}$ in Eq. (**??**) become:

$$q_1=+i\sqrt{(\Delta\beta_{ab}L)^2+\kappa_{ab}L\kappa_{ba}L}, \tag{2.135a}$$

$$q_2=-i\sqrt{(\Delta\beta_{ab}L)^2+\kappa_{ab}L\kappa_{ba}L}. \tag{2.135b}$$

The product $\kappa_{ab}\kappa_{ba}$ is defined to be κ_e such that $\kappa_e L=\sqrt{\kappa_{ab}L\kappa_{ba}L}$; the eigenvalues for a directional coupler can be written as

$$q_1 = +i\sqrt{(\Delta\beta_{ab}L)^2 + (\kappa_e L)^2}, \tag{2.136a}$$

$$q_2 = -i\sqrt{(\Delta\beta_{ab}L)^2 + (\kappa_e L)^2}. \tag{2.136b}$$

Electric-Field Expressions

The general slow-moving rotated-frame envelope expression Eq. (2.128) can now be expanded for the directional coupler as:

$$\hat{a}^+(\zeta) = v_{11}e^{+i\sqrt{(\Delta\beta_{ab}L)^2+(\kappa_e L)^2}\ \zeta} + v_{12}e^{-i\sqrt{(\Delta\beta_{ab}L)^2+(\kappa_e L)^2}\ \zeta}, \tag{2.137a}$$

$$\hat{b}^+(\zeta) = v_{21}e^{+i\sqrt{(\Delta\beta_{ab}L)^2+(\kappa_e L)^2}\ \zeta} + v_{22}e^{-i\sqrt{(\Delta\beta_{ab}L)^2+(\kappa_e L)^2}\ \zeta}, \tag{2.137b}$$

where v_{nm} are the unknown elements of the two eigenvectors which can be found by imposing boundary conditions on the structure. If power is injected only into waveguide A at $\zeta = 0$ then the boundary condition is

$$\hat{b}^+(0) = 0, \tag{2.138}$$

which, by using Eq. (2.137b), shows that $v_{21} = -v_{12}$. After manipulation and reduction, the slow-moving rotated-frame envelope field expression for $b^+(\zeta)$ becomes

$$\hat{b}^+(\zeta) = 2v_{12}\sinh\left(i\sqrt{(\Delta\beta_{ab}L)^2 + (\kappa_e L)^2}\ \zeta\right). \tag{2.139}$$

Substituting the above $b^{+}(\zeta)$ expression back into the directional coupler CME given in Eq. (2.124b) provides the slow-moving rotated-frame envelope field expression for $\hat{a}^{+}(\zeta)$ as

$$\begin{aligned}\hat{a}^{+}(\zeta) = \frac{2v_{12}}{\kappa_e L}\Bigg(&\Delta\beta_{ab}L\sinh\left(i\sqrt{(\Delta\beta_{ab}L)^2+(\kappa_{ab}L)^2}\,\zeta\right)\cdots \\ &+\sqrt{(\Delta\beta_{ab}L)^2+(\kappa_e L)^2}\cosh\left(i\sqrt{(\Delta\beta_{ab}L)^2+(\kappa_e L)^2}\,\zeta\right)\Bigg)\end{aligned} \tag{2.140}$$

To return to the slow-moving envelope field-expressions from the rotated frame, Eq. (2.123) is used resulting in expressions for $a^{+}(\zeta)$ and $b^{+}(\zeta)$.

Power Expressions

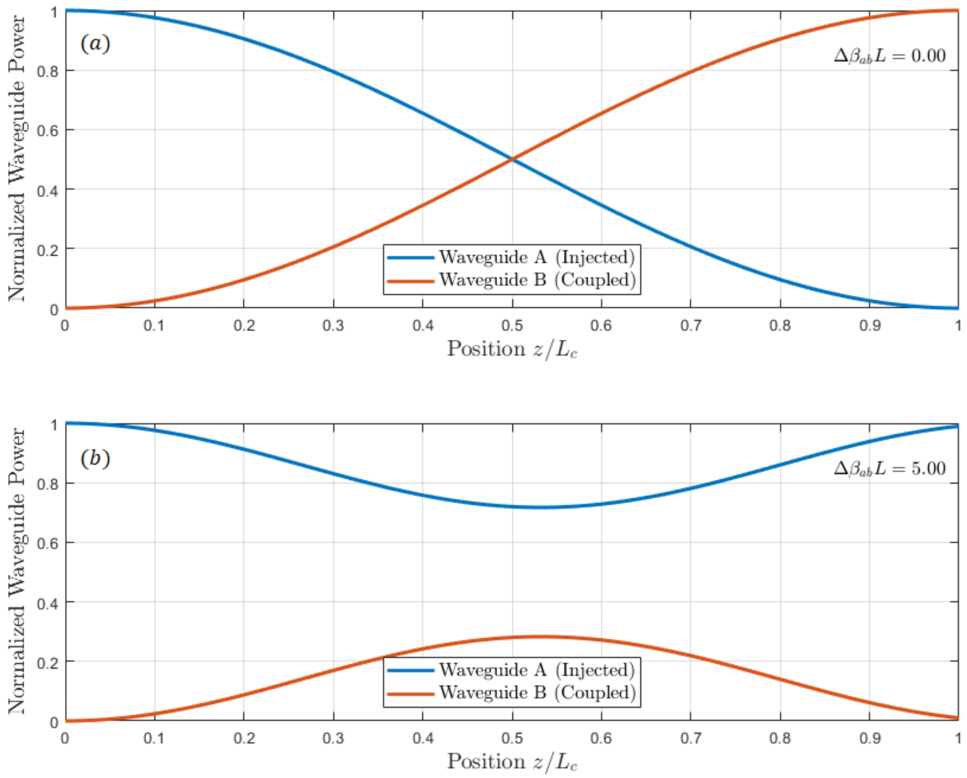

Figure 2.10 A directional coupler transfers power between two evanescently coupled optical waveguides. (a) When the directional coupler is synchronous, defined as the waveguide wavenumber detuning $\Delta\beta_{ab} = 0$, complete power transfer occurs across the two waveguides. This transfer happens at the coupling length L_c. (b) As the waveguide wavenumber detuning increases, that is the structure becomes asynchronous, power transfer efficiency rapidly declines. $\kappa_e L = 1.47$ for both subfigures.

The power in a waveguide is the magnitude squared of the field [68]:

$$P_a(\zeta) = |a^+(\zeta)|^2 = |\hat{a}^+(\zeta)|^2, \tag{2.141a}$$

$$P_b(\zeta) = |b^+(\zeta)|^2 = |\hat{b}^+(\zeta)|^2. \tag{2.141b}$$

Recall, for this example, power was injected in waveguide A at $\zeta = 0$. If the injected power is $P_a(\zeta = 0) = P_0$ then:

$$P_0 = P_a(\zeta = 0) = |\hat{a}^+(0)|^2 = \left|\frac{2v_{12}}{\kappa_e L}\right|^2 \left((\Delta\beta_{ab}L)^2 + (\kappa_{ab}L)^2\right). \tag{2.142}$$

The value is v_{12} can be found in terms of the input power P_0 which falls out due to normalization.

2.8.2 Behavior

The longitudinal power profile for both waveguides of the directional coupler when $\beta_a L = \beta_b L$ is shown in Fig. 2.10(a). Under this condition $\Delta\beta_{ab}L = 0$ and the directional coupler is considered synchronous, providing full transfer of power across the two waveguides at a coupling length L_c. Detuning the two waveguides such that $\beta_a L \neq \beta_b L$ results in a shift in the peak power transfer location and a reduced power transfer efficiency as seen in Fig. 2.10(b).

The magnitude of the waveguide-wavenumber detuning $\Delta\beta_{ab}L$ establishes the efficiency of the power transfer between the two waveguides of the directional coupler and quickly falls off as the waveguide-wavenumber detuning varies from zero as seen in Fig. 2.11 [68]. The total power transfer across waveguides is therefore a function of both the coupling coefficient and the waveguide-wavenumber detuning.

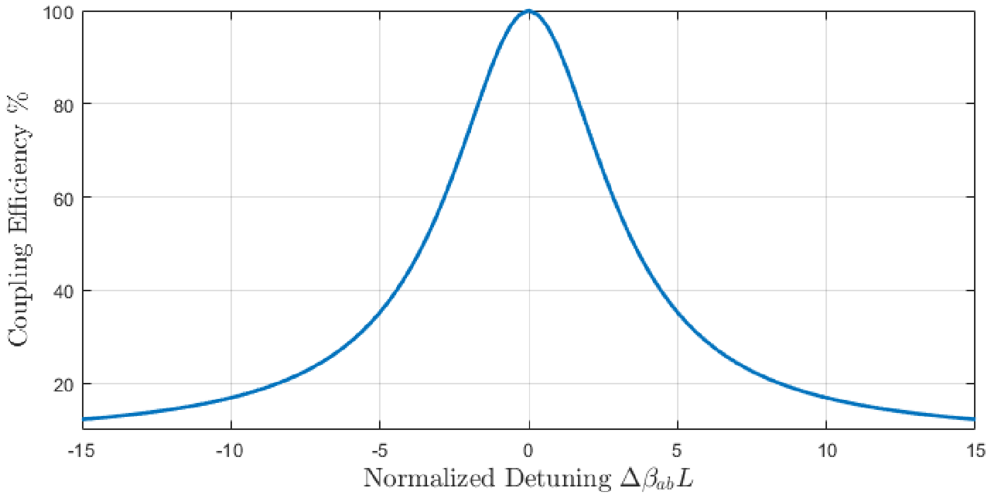

Figure 2.11 The maximum power transfer efficiency of a directional coupler peaks when the waveguides are matched in wavenumber and quickly falls off as the magnitude of waveguide wavenumber detuning $\Delta\beta_{ab}L$ increases. Maximum power transfer in this plot assumes the structure is long enough to support at least one full evanescent-coupling cycle. This length is called the coupling length L_c for the synchronous case.

2.9 Conclusion

The basic language of coupled-mode theory has been developed and the coupled-mode equations for the grating reflector, the uniform-grating DFB laser, the contra-directional coupler, and the directional coupler presented. Two methods of generating electric-field expressions, the eigenvalue approach and the ansatz approach, were presented in detail. Furthermore, closed-form parameterized waveguide power and transmittivity expressions were generated for each structure.

The transmittivity expression were used to isolate the lasing thresholds for the uniform-grating distributed feedback laser which was shown to result in a degenerate lasing mode spectrum. Single-mode lasing behavior was achieved by introducing a $\lambda/4$-phase shift element in the diffraction grating. Single-mode behavior was characterized by the quantity of gain margin, capturing the difference in threshold gain between the fundamental and secondary lasing modes of the structure, and longitudinal power profile flatness, capturing the expected impact of spatial-hole burning on above-threshold lasing performance.

The methods presented here leveraged in this dissertation on single-mode distributed feedback lasing in coupled dissimilar photonic waveguides.

3. Single-Mode DFB Lasing using Photonic-Bandgap Alignment: Theory

3.1 Introduction

This chapter presents a novel single-mode lasing mechanism which seeks to avoid the diffraction grating's $\lambda/4$-phase shift and its exacerbated nonlinear phase-shift problem. This is accomplished by introducing a passive waveguide placed in proximity to a uniform diffraction grating that is itself in proximity to an active waveguide, as depicted in Fig. 3.1(a). Due to the presence of the diffraction grating, the proposed structure supports direct-Bragg coupling within the modes of each waveguide as well as exchange-Bragg coupling between the modes of both waveguides [65]. Through proper selection of waveguide-wavenumber detuning, the exchange-Bragg PBG can be aligned to suppress the degenerate mode associated with the direct-Bragg PBG of the active waveguide, resulting in single-mode lasing.

Each of the three Bragg-coupling processes produces an associated PBG. Waveguide A contains the active region for lasing, and therefore direct-Bragg coupling within A is expected to exhibit strong, degenerate resonances on either side of its PBG. These degenerate modes are suppresed by positioning the exchange-Bragg PBG$_\chi$ and the waveguide B direct-

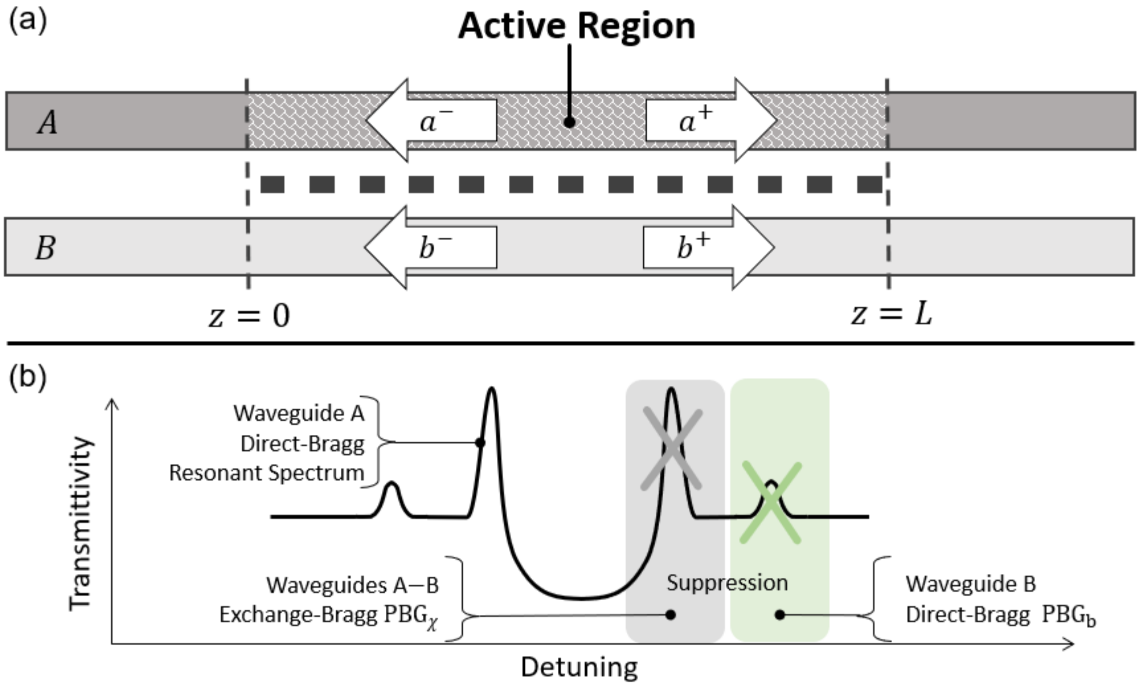

Figure 3.1 Single-mode DFB lasing structure & mechanism. (a) Structure: a uniform diffraction grating & active waveguide A, both of length L, plus a passive waveguide B. (b) Mechanism: the exchange-Bragg photonic bandgap PBG$_\chi$ and direct-Bragg photonic bandgap PBG$_b$ suppress degenerate lasing modes belonging to direct-Bragg coupling in active waveguide A.

Bragg PBG$_b$, as shown in Fig. 3.1(b).

The required dual waveguide geometry and waveguide wavenumber detuning of our proposed structure may be satisfied by integrated-photonic or silicon-photonic circuit process designs. A DFB laser seeking to take advantage of exchange-Bragg coupling to provide both optical feedback and power coupling across an active and passive waveguide pair was shown to be compatible with a III-V laser stack and silicon-on-insulator (SOI) process, however, no mathematical model was presented to capture the underlying physics of the structure and a $\lambda/4$-phase shift was again required to achieve its single-mode lasing behavior [6], [7].

Previous analytical modeling works that include exchange-Bragg coupling primarily focus on *passive* devices such as couplers [59], [60], [74], narrow-band reflectors [61], filters [63], and optical add-drop multiplexers [65]. To date, no active-passive dual-waveguide single-mode laser, which includes evanescent, direct-Bragg, and exchange-Bragg coupling, has been mathematically modeled and parameterized closed-form solutions provided. New & unexplored analytic solutions for the 2-waveguide DFB structure having direct- and exchange-Bragg coupling are herein developed allowing for the study of these key characteristics.

Coupled-mode equations (CMEs) that include gain and the associated nonlinearity of the active region are introduced for the novel single-mode lasing structure. Solutions to these CMEs will allow for the study of key at-threshold lasing characteristics and behaviors. The first portion of this chapter will assume evanescent coupling between waveguides is weak and can be disregarded in order to simplify the presented CMEs and the associated solution process. Neglecting evanescent coupling in the presence of exchange-Bragg coupling assumes that the opposite transverse modes do not overlap significantly each opposing waveguide, but do overlap significantly within the diffraction grating. Furthermore, the structures required detuning of waveguide wavenumbers is assumed to be sufficiently large to reduce the efficiency of evanescent coupling to a negligible level as discussed in Section 2.8. A new solution process will be presented which provides for electric-fields, longitudinal power profiles, and transmittivity for the three-coupled structure.

Once a baseline set of CMEs and the associated closed-form solutions are developed for the structure without evancesent coupling, evanescent coupling is then introduced and new closed-form analytic solutions are derived to capture the complete coupling model of the proposed four-coupled structure. Closed-form solutions can theoretically be provided for a coupled-mode system up to and *including* the fourth-order; quintic (fifth-order) equations and greater do not have closed-form roots using traditional algebraic methods [75]. It is with this full model that the effects of exchange-Bragg coupling strength and evanescent coupling strength will be explored in Chapter 4.

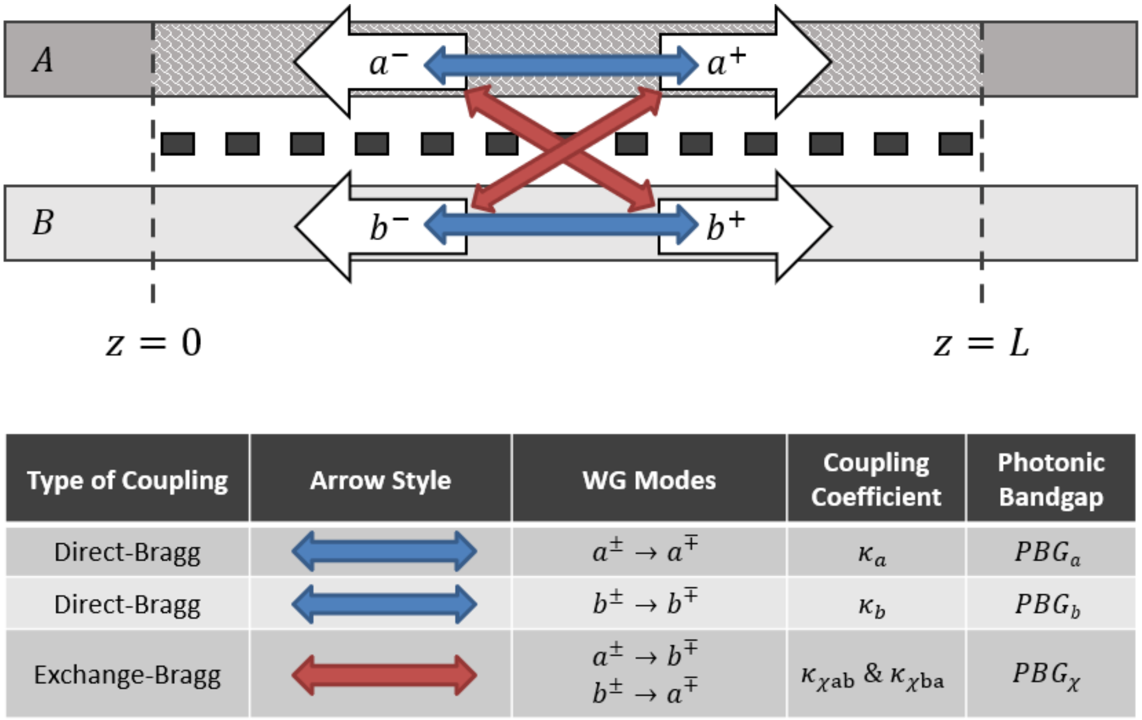

Type of Coupling	Arrow Style	WG Modes	Coupling Coefficient	Photonic Bandgap
Direct-Bragg	⟷	$a^\pm \to a^\mp$	κ_a	PBG_a
Direct-Bragg	⟷	$b^\pm \to b^\mp$	κ_b	PBG_b
Exchange-Bragg	⟷	$a^\pm \to b^\mp$ $b^\pm \to a^\mp$	$\kappa_{\chi\text{ab}}$ & $\kappa_{\chi\text{ba}}$	PBG_χ

Figure 3.2 Single-mode DFB lasing structure and coupling processes. Two direct-Bragg coupling processes transfer power between modes of the same waveguide where the exchange-Bragg coupling processes transfer power across counter-directional modes in opposite waveguides. The Bragg coupling processed have the associated coupling coefficients and photonic bandgaps as shown in the table. The modes for which power transfer occurs under each coupling process is specified in “WG Modes”.

3.2 Coupled-Mode Equations without Evanescent Coupling

The electric fields for the A and B waveguides of the structure shown in Fig. 3.2(a) are given by:

$$\mathbf{E}_A(x,y,z,t) = \left(a^+(z)e^{i\tilde{\beta}^a_p z} + a^-(z)e^{i\tilde{\beta}^a_{-p} z}\right)\mathbf{e}_a(x,y)e^{-i\omega t}, \tag{3.1a}$$

$$\mathbf{E}_B(x,y,z,t) = \left(b^+(z)e^{i\tilde{\beta}^b_p z} + b^-(z)e^{i\tilde{\beta}^b_{-p} z}\right)\mathbf{e}_b(x,y)e^{-i\omega t}, \tag{3.1b}$$

where $a^\pm(z)$ and $b^\pm(z)$ are the longitudinally varying amplitudes in either waveguide for the forward ($+$) and backward ($-$) propagating fields, $\tilde{\beta}^a_p = \beta^a_p - ig(1-i\alpha_H)/2 + i\alpha_a/2$ and

$\tilde{\beta}_p^b = \beta_p^b + i\alpha_b/2$ are the associated complex-valued wavenumbers of the unperturbed modes, $\beta_{\pm p}^a$ are the forward- and backward-propagating modes of associated with the A waveguide, $\beta_{\pm p}^b$ are the forward- and backward-propagating modes of associated with the B waveguide, g is the modal gain coefficient of the active region, $\alpha_{_H}$ is the semiconductor nonlinearity of the active region made of semiconductor, α_a and α_b are the loss coefficients of either waveguide, and ω is the angular frequency. Using $\beta_a = \beta_p^a = -\beta_{-p}^a$ and $\beta_b = \beta_p^b = -\beta_{-p}^b$ gives:

$$\mathbf{E}_A(x,y,z,t) = \left(a^+(z)e^{i\tilde{\beta}_a z} + a^-(z)e^{-i\tilde{\beta}_a z}\right)\mathbf{e}_a(x,y)e^{-i\omega t}, \tag{3.2a}$$

$$\mathbf{E}_B(x,y,z,t) = \left(b^+(z)e^{i\tilde{\beta}_b z} + b^-(z)e^{-i\tilde{\beta}_b z}\right)\mathbf{e}_b(x,y)e^{-i\omega t}, \tag{3.2b}$$

where $\tilde{\beta}_a = \beta_a - ig(1-i\alpha_{_H})/2 + i\alpha_a/2$, $\tilde{\beta}_b = \beta_b + i\alpha_b/2$, $\beta_a = 2\pi n_a/\lambda_0$ is the wavenumber of the A waveguide, n_a is the effective refractive index of the A waveguide, $\beta_b = 2\pi n_b/\lambda_0$ is the wavenumber of the B waveguide, n_b is the effective refractive index of the B waveguide, and λ_0 is the wavelength.

The quantities $\mathbf{e}_a(x,y)$ and $\mathbf{e}_b(x,y)$ are the unperturbed mode profiles for each waveguide in isolation. It is assumed that the unperturbed modes match the actual mode profiles and are approximately orthogonal. These approximations have allowed for insightful modeling of *passive* structures having direct- and exchange-Bragg coupling [65].

Under these approximations, and using the techniques detailed in Section 2.5 and Section 2.7 for the grating reflector and the contra-directional coupler, respectively, the coupled-mode equations (CMEs) governing direct- and exchange-Bragg coupling between the longitudinally varying field amplitudes can be written as:

$$\frac{da^+}{d\zeta} = i\,\mathrm{sgn}(\mathbb{S}_a^+)\left(\kappa_a L\, e^{-i2\Delta\tilde{\beta}_a L\zeta} a^- + \kappa_{\chi ba} L\, e^{-i2\Delta\tilde{\beta}_\chi L\zeta} b^-\right), \tag{3.3a}$$

$$\frac{db^+}{d\zeta} = i\,\mathrm{sgn}(\mathbb{S}_b^+)\left(\kappa_{\chi ab} L\, e^{-i2\Delta\tilde{\beta}_\chi L\zeta} a^- + \kappa_b L\, e^{-i2\Delta\tilde{\beta}_b L\zeta} b^-\right), \tag{3.3b}$$

$$\frac{da^-}{d\zeta} = i\,\mathrm{sgn}(\mathbb{S}_a^-)\left(\kappa_a L\, e^{i2\Delta\tilde{\beta}_a L\zeta} a^+ + \kappa_{\chi ba} L\, e^{i2\Delta\tilde{\beta}_\chi L\zeta} b^+\right), \tag{3.3c}$$

$$\frac{db^-}{d\zeta} = i\,\mathrm{sgn}(\mathbb{S}_b^-)\left(\kappa_{\chi ab} L\, e^{i2\Delta\tilde{\beta}_\chi L\zeta} a^+ + \kappa_b L\, e^{i2\Delta\tilde{\beta}_b L\zeta} b^+\right), \tag{3.3d}$$

where the sgn function returns the sign associated with the direction of modal power flow, $\zeta = z/L$ is the normalized longitudinal coordinate, κ_a and κ_b are the direct-Bragg coupling coefficients of waveguide A and B, and $\kappa_{\chi ab}$ and $\kappa_{\chi ba}$ are the exchange-Bragg coupling coefficients, as defined in Section 2.7, that accounts for counter propagating-mode coupling between the waveguides. Executing the sgn function and moving the resulting sign to the left-hand side provides:

$$\frac{da^+}{d\zeta} = i\kappa_a L\, e^{-i2\Delta\tilde{\beta}_a L\zeta} a^- + i\kappa_{\chi ba} L\, e^{-i2\Delta\tilde{\beta}_\chi L\zeta} b^-, \tag{3.4a}$$

$$\frac{db^+}{d\zeta} = i\kappa_{\chi ab} L\, e^{-i2\Delta\tilde{\beta}_\chi L\zeta} a^- + i\kappa_b L\, e^{-i2\Delta\tilde{\beta}_b L\zeta} b^-, \tag{3.4b}$$

$$-\frac{da^-}{d\zeta} = i\kappa_a L\, e^{i2\Delta\tilde{\beta}_a L\zeta} a^+ + i\kappa_{\chi ba} L\, e^{i2\Delta\tilde{\beta}_\chi L\zeta} b^+, \tag{3.4c}$$

$$-\frac{db^-}{d\zeta} = i\kappa_{\chi ab} L\, e^{i2\Delta\tilde{\beta}_\chi L\zeta} a^+ + i\kappa_b L\, e^{i2\Delta\tilde{\beta}_b L\zeta} b^+, \tag{3.4d}$$

The associated wavenumber detunings in terms of the Bragg wavenumber $\beta_\Lambda = \pi/\Lambda$ and grating period Λ are:

$$\Delta\tilde{\beta}_a = \tilde{\beta}_a - \beta_\Lambda = \Delta\beta_a - \alpha_H g/2 - i(g - \alpha_a)/2, \tag{3.5a}$$

$$\Delta\tilde{\beta}_b = \tilde{\beta}_b - \beta_\Lambda = \Delta\beta_a - 2\Delta\beta_{ab} + i\alpha_b/2, \tag{3.5b}$$

$$\Delta\tilde{\beta}_\chi = \frac{\tilde{\beta}_a + \tilde{\beta}_b}{2} - \beta_\Lambda = \Delta\beta_a - \Delta\beta_{ab} - \frac{\alpha_H g}{4} - i\frac{g - \alpha_s}{4}. \tag{3.5c}$$

where $\alpha_s = \alpha_a + \alpha_b$ and each complex-valued detuning quantity has been expressed in terms of 2 real-valued detuning quantities:

$$\Delta\beta_a = \beta_a - \beta_\Lambda, \qquad \Delta\beta_{ab} = (\beta_a - \beta_b)/2. \tag{3.6}$$

A gain coefficient g appears only for the optical mode in active waveguide A, ensuring that the PBG of direct-Bragg coupling in waveguide A exhibits the strongest resonances. Loss coefficients α_a and α_b appear for the A and B waveguides respectively. In semiconductor media, an increase in carrier density that drives an increase in gain also drives a descrease in the refractive index, accounted for in Eq. (3.5a) by Henry's alpha α_H [4].

Evanescent coupling coefficient κ_e terms are excluded from the CMEs because asynchronous operation (e.g., large $\Delta\beta_{ab}L$) produces a phase mismatch that weakens evanescent coupling efficiency [68], [73]. Evanescent coupling has been excluded for the study of passive asynchronous structures exhibiting a maximal power coupling of up to 9% [73]. Our structure meets a more severe coupling limit of 1% for $\kappa_e L \leq 0.23$, a reasonable assumption as the evanescent mode of either waveguide is assumed to extend only weakly into the opposite waveguide. This assumption is removed in Section 4.

3.3 Analytic Solution without Evanescent Coupling

3.3.1 Fourth-Order CME Solutions

General Solution

Analytic solutions of the CMEs in Eq. (3.4) are found by substituting the ansatz $(a,b)^{\pm} = (a_0,b_0)^{\pm}\exp(i\gamma^{\pm}_{(a,b)}L\zeta)$. Solving the resulting fourth-order characteristic polynomial drops the $(a_0,b_0)^{\pm}$ coefficients and yields the normalized quantities $\gamma^{\pm}_{(a,b)m}L$ which can then be used to form the general solution:

$$\begin{bmatrix} \hat{a}^+(\zeta) \\ \hat{b}^+(\zeta) \\ \hat{a}^-(\zeta) \\ \hat{b}^-(\zeta) \end{bmatrix} = \begin{bmatrix} a_1^+ & a_2^+ & a_3^+ & a_4^+ \\ b_1^+ & b_2^+ & b_3^+ & b_4^+ \\ a_1^- & a_2^- & a_3^- & a_4^- \\ b_1^- & b_2^- & b_3^- & b_4^- \end{bmatrix} \begin{bmatrix} e^{i\Theta_1\zeta} \\ e^{i\Theta_2\zeta} \\ e^{i\Theta_3\zeta} \\ e^{i\Theta_4\zeta} \end{bmatrix}, \tag{3.7}$$

where $(a,b)_m^\pm$ are complex-valued coefficients, $m \in \{1,2,3,4\}$, and $\gamma_{(a,b)m}^\pm L = \phi_{(a,b)}^\pm + \Theta_m$. The field amplitudes have been written in a rotated frame $(\hat{a},\hat{b})^\pm = (a,b)^\pm e^{-i\phi_{(a,b)}^\pm \zeta}$, where

$$\phi_a^\pm = \pm(-\Delta\tilde{\beta}_{ab}L - \Delta\tilde{\beta}_\chi L), \quad \phi_b^\pm = \pm(\Delta\tilde{\beta}_{ab}L - \Delta\tilde{\beta}_\chi L). \tag{3.8}$$

The complex-valued wavenumber detuning $\Delta\tilde{\beta}_{ab}$ is given by:

$$\Delta\tilde{\beta}_{ab} = \frac{\tilde{\beta}_a - \tilde{\beta}_b}{2} = \Delta\beta_{ab} - \frac{\alpha_H g}{4} - i\frac{(g - \alpha_a + \alpha_b)}{4}. \tag{3.9}$$

The quantities Θ_m are found from the four roots of the characteristic polynomial [76]:

$$\Theta_m = \frac{R_m + D_m(-1)^{(m-1)}}{2}, \tag{3.10a}$$

$$R_m = (-1)^{\tau_m}\sqrt{\frac{1}{4}p^2 - q + y_c}, \tag{3.10b}$$

$$D_m = \begin{cases} \sqrt{\frac{3}{4}p^2 - R_m^2 - 2q + \frac{(-1)^{\tau_m}}{4R_m}(4pq - 8u - p^3)} & R_m \neq 0 \\ \sqrt{\frac{3}{4}p^2 - 2q + 2(-1)^{\tau_m}\sqrt{y_c^2 - 4v}} & R_m = 0 \end{cases}, \tag{3.10c}$$

where $\tau_m = \lceil m/2 \rceil - 1$. The root y_c of the resolvent cubic is [76]:

$$y_c = \frac{\left(q - \xi^{(n-1)}\mathscr{E} - \frac{\Delta_0}{\xi^{(n-1)}\mathscr{E}}\right)}{3}, \tag{3.11a}$$

$$\mathscr{E} = \sqrt[3]{\frac{\Delta_1 + (-1)^\delta\sqrt{\Delta_1^2 - 4\Delta_0^3}}{2}}, \tag{3.11b}$$

where $n \in \{1,2,3\}$ is selected to provide the largest $|y_c|$, $\xi = -\frac{1}{2} + i\frac{\sqrt{3}}{2}$, and $\delta \in \{1,2\}$ is selected to provide the largest $|\mathscr{E}|$. The Δ_0 and Δ_1 quantities are defined as [76]:

$$\Delta_0 = q^2 - 3pu + 12v, \tag{3.12a}$$

$$\Delta_1 = -2q^3 - 27(u^2 + p^2 v) + 9pqu + 72qv. \tag{3.12b}$$

The quantities p, q, u, and v are the coefficients of the fourth-order characteristic polynomial, and can be written in terms of two detuning quantities $\Delta\tilde{\beta}_{ab}$ and $\Delta\tilde{\beta}_{\chi}$ as:

$$p = (4\Delta\tilde{\beta}_{ab} + 4\Delta\tilde{\beta}_{\chi})L, \tag{3.13a}$$

$$q = (4\Delta\tilde{\beta}_{ab}^2 + 12\Delta\tilde{\beta}_{ab}\Delta\tilde{\beta}_{\chi} + 4\Delta\tilde{\beta}_{\chi}^2 + \kappa_a^2 + \kappa_b^2 + 2\kappa_{\chi ab}\kappa_{\chi ba})L^2, \tag{3.13b}$$

$$\begin{aligned} u = (&8\Delta\tilde{\beta}_{ab}^2\Delta\tilde{\beta}_{\chi} + 8\Delta\tilde{\beta}_{ab}\Delta\tilde{\beta}_{\chi}^2 + 2\Delta\tilde{\beta}_{ab}\kappa_a^2 + 2\Delta\tilde{\beta}_{ab}\kappa_b^2 \\ &+ 4\Delta\tilde{\beta}_{ab}\kappa_{\chi ab}\kappa_{\chi ba} + 4\Delta\tilde{\beta}_{\chi}\kappa_{\chi ab}\kappa_{\chi ba} + 2\Delta\tilde{\beta}_{\chi}\kappa_a^2 + 2\Delta\tilde{\beta}_{\chi}\kappa_b^2)L^3, \end{aligned} \tag{3.13c}$$

$$\begin{aligned} v = (&4\Delta\tilde{\beta}_{ab}^2\kappa_{\chi ab}\kappa_{\chi ba} + 4\Delta\tilde{\beta}_{ab}\Delta\tilde{\beta}_{\chi}\kappa_a^2 + 4\Delta\tilde{\beta}_{ab}\Delta\tilde{\beta}_{\chi}\kappa_{\chi ab}\kappa_{\chi ba} \\ &+ \kappa_a^2\kappa_b^2 - 2\kappa_a\kappa_b\kappa_{\chi ab}\kappa_{\chi ba} + \kappa_{\chi ab}^2\kappa_{\chi ba}^2)L^4. \end{aligned} \tag{3.13d}$$

Recast Using Reflection Coefficients

The solutions in Eq. (3.7) can be recast in terms of reflection coefficients:

$$\begin{bmatrix} \hat{a}^+(\zeta) \\ \hat{b}^+(\zeta) \\ \hat{a}^-(\zeta) \\ \hat{b}^-(\zeta) \end{bmatrix} = \begin{bmatrix} 1 & r_{c2}^{b+} & r_{d3}^{a-} & r_{\chi 4}^{b-} \\ r_{c1}^{a+} & 1 & r_{\chi 3}^{a-} & r_{d4}^{b-} \\ r_{d1}^{a+} & r_{\chi 2}^{b+} & 1 & r_{c4}^{b-} \\ r_{\chi 1}^{a+} & r_{d2}^{b+} & r_{c3}^{a-} & 1 \end{bmatrix} \begin{bmatrix} a_1^+ e^{i\Theta_1\zeta} \\ b_2^+ e^{i\Theta_2\zeta} \\ a_3^- e^{i\Theta_3\zeta} \\ b_4^- e^{i\Theta_4\zeta} \end{bmatrix}, \tag{3.14}$$

where the reflection coefficients are given by:

$$r_{cm}^{ws} = \frac{(b,a)_m^{\pm}}{(a,b)_m^{\pm}} = \frac{\gamma_{wm}^{s}\gamma_{wm}^{\bar{s}}\kappa_{\bar{w}} + \kappa_w^2\kappa_{\bar{w}} - \kappa_w\kappa_{\chi w\bar{w}}\kappa_{\chi\bar{w}w}}{\gamma_{wm}^{\bar{s}}\gamma_{\bar{w}m}^{s}\kappa_{\chi\bar{w}w} - \kappa_w\kappa_{\bar{w}}\kappa_{\chi\bar{w}w} + \kappa_{\chi w\bar{w}}\kappa_{\chi\bar{w}w}^2}, \tag{3.15a}$$

$$r_{dm}^{ws} = \frac{(a,b)_m^{\mp}}{(a,b)_m^{\pm}} = \frac{\bar{s}\gamma_{wm}^{s}\kappa_{\bar{w}}\kappa_{\chi\bar{w}w} + \bar{s}\gamma_{\bar{w}m}^{s}\kappa_w\kappa_{\chi\bar{w}w}}{\gamma_{wm}^{\bar{s}}\gamma_{\bar{w}m}^{s}\kappa_{\chi\bar{w}w} - \kappa_w\kappa_{\bar{w}}\kappa_{\chi\bar{w}w} + \kappa_{\chi w\bar{w}}\kappa_{\chi\bar{w}w}^2}, \tag{3.15b}$$

$$r_{\chi m}^{ws} = \frac{(b,a)_m^{\mp}}{(a,b)_m^{\pm}} = \frac{s\gamma_{wm}^{s}\gamma_{wm}^{\bar{s}}\gamma_{\bar{w}m}^{\bar{s}} + s\gamma_{\bar{w}m}^{s}\kappa_w^2 + s\gamma_{wm}^{s}\kappa_{\chi w\bar{w}}\kappa_{\chi\bar{w}w}}{\gamma_{wm}^{\bar{s}}\gamma_{\bar{w}m}^{s}\kappa_{\chi\bar{w}w} - \kappa_w\kappa_{\bar{w}}\kappa_{\chi\bar{w}w} + \kappa_{\chi w\bar{w}}\kappa_{\chi\bar{w}w}^2}, \tag{3.15c}$$

Each reflection coefficient is a ratio of two $(a,b)_m^{\pm}$ coefficients and has been written in terms of a sign $s \in \{+,-\}$ and an amplitude identifier $w \in \{a_m, b_m\}$. The values of $\bar{s}$ and $\bar{w}$ in Eqs. (3.15) are the opposite element of the respective set.

3.3.2 Electric-Field Expressions

To study lasing, the analytic solutions provided by Eq. (3.14) are made to satisfy the boundary conditions $\hat{a}^-(1) = 0$, $\hat{b}^+(0) = 0$, and $\hat{b}^-(1) = 0$ under the assumption that facet reflections are negligible; $\hat{a}^+(0)$ is designated as the reference non-zero input field amplitude value. Applying these boundary conditions yields:

$$\begin{bmatrix} \hat{a}^+(0) \\ 0 \\ 0 \\ 0 \end{bmatrix} = \begin{bmatrix} 1 & r_{c2}^{b+} & r_{d3}^{a-} & r_{\chi 4}^{b-} \\ r_{c1}^{a+} & 1 & r_{\chi 3}^{a-} & r_{d4}^{b-} \\ r_{d1}^{a+}e^{i\Theta_1} & r_{\chi 2}^{b+}e^{i\Theta_2} & e^{i\Theta_3} & r_{c4}^{b-}e^{i\Theta_4} \\ r_{\chi 1}^{a+}e^{i\Theta_1} & r_{d2}^{b+}e^{i\Theta_2} & r_{c3}^{a-}e^{i\Theta_3} & e^{i\Theta_4} \end{bmatrix} \begin{bmatrix} a_1^+ \\ b_2^+ \\ a_3^- \\ b_4^- \end{bmatrix}. \tag{3.16}$$

Using the lower three expressions of equation above, the coefficients a_1^+, b_2^+, and a_3^- can be written in terms of b_4^-:

$$\begin{aligned} a_1^+ &= \Big(\Omega_{(2,3)}(r_{\chi 2}^{b+} r_{c3}^{a-} r_{d4}^{b-} - r_{d2}^{b+} r_{d4}^{b-}) + \Omega_{(2,4)}(r_{d2}^{b+} r_{\chi 3}^{a-} r_{c4}^{b-} - r_{\chi 2}^{b+} r_{\chi 3}^{a-}) \\ &\quad -\Omega_{(3,4)}(r_{c3}^{a-} r_{c4}^{b-} - 1)\Big)\,(-1)U^{-1} b_4^- = \Gamma_1 b_4^-, \end{aligned} \tag{3.17a}$$

$$\begin{aligned} b_2^+ &= \Big(\Omega_{(1,3)}(r_{d1}^{a+} r_{c3}^{a-} r_{d4}^{b-} - r_{\chi 1}^{a+} r_{d4}^{b-}) + \Omega_{(1,4)}(r_{\chi 1}^{a+} r_{\chi 3}^{a-} r_{c4}^{b-} - r_{d1}^{a+} r_{\chi 3}^{a-}) \\ &\quad -\Omega_{(3,4)}(r_{c1}^{a+} r_{c3}^{a-} r_{c4}^{b-} - r_{c1}^{a+})\Big)\,U^{-1} b_4^- = \Gamma_2 b_4^-, \end{aligned} \tag{3.17b}$$

$$\begin{aligned} a_3^- &= \Big(\Omega_{(1,2)}(r_{d1}^{a+} r_{d2}^{b+} r_{d4}^{b-} - r_{\chi 1}^{a+} r_{\chi 2}^{b+} r_{d4}^{b-}) + \Omega_{(1,4)}(r_{\chi 1}^{a+} r_{c4}^{b-} - r_{d1}^{a+}) \\ &\quad -\Omega_{(2,4)}(r_{c1}^{a+} r_{d2}^{b+} r_{c4}^{b-} - r_{c1}^{a+} r_{\chi 2}^{b+})\Big)\,(-1)U^{-1} b_4^- = \Gamma_3 b_4^-, \end{aligned} \tag{3.17c}$$

$$\begin{aligned} U &= \Omega_{(1,2)}(r_{d1}^{a+} r_{d2}^{b+} r_{\chi 3}^{a-} - r_{\chi 1}^{a+} r_{\chi 2}^{b+} r_{\chi 3}^{a-}) \\ &\quad + \Omega_{(2,3)}(r_{c1}^{a+} r_{\chi 2}^{b+} r_{c3}^{a-} - r_{c1}^{a+} r_{d2}^{b+}) - \Omega_{(1,3)}(r_{d1}^{a+} r_{c3}^{a-} - r_{\chi 1}^{a+}), \end{aligned} \tag{3.17d}$$

where $\Omega_{(a,b)} = e^{i(\Theta_a+\Theta_b)}$. Using the equations above, the analytic solutions in Eq. (3.14) can be simplified as:

$$\begin{bmatrix} \hat{a}^+(\zeta) \\ \hat{b}^+(\zeta) \\ \hat{a}^-(\zeta) \\ \hat{b}^-(\zeta) \end{bmatrix} = b_4^- \begin{bmatrix} 1 & r_{c2}^{b+} & r_{d3}^{a-} & r_{\chi 4}^{b-} \\ r_{c1}^{a+} & 1 & r_{\chi 3}^{a-} & r_{d4}^{b-} \\ r_{d1}^{a+} & r_{\chi 2}^{b+} & 1 & r_{c4}^{b-} \\ r_{\chi 1}^{a+} & r_{d2}^{b+} & r_{c3}^{a-} & 1 \end{bmatrix} \begin{bmatrix} \Gamma_1 e^{i\Theta_1\zeta} \\ \Gamma_2 e^{i\Theta_2\zeta} \\ \Gamma_3 e^{i\Theta_3\zeta} \\ e^{i\Theta_4\zeta} \end{bmatrix} = b_4^- \begin{bmatrix} \hat{f}_a^+(\zeta) \\ \hat{f}_b^+(\zeta) \\ \hat{f}_a^-(\zeta) \\ \hat{f}_b^-(\zeta) \end{bmatrix}. \tag{3.18}$$

3.3.3 Power, Transmittivity, and Reflectivity Expressions

The power of each unidirectional field along ζ is given by:

$$P_a^\pm(\zeta) = |a^\pm(\zeta)e^{\pm i\tilde{\beta}_a L\zeta}|^2 = |\hat{a}^\pm(\zeta)e^{i(\phi_a^\pm \pm \tilde{\beta}_a L)\zeta}|^2 = |\hat{a}^\pm(\zeta)|^2, \tag{3.19a}$$

$$P_b^\pm(\zeta) = |b^\pm(\zeta)e^{\pm i\tilde{\beta}_b L\zeta}|^2 = |\hat{b}^\pm(\zeta)e^{i(\phi_b^\pm \pm \tilde{\beta}_b L)\zeta}|^2 = |\hat{b}^\pm(\zeta)|^2. \tag{3.19b}$$

To eliminate the unknown coefficient b_4^-, each power expression is normalized by a reference power $P_a^+(1)$:

$$\mathbb{P}^{\pm}_{(a,b)}(\zeta) = \frac{P^{\pm}_{(a,b)}(\zeta)}{P_a^+(1)} = \frac{|b_4^-|^2|\hat{f}^{\pm}_{(a,b)}(\zeta)|^2}{|b_4^-|^2|\hat{f}_a^+(1)|^2} = \frac{|\hat{f}^{\pm}_{(a,b)}(\zeta)|^2}{|\hat{f}_a^+(1)|^2}. \tag{3.20}$$

The normalized longitudinal power in each waveguide is the sum of the associated counter-propagating powers [4], [5], [35] :

$$\mathbb{P}_A(\zeta) = \mathbb{P}_a^+(\zeta) + \mathbb{P}_a^-(\zeta) \quad \text{and} \quad \mathbb{P}_B(\zeta) = \mathbb{P}_b^+(\zeta) + \mathbb{P}_b^-(\zeta). \tag{3.21}$$

Lasing threshold and gain margin can be determined via the transmittivity or reflectivity through any pair of ports; the transmittivity T_a through waveguide A is given by:

$$T_a = \mathbb{P}_a^+(1)/\mathbb{P}_a^+(0) = |\hat{a}^+(1)|^2/|\hat{a}^+(0)|^2 = |\hat{f}_a^+(1)|^2/|\hat{f}_a^+(0)|^2. \tag{3.22}$$

3.4 Coupled-Mode Equations with Evanescent Coupling

Evanescent coupling, which may occur between the active and passive waveguides, is not necessary to form the photonic bandgaps that govern lasing behavior of the proposed structure. Although this kind of coupling may occur in principle, it was argued in the previous section that it can be neglected due to poor transverse-field overlap in either waveguide and due to the required asynchronous operation (i.e., wavenumber mismatch) [50]. This bound is realized for coupling values of $\kappa_e L \leq 0.25$ and $\Delta\beta_{ab}L \geq 5$. In general, evanescent coupling values which are greater than 0.25 should be accounted for when modeling lasing behaviors. In this section, the CMEs are extended to include evanescent coupling as shown in Fig. 3.3, and then execute a full closed-form solution derivation,

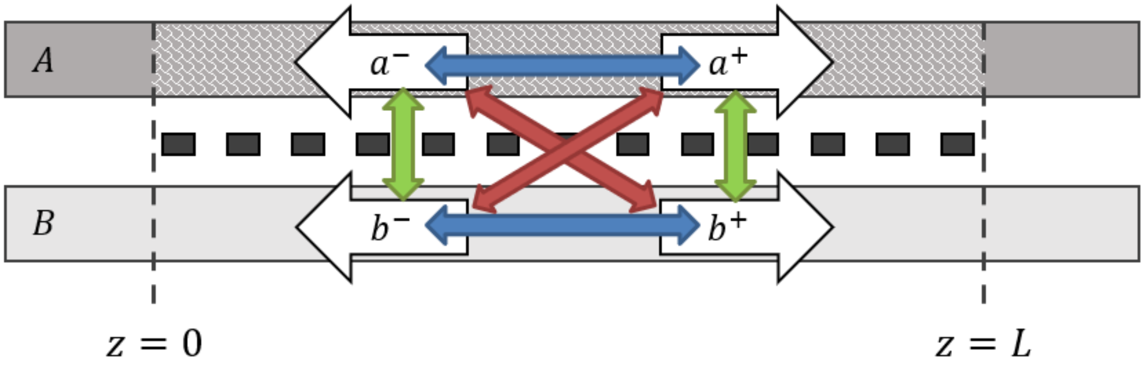

Type of Coupling	Arrow Style	WG Modes	Coupling Coefficient	Photonic Bandgap
Direct-Bragg	↔	$a^\pm \to a^\mp$	κ_a	PBG_a
Direct-Bragg	↔	$b^\pm \to b^\mp$	κ_b	PBG_b
Exchange-Bragg	↔	$a^\pm \to b^\mp$ $b^\pm \to a^\mp$	$\kappa_{\chi ab}$ & $\kappa_{\chi ba}$	PBG_χ
Evanescent	↔	$a^\pm \to b^\pm$ $b^\pm \to a^\pm$	κ_{ab} & κ_{ba}	None

Figure 3.3 The single-mode DFB lasing structure and coupling processes with evanescent coupling included. The Bragg based coupling processes remain unchanged but evanescent coupling is now included in the model shown by the green arrows. Evanescent coupling transfers power between co-diretional modes across waveguides and does not have an associated photonic bandgap.

ultimately, to ascertain its impact on lasing properties.

The electric fields E_A and E_B for light in the active waveguide A and passive waveguide B, respectively, are given by:

$$\mathbf{E}_A(x,y,z,t) = \left(a^+(z)e^{i\tilde{\beta}^a_p z} + a^-(z)e^{i\tilde{\beta}^a_{-p} z}\right)\mathbf{e}_a(x,y)e^{-i\omega t}, \tag{3.23a}$$

$$\mathbf{E}_B(x,y,z,t) = \left(b^+(z)e^{i\tilde{\beta}^b_p z} + b^-(z)e^{i\tilde{\beta}^b_{-p} z}\right)\mathbf{e}_b(x,y)e^{-i\omega t}, \tag{3.23b}$$

where $(a,b)^\pm$ are the forward (+) and backward (-) slowly varying amplitudes in either waveguide, $\tilde{\beta}^a_{\pm p}$ are the complex wavenumbers for the forward- and backwards-propagating modes for the A waveguide, and $\tilde{\beta}^b_{\pm p}$ are the complex wavenumbers for the forward- and backwards-propagating modes for the B waveguide, as defined in Eq. 3.2. The time dependence is expressed using the angular frequency $\omega = 2\pi c/\lambda$, where c is the speed of light in vacuum.

Making the substitutions $\beta_a \equiv \beta_p^a = -\beta_{-p}^a$ and $\beta_b \equiv \beta_p^b = -\beta_{-p}^b$ where $\beta_a = 2\pi n_a/\lambda_0$ is the wavenumber of the A waveguide, n_a is the effective refractive index of the A waveguide, $\beta_b = 2\pi n_b/\lambda_0$ is the wavenumber of the B waveguide, n_b is the effective refractive index of the B waveguide, and λ_0 is the wavelength, yields:

$$\mathbf{E}_A(x,y,z,t) = \left(a^+(z)e^{i\tilde{\beta}_a z} + a^-(z)e^{-i\tilde{\beta}_a z}\right)\mathbf{e}_a(x,y)e^{-i\omega t}, \tag{3.24a}$$

$$\mathbf{E}_B(x,y,z,t) = \left(b^+(z)e^{i\tilde{\beta}_b z} + b^-(z)e^{-i\tilde{\beta}_b z}\right)\mathbf{e}_b(x,y)e^{-i\omega t}, \tag{3.24b}$$

The transverse mode profiles $\mathbf{e}_a(x,y)$ and $\mathbf{e}_b(x,y)$ express the shape of the optical mode in waveguides A and B, respectively, over the transverse dimensions x and y. These mode profiles are the fundamental modes of either waveguide and their shapes are assumed to be unperturbed in the presence of the diffraction grating and opposite waveguide. Moreover, these structural perturbations are assumed not to erode the orthogonality of the mode profiles, an approximation that has historically been used to model physical systems and structures which include evanescent, direct-, and exchange-Bragg coupling [50], [65].

Using the techniques detailed in Section 2.5 for the grating reflector, Section 2.7 for the contra-directional coupler, and Section 2.8 for the directional coupler, the coupled-mode equations (CMEs) governing direct-Bragg, exchange-Bragg, and evanescent coupling processes between the four longitudinally varying field amplitudes $(a,b)^{\pm}$ can be written as:

$$\begin{aligned}\frac{da^{+}}{d\zeta} = i\,\mathrm{sgn}(\mathbb{S}_{a}^{+})\Big(&b^{+}\kappa_{ba}Le^{-i2\Delta\tilde{\beta}_{ab}L\zeta}+a^{-}\kappa_{a}Le^{-i2\Delta\tilde{\beta}_{a}L\zeta}\\ &+b^{-}\kappa_{\chi ba}Le^{-i2\Delta\tilde{\beta}_{\chi}L\zeta}\Big),\end{aligned} \tag{3.25a}$$

$$\begin{aligned}\frac{db^{+}}{d\zeta} = i\,\mathrm{sgn}(\mathbb{S}_{a}^{-})\Big(&a^{+}\kappa_{ab}Le^{i2\Delta\tilde{\beta}_{ab}L\zeta}+a^{-}\kappa_{\chi ab}Le^{-i2\Delta\tilde{\beta}_{\chi}L\zeta}\\ &+b^{-}\kappa_{b}Le^{-i2\Delta\tilde{\beta}_{b}L\zeta}\Big),\end{aligned} \tag{3.25b}$$

$$\begin{aligned}-\frac{da^{-}}{d\zeta} = i\,\mathrm{sgn}(\mathbb{S}_{b}^{+})\Big(&a^{+}\kappa_{a}Le^{i2\Delta\tilde{\beta}_{a}L\zeta}+b^{+}\kappa_{\chi ba}Le^{i2\Delta\tilde{\beta}_{\chi}L\zeta}\\ &+b^{-}\kappa_{ba}Le^{i2\Delta\tilde{\beta}_{ab}L\zeta}\Big),\end{aligned} \tag{3.25c}$$

$$\begin{aligned}-\frac{db^{-}}{d\zeta} = i\,\mathrm{sgn}(\mathbb{S}_{b}^{-})\Big(&a^{+}\kappa_{\chi ab}Le^{i2\Delta\tilde{\beta}_{\chi}L\zeta}+b^{+}\kappa_{b}Le^{i2\Delta\tilde{\beta}_{b}L\zeta}\\ &+a^{-}\kappa_{ab}Le^{-i2\Delta\tilde{\beta}_{ab}L\zeta}\Big),\end{aligned} \tag{3.25d}$$

where the *sgn* function returns the sign associated with the direction of modal power flow, L is the length of the coupling region and active region, and $\zeta = z/L$ is the normalized longitudinal position. Evaluating the sgn function and moving the resulting sign to the left-hand side results in:

$$\begin{aligned}\frac{da^{+}}{d\zeta} = {}&ib^{+}\kappa_{ba}Le^{-i2\Delta\tilde{\beta}_{ab}L\zeta}+ia^{-}\kappa_{a}Le^{-i2\Delta\tilde{\beta}_{a}L\zeta}\\ &+ib^{-}\kappa_{\chi ba}Le^{-i2\Delta\tilde{\beta}_{\chi}L\zeta},\end{aligned} \tag{3.26a}$$

$$\begin{aligned}\frac{db^{+}}{d\zeta} = {}&ia^{+}\kappa_{ab}Le^{i2\Delta\tilde{\beta}_{ab}L\zeta}+ia^{-}\kappa_{\chi ab}Le^{-i2\Delta\tilde{\beta}_{\chi}L\zeta}\\ &+ib^{-}\kappa_{b}Le^{-i2\Delta\tilde{\beta}_{b}L\zeta},\end{aligned} \tag{3.26b}$$

$$\begin{aligned}-\frac{da^{-}}{d\zeta} = {}&ia^{+}\kappa_{a}Le^{i2\Delta\tilde{\beta}_{a}L\zeta}+ib^{+}\kappa_{\chi ba}Le^{i2\Delta\tilde{\beta}_{\chi}L\zeta}\\ &+ib^{-}\kappa_{ba}Le^{i2\Delta\tilde{\beta}_{ab}L\zeta},\end{aligned} \tag{3.26c}$$

$$\begin{aligned}-\frac{db^{-}}{d\zeta} = {}&ia^{+}\kappa_{\chi ab}Le^{i2\Delta\tilde{\beta}_{\chi}L\zeta}+ib^{+}\kappa_{b}Le^{i2\Delta\tilde{\beta}_{b}L\zeta}\\ &+ia^{-}\kappa_{ab}Le^{-i2\Delta\tilde{\beta}_{ab}L\zeta},\end{aligned} \tag{3.26d}$$

Each term of each derivative function couples a slowly varying amplitude via a coupling coefficient and complex wavenumber detuning. The latter are defined as

$$\Delta\tilde{\beta}_a = \tilde{\beta}_a - \beta_\Lambda = \Delta\beta_a - \alpha_H g/2 - i(g-\alpha_a)/2, \tag{3.27a}$$

$$\Delta\tilde{\beta}_\chi = \frac{\tilde{\beta}_a + \tilde{\beta}_b}{2} - \beta_\Lambda = \Delta\beta_a - \Delta\beta_{ab} - \frac{\alpha_H g}{4} - i\frac{g-\alpha_s}{4} \tag{3.27b}$$

$$\Delta\tilde{\beta}_b = \tilde{\beta}_b - \beta_\Lambda = \Delta\beta_a - 2\Delta\beta_{ab} + i\alpha_b/2, \tag{3.27c}$$

where $\alpha_s = \alpha_a + \alpha_b$.

Using the complex-detuning definitions of Eq. (3.27), the interrelationships between the complex-detuning values is found as

$$\Delta\tilde{\beta}_a L + \Delta\tilde{\beta}_b L = 2\Delta\tilde{\beta}_\chi L, \tag{3.28}$$

In the CMEs, κ_a and κ_b are the coupling coefficients of direct-Bragg coupling within the A and B waveguides, respectively, $\kappa_{\chi ab}$ and $\kappa_{\chi ba}$ are the exchange-Bragg coupling coefficients for counter-directional coupling into and out of waveguide B, respectively, and κ_{ab} and κ_{ba} are the evanescent coupling coefficients for co-directional coupling into and out of waveguide B, respectively. In this work, the coupling coefficients are treated phenomenologicaly and do not calculate them from specific perturbation values & shapes with specific shapes of transverse mode profiles. Nonetheless, the equations for various coupling coefficients are instructive, and were provided in the sections above, showing that the coupling coefficients for evanescent coupling, direct-Bragg coupling, and exchange-Bragg coupling can all be different. This study assumes a specific range of values can be achieved.

3.5 Analytic Solution with Evanescent Coupling

3.5.1 Fourth-order CME Solutions

The Ansatz

To analytically solve the CMEs of Eq. (3.26), a set of viable slowly varying envelope solutions are assumed to take the form:

$$(a,b)^{\pm}(\zeta) = (a,b)_0^{\pm} e^{i\gamma_{(a,b)}^{\pm}\zeta}, \tag{3.29}$$

where $(a,b)_0^{\pm}$ are four unknown complex-valued coefficients and $\gamma_{(a,b)}^{\pm}$ are four unknown complex-valued quantities that reside in the ζ-dependent exponential function.

Complex-Exponent Relationships

Substituting the ansatz Eq. (3.29) into the CMEs of Eq. (3.26) generates four expressions:

$$\begin{aligned} \gamma_a^+ a_0^+ &= b_0^+ \kappa_{ba} L e^{-i(2\Delta\tilde{\beta}_{ab}L - \gamma_b^+ + \gamma_a^+)\zeta} \\ &\quad + a_0^- \kappa_a L e^{-i(2\Delta\tilde{\beta}_a L - \gamma_a^- + \gamma_a^+)\zeta} \\ &\quad + b_0^- \kappa_{\chi ba} L e^{-i(2\Delta\tilde{\beta}_\chi L - \gamma_b^- + \gamma_a^+)\zeta}, \end{aligned} \tag{3.30a}$$

$$\begin{aligned} \gamma_b^+ b_0^+ &= a_0^+ \kappa_{ab} L e^{i(2\Delta\tilde{\beta}_{ab}L + \gamma_a^+ - \gamma_b^+)\zeta} \\ &\quad + a_0^- \kappa_{\chi ab} L e^{-i(2\Delta\tilde{\beta}_\chi L - \gamma_a^- + \gamma_b^+)\zeta} \\ &\quad + b_0^- \kappa_b L e^{-i(2\Delta\tilde{\beta}_b L - \gamma_b^- + \gamma_b^+)\zeta}, \end{aligned} \tag{3.30b}$$

$$\begin{aligned} -\gamma_a^- a_0^- &= a_0^+ \kappa_a L e^{i(2\Delta\tilde{\beta}_a L + \gamma_a^+ - \gamma_a^-)\zeta} \\ &\quad + b_0^+ \kappa_{\chi ba} L e^{i(2\Delta\tilde{\beta}_\chi L + \gamma_b^+ - \gamma_a^-)\zeta} \\ &\quad + b_0^- \kappa_{ba} L e^{i(2\Delta\tilde{\beta}_{ab} L + \gamma_b^- - \gamma_a^-)\zeta}, \end{aligned} \tag{3.30c}$$

$$\begin{aligned} -\gamma_b^- b_0^- &= a_0^+ \kappa_{\chi ab} L e^{i(2\Delta\tilde{\beta}_\chi L + \gamma_a^+ - \gamma_b^-)\zeta} \\ &\quad + b_0^+ \kappa_b L e^{i(2\Delta\tilde{\beta}_b L + \gamma_b^+ - \gamma_b^-)\zeta} \\ &\quad + a_0^- \kappa_{ab} L e^{-i(2\Delta\tilde{\beta}_{ab} L - \gamma_a^- + \gamma_b^-)\zeta}. \end{aligned} \tag{3.30d}$$

Since the left-hand side of each expression is independent of ζ, each of the six unique complex-exponents of Eq. (3.30) must equal zero for the expressions to be valid for all values of ζ:

$$2\Delta\tilde{\beta}_{ab}L + \gamma_a^+ - \gamma_b^+ = 0, \qquad 2\Delta\tilde{\beta}_{ab}L + \gamma_b^- - \gamma_a^- = 0, \tag{3.31a}$$

$$2\Delta\tilde{\beta}_a L + \gamma_a^+ - \gamma_a^- = 0, \qquad 2\Delta\tilde{\beta}_b L + \gamma_b^+ - \gamma_b^- = 0, \tag{3.31b}$$

$$2\Delta\tilde{\beta}_\chi L + \gamma_a^+ - \gamma_b^- = 0, \qquad 2\Delta\tilde{\beta}_\chi L + \gamma_b^+ - \gamma_a^- = 0. \tag{3.31c}$$

This same logic has been used for sets of two CMEs [68], and is extended for the provided set of four CMEs.

Linear Frame Expression

The conditions above eliminate the exponential functions of Eq. (3.30), resulting in four ζ-independent algebraic equations:

$$\gamma_a^+ a_0^+ = \kappa_{ba} L b_0^+ + \kappa_a L a_0^- + \kappa_{\chi ba} L b_0^-, \tag{3.32a}$$

$$\gamma_b^+ b_0^+ = \kappa_{ab} L a_0^+ + \kappa_{\chi ab} L a_0^- + \kappa_b L b_0^-, \tag{3.32b}$$

$$-\gamma_a^- a_0^- = \kappa_a L a_0^+ + \kappa_{\chi ba} L b_0^+ + \kappa_{ba} L b_0^-, \tag{3.32c}$$

$$-\gamma_b^- b_0^- = \kappa_{\chi ab} L a_0^+ + \kappa_b L b_0^+ + \kappa_{ab} L a_0^-. \tag{3.32d}$$

The Matrix Expression

By combining the expressions in Eq. (3.31) with the interrelations among complex-valued detuning quantities in Eq. (3.28), it is found that any of the four complex-valued exponents γ can then expressed in terms of another exponent. Thus, solving for γ_a^+ yields all other exponents via:

$$\gamma_b^+ = \gamma_a^+ + 2\Delta\tilde{\beta}_{ab} L, \tag{3.33a}$$

$$\gamma_a^- = \gamma_a^+ + 2\Delta\tilde{\beta}_{ab} L + 2\Delta\tilde{\beta}_{\chi} L, \tag{3.33b}$$

$$\gamma_b^- = \gamma_a^+ + 2\Delta\tilde{\beta}_{\chi} L. \tag{3.33c}$$

Using the complex-exponent relationships of Eq. (3.33), the four linear equations in Eq. (3.32) can be written in one complex exponent γ_a^+ as

$$\mathbb{A}\vec{x} = 0 \tag{3.34}$$

where,

$$\mathbb{A} = \begin{bmatrix} \gamma_a^+ & -\kappa_{ba}L & -\kappa_a L & -\kappa_{\chi ba}L \\ -\kappa_{ab}L & \gamma_a^+ + 2\Delta\tilde{\beta}_{ab}L & -\kappa_{\chi ab}L & -\kappa_b L \\ \kappa_a L & \kappa_{\chi ba}L & \gamma_a^+ + 2\Delta\tilde{\beta}_\chi L + 2\Delta\tilde{\beta}_{ab}L & \kappa_{ba}L \\ \kappa_{\chi ab}L & \kappa_b L & \kappa_{ab}L & \gamma_a^+ + 2\Delta\tilde{\beta}_\chi L \end{bmatrix}, \tag{3.35}$$

and

$$\vec{x} = \begin{bmatrix} a_0^+ & b_0^+ & a_0^- & b_0^- \end{bmatrix}^\dagger, \tag{3.36}$$

where † represents the transpose.

Characteristic Polynomial

Non-trivial solutions to the matrix expression $\mathbb{A}\vec{x} = 0$ occur if and only if $\det\mathbb{A} = 0$. This was performed for a set of 2 CMEs [68], and has been extended here to the novel set of 4 CMEs. For this case, the determinant expressions forms fourth-order characteristic polynomial in γ_a^+ as:

$$\det\mathbb{A} \equiv \gamma_a^{+4} + p\gamma_a^{+3} + q\gamma_a^{+2} + u\gamma_a^+ + v = 0, \tag{3.37}$$

where the polynomial coefficients are found, after some work, to be

$$p = (4\Delta\tilde{\beta}_{ab} + 4\Delta\tilde{\beta}_{\chi})\, L, \tag{3.38a}$$

$$\begin{aligned} q = (&4\Delta\tilde{\beta}_{ab}^2 + 12\Delta\tilde{\beta}_{ab}\Delta\tilde{\beta}_{\chi} + 4\Delta\tilde{\beta}_{\chi}^2 \\ &- 2\kappa_{ab}\kappa_{ba} + \kappa_a^2 + \kappa_b^2 + 2\kappa_{\chi ab}\kappa_{\chi ba})\, L^2, \end{aligned} \tag{3.38b}$$

$$\begin{aligned} u = (&8\Delta\tilde{\beta}_{ab}^2\Delta\tilde{\beta}_{\chi} + 8\Delta\tilde{\beta}_{ab}\Delta\tilde{\beta}_{\chi}^2 + 2\Delta\tilde{\beta}_{ab}\kappa_a^2 + 2\Delta\tilde{\beta}_{ab}\kappa_b^2 \\ &+ 4\Delta\tilde{\beta}_{ab}\kappa_{\chi ab}\kappa_{\chi ba} - 4\Delta\tilde{\beta}_{ab}\kappa_{ab}\kappa_{ba} - 4\Delta\tilde{\beta}_{\chi}\kappa_{ab}\kappa_{ba} + 4\Delta\tilde{\beta}_{\chi}\kappa_{\chi ab}\kappa_{\chi ba} \\ &+ 2\Delta\tilde{\beta}_{\chi}\kappa_a^2 + 2\Delta\tilde{\beta}_{\chi}\kappa_b^2)\, L^3, \end{aligned} \tag{3.38c}$$

$$\begin{aligned} v = (&4\Delta\tilde{\beta}_{ab}^2\kappa_{\chi ab}\kappa_{\chi ba} - 4\Delta\tilde{\beta}_{ab}\Delta\tilde{\beta}_{\chi}\kappa_{ab}\kappa_{ba} + 4\Delta\tilde{\beta}_{ab}\Delta\tilde{\beta}_{\chi}\kappa_a^2 \\ &+ 4\Delta\tilde{\beta}_{ab}\Delta\tilde{\beta}_{\chi}\kappa_{\chi ab}\kappa_{\chi ba} - 2\Delta\tilde{\beta}_{ab}\kappa_{ab}\kappa_a\kappa_{\chi ba} + 2\Delta\tilde{\beta}_{ab}\kappa_{ab}\kappa_b\kappa_{\chi ba} \\ &- 2\Delta\tilde{\beta}_{ab}\kappa_{ba}\kappa_a\kappa_{\chi ab} + 2\Delta\tilde{\beta}_{ab}\kappa_{ba}\kappa_b\kappa_{\chi ab} - 4\Delta\tilde{\beta}_{\chi}^2\kappa_{ab}\kappa_{ba} \\ &+ 2\Delta\tilde{\beta}_{\chi}\kappa_{ab}\kappa_a\kappa_{\chi ba} + 2\Delta\tilde{\beta}_{\chi}\kappa_{ab}\kappa_b\kappa_{\chi ba} + 2\Delta\tilde{\beta}_{\chi}\kappa_{ba}\kappa_a\kappa_{\chi ab} \\ &+ 2\Delta\tilde{\beta}_{\chi}\kappa_{ba}\kappa_b\kappa_{\chi ab} + \kappa_{ab}^2\kappa_{ba}^2 - \kappa_{ab}^2\kappa_{\chi ba}^2 - 2\kappa_{ab}\kappa_{ba}\kappa_a\kappa_b \\ &- \kappa_{ba}^2\kappa_{\chi ab}^2 + \kappa_a^2\kappa_b^2 - 2\kappa_a\kappa_b\kappa_{\chi ab}\kappa_{\chi ba} + \kappa_{\chi ab}^2\kappa_{\chi ba}^2)\, L^4. \end{aligned} \tag{3.38d}$$

Root Solutions

Root expressions for polynomials of degree four or less can be found in closed-form [76]. The fourth-order polynomial in Eq. (3.37) has four roots $\gamma_{am}^{+}\ \forall\, m \in \{1,2,3,4\}$. The polynomial root expressions are of the form

$$\gamma_{am}^{+} = \phi_a^{+} + \Theta_m \tag{3.39}$$

where ϕ_a^{+} is common across each of the four roots defining a complex axis of symmetry or rotation. The unique component Θ_m of each of the four roots establishes its complex position relative to the common rotation ϕ_a^{+}. Roots of this form allow complex-exponent solutions to be developed in a rotated frame by factoring out ϕ_a^{+} and solving for solutions in

Θ_m.

Calculating the roots in the required form provides the common rotation ϕ_a^+ as

$$\phi_a^+ = -\left(\Delta\tilde{\beta}_{ab}L + \Delta\tilde{\beta}_{\chi}L\right) \tag{3.40}$$

with the four unique values of Θ_m in terms of the characteristic-polynomial coefficients p, q, u, and v being:

$$\Theta_m = \frac{R_m + D_m(-1)^{(m-1)}}{2}, \tag{3.41a}$$

$$R_m = (-1)^{\tau_m}\sqrt{\frac{1}{4}p^2 - q + y_c}, \tag{3.41b}$$

$$D_m = \begin{cases} \sqrt{\frac{3}{4}p^2 - R^2 - 2q + \frac{(-1)^{\tau_m}}{4R_m}\left(4pq - 8u - p^3\right)} & R_m \neq 0 \\ \sqrt{\frac{3}{4}p^2 - 2q + 2(-1)^{\tau_m}\sqrt{y_c^2 - 4v}} & R_m = 0 \end{cases}, \tag{3.41c}$$

where $\tau_m = \lceil m/2 \rceil - 1$. The value y_c is the root of the resolvent cubic:

$$y_c = -\frac{1}{3}\left(-q + \xi^{(n-1)}\mathscr{E} + \frac{\Delta_0}{\xi^{(n-1)}\mathscr{E}}\right), \tag{3.42a}$$

$$\mathscr{E} = \sqrt[3]{\frac{\Delta_1 + (-1)^{\delta}\sqrt{\Delta_1^2 - 4\Delta_0^3}}{2}}, \tag{3.42b}$$

where $n \in \{1,2,3\}$ is selected to provide the largest $|y_c|$. The value $\xi = e^{i3\pi/2}$ is the first complex cube-root of 1. The exponent $\delta \in \{1,2\}$ is selected so as to provide the largest $|\mathscr{E}|$. Each of the quantities Δ_0 and Δ_1 are defined using Cardano's method as:

$$\Delta_0 = q^2 - 3pu + 12v, \tag{3.43a}$$

$$\Delta_1 = -2q^3 - 27(u^2 + p^2 v) + 9pqu + 72qv. \tag{3.43b}$$

The Complex Exponents

Each of the 12 remaining members of the 16-member set of complex exponents $\gamma^{\pm}_{(a,b)_m}$ can be found using the complex-exponent relationships in Eq. (3.33). The complex-exponent relationship offsets the common rotation of γ^{+}_{a} to a new rotation while leaving the unique root component Θ_m unchanged. The complete set of 16 complex exponents are

$$\gamma^{+}_{am} = -\left(\Delta\tilde{\beta}_{ab}L + \Delta\tilde{\beta}_{\chi}L\right) + \Theta_m = \phi^{+}_{a} + \Theta_m, \tag{3.44a}$$

$$\gamma^{+}_{bm} = \left(\Delta\tilde{\beta}_{ab}L - \Delta\tilde{\beta}_{\chi}L\right) + \Theta_m = \phi^{+}_{b} + \Theta_m, \tag{3.44b}$$

$$\gamma^{-}_{am} = \left(\Delta\tilde{\beta}_{ab}L + \Delta\tilde{\beta}_{\chi}L\right) + \Theta_m = \phi^{-}_{a} + \Theta_m, \tag{3.44c}$$

$$\gamma^{-}_{bm} = -\left(\Delta\tilde{\beta}_{ab}L - \Delta\tilde{\beta}_{\chi}L\right) + \Theta_m = \phi^{-}_{b} + \Theta_m. \tag{3.44d}$$

The complex exponents generate four groups of four unique kernels in each group $\exp(i\gamma^{\pm}_{(a,b)_m}\zeta)$ where each groups kernels satisfy the associated slowly varyting envelop $(a,b)^{\pm}(\zeta)$ as a solution to the CMEs in Eqs. (3.26).

General Solution

Generalized solutions for each slow-moving envelope $(a,b)^{\pm}(\zeta)$, are comprised of the weighted sum of the four kernels in the associated group. These general solutions are

$$a^{+}(\zeta) = a^{+}_{1}e^{i\gamma^{+}_{a1}\zeta} + a^{+}_{2}e^{i\gamma^{+}_{a2}\zeta} + a^{+}_{3}e^{i\gamma^{+}_{a3}\zeta} + a^{+}_{4}e^{i\gamma^{+}_{a4}\zeta}, \tag{3.45a}$$

$$b^{+}(\zeta) = b^{+}_{1}e^{i\gamma^{+}_{b1}\zeta} + b^{+}_{2}e^{i\gamma^{+}_{b2}\zeta} + b^{+}_{3}e^{i\gamma^{+}_{b3}\zeta} + b^{+}_{4}e^{i\gamma^{+}_{b4}\zeta}, \tag{3.45b}$$

$$a^{-}(\zeta) = a^{-}_{1}e^{i\gamma^{-}_{a1}\zeta} + a^{-}_{2}e^{i\gamma^{-}_{a2}\zeta} + a^{-}_{3}e^{i\gamma^{-}_{a3}\zeta} + a^{-}_{4}e^{i\gamma^{-}_{a4}\zeta}, \tag{3.45c}$$

$$b^{-}(\zeta) = b^{-}_{1}e^{i\gamma^{-}_{b1}\zeta} + b^{-}_{2}e^{i\gamma^{-}_{b2}\zeta} + b^{-}_{3}e^{i\gamma^{-}_{b3}\zeta} + b^{-}_{4}e^{i\gamma^{-}_{b4}\zeta}. \tag{3.45d}$$

Rotated Frames

The general solutions can be written in a rotated frame by dividing both sides of Eq. (3.45) by its associated common rotation exponent $\exp(i\phi^{\pm}_{(a,b)})$. The result is a set of general solutions in a rotated frame, shown here in matrix notation:

$$\begin{bmatrix} \hat{a}^{+}(\zeta) \\ \hat{b}^{+}(\zeta) \\ \hat{a}^{-}(\zeta) \\ \hat{b}^{-}(\zeta) \end{bmatrix} = \begin{bmatrix} a_1^{+} & a_2^{+} & a_3^{+} & a_4^{+} \\ b_1^{+} & b_2^{+} & b_3^{+} & b_4^{+} \\ a_1^{-} & a_2^{-} & a_3^{-} & a_4^{-} \\ b_1^{-} & b_2^{-} & b_3^{-} & b_4^{-} \end{bmatrix} \begin{bmatrix} e^{i\Theta_1\zeta} \\ e^{i\Theta_2\zeta} \\ e^{i\Theta_3\zeta} \\ e^{i\Theta_4\zeta} \end{bmatrix}, \tag{3.46}$$

where $(a,b)^{\pm}_{m}$ are unknown coefficients to be determined using boundary conditions and

$$(\hat{a},\hat{b})^{\pm} = (a,b)^{\pm} e^{-i\phi^{\pm}_{(a,b)}\zeta}. \tag{3.47}$$

The *longitudinal component* of the electric-field expressions in Eqs. (3.24) can be rewritten in the rotated frames as:

$$\mathbf{E}_A(\zeta) = \hat{a}^{+}(\zeta)e^{i(\tilde{\beta}_a L+\phi_a^{+})\zeta} + \hat{a}^{-}(\zeta)e^{-i(\tilde{\beta}_a L-\phi_a^{-})\zeta}, \tag{3.48a}$$

$$\mathbf{E}_B(\zeta) = \hat{b}^{+}(\zeta)e^{i(\tilde{\beta}_b L+\phi_b^{+})\zeta} + \hat{b}^{-}(\zeta)e^{-i(\tilde{\beta}_b L-\phi_b^{-})\zeta}. \tag{3.48b}$$

Rotated CMEs

A new set of rotated-frame coupled-mode equations is found by passing the rotated frames in Eq. (3.47) through the original coupled-mode equations in Eqs. (3.26). The common-rotation of the rotated frame causes each of the exponent expressions of the original CMEs to drop out, leaving a set of four linear coupled-mode equations in the rotated frame:

$$\frac{d\hat{a}^+}{d\zeta} = -i\hat{a}^+\phi_a^+ + i\hat{b}^+\kappa_{ba}L + i\hat{a}^-\kappa_a L + i\hat{b}^-\kappa_{\chi ba}L, \tag{3.49a}$$

$$\frac{d\hat{b}^+}{d\zeta} = i\hat{a}^+\kappa_{ab}L - i\hat{b}^+\phi_b^+ + i\hat{a}^-\kappa_{\chi ab}L + i\hat{b}^-\kappa_b L, \tag{3.49b}$$

$$-\frac{d\hat{a}^-}{d\zeta} = i\hat{a}^+\kappa_a L + i\hat{b}^+\kappa_{\chi ba}L + i\hat{a}^-\phi_a^- + i\hat{b}^-\kappa_{ba}L, \tag{3.49c}$$

$$-\frac{d\hat{b}^-}{d\zeta} = i\hat{a}^+\kappa_{\chi ab}L + i\hat{b}^+\kappa_b L + i\hat{a}^-\kappa_{ab}L + i\hat{b}^-\phi_b^-. \tag{3.49d}$$

Reflection Coefficients

The general solutions in the rotated frame of Eq. (3.46) are applied to the rotated-frame CMEs of Eq. (3.49) producing four expressions with each expression written in terms of the four rotated-frame kernels $e^{i\Theta_m\zeta}$.

Collecting terms from like exponents generates sixteen linear expressions relating the sixteen unknown coefficients $(a,b)_m^\pm$ of the rotated-frame general solution to the known values of $\kappa_a L$, $\kappa_b L$, $\kappa_{\chi ab}L$, $\kappa_{\chi ba}L$, and $\gamma^\pm_{(a,b)m}$:

$$\gamma^+_{am}a^+_m = b^+_m\kappa_{ba}L + a^-_m\kappa_a L + b^-_m\kappa_{\chi ba}L, \tag{3.50a}$$

$$\gamma^+_{bm}b^+_m = a^+_m\kappa_{ab}L + a^-_m\kappa_{\chi ab}L + b^-_m\kappa_b L, \tag{3.50b}$$

$$-\gamma^-_{am}a^-_m = a^+_m\kappa_a L + b^+_m\kappa_{\chi ba}L + b^-_m\kappa_{ba}L, \tag{3.50c}$$

$$-\gamma^-_{bm}b^-_m = a^+_m\kappa_{\chi ab}L + b^+_m\kappa_b L + a^-_m\kappa_{ab}L. \tag{3.50d}$$

Creating four sets of four equations, each set in terms of an index m, allows for the solution of any coefficient w^s_m, where $w \in (a,b)$ and $s \in (+,-)$, in terms of a selected coefficient for that set. The selected coefficient for each set m is determined as the coefficient indexed by m in $\mathbb{C}_m \in \{a_1^+, b_2^+, a_3^-, b_4^-\}$, being the diagonal of Eq. (3.46). The reflection coefficients for a set of equations indexed by m are found as the ratio of each coefficient to the selected coefficient of the set:

$$r_{cm}^{ws} = \frac{\bar{w}_m^s}{w_m^s}, \quad r_{dm}^{ws} = \frac{w_m^{\bar{s}}}{w_m^s}, \quad r_{\chi m}^{ws} = \frac{\bar{w}_m^{\bar{s}}}{w_m^s}. \tag{3.51}$$

The values w and s are determined from the selected coefficient which appears in the denominator of every reflection coefficient. The quantities $\bar{w}$ and $\bar{s}$ are determined as the opposite set element identifier of the selected coefficient. For example, the first selected coefficient from $\mathbb{C}$ is a_1^+ implying $w = a, \bar{w} = b, s = +$, and $\bar{s} = -$.

To form these ratios only twelve of the sixteen expressions are required. This implies there are four equivalent forms for each of the twelve reflection coefficients r for a total of forty-eight unique expressions. Due to the equivalency of each form, the following set of twelve coefficients has been selected for this work, though any of the other three sets would produce identical results:

$$\begin{aligned} r_{cm}^{ws} = \big(&\gamma_{wm}^s \gamma_{wm}^{\bar{s}} \kappa_{\bar{w}} + \bar{s}\gamma_{wm}^s \kappa_{\bar{w}w} \kappa_{\chi w\bar{w}} + s\gamma_{wm}^{\bar{s}} \kappa_{w\bar{w}} \kappa_{\chi \bar{w}w} \\ &- \kappa_{\bar{w}w} \kappa_{w\bar{w}} \kappa_w + \kappa_w^2 \kappa_{\bar{w}} - \kappa_w \kappa_{\chi w\bar{w}} \kappa_{\chi \bar{w}w}\big) V^{-1}, \end{aligned} \tag{3.52a}$$

$$\begin{aligned} r_{dm}^{ws} = \big(&-\gamma_{wm}^s \gamma_{\bar{w}m}^s \kappa_{\bar{w}w} + \bar{s}\gamma_{wm}^s \kappa_{\bar{w}} \kappa_{\chi \bar{w}w} + \bar{s}\gamma_{\bar{w}m}^s \kappa_w \kappa_{\chi \bar{w}w} \\ &+ \kappa_{w\bar{w}} \kappa_{w\bar{w}}^2 - \kappa_{w\bar{w}} \kappa_{\chi \bar{w}w}^2 - \kappa_{\bar{w}w} \kappa_{\bar{w}} \kappa_w\Big) V^{-1}, \end{aligned} \tag{3.52b}$$

$$\begin{aligned} r_{\chi m}^{ws} = \big(&s\gamma_{wm}^s \gamma_{wm}^{\bar{s}} \gamma_{\bar{w}m}^{\bar{s}} + \bar{s}\gamma_{wm}^{\bar{s}} \kappa_{w\bar{w}} \kappa_{\bar{w}w} + s\gamma_{\bar{w}m}^s \kappa_w^2 \\ &+ s\gamma_{wm}^s \kappa_{\chi w\bar{w}} \kappa_{\chi \bar{w}w} + \kappa_{\bar{w}w} \kappa_w \kappa_{\chi w\bar{w}} + \kappa_{w\bar{w}} \kappa_w \kappa_{\chi \bar{w}w}\big) V^{-1}, \end{aligned} \tag{3.52c}$$

$$\begin{aligned} V = &\gamma_{wm}^{\bar{s}} \gamma_{\bar{w}m}^s \kappa_{\chi \bar{w}w} + s\gamma_{wm}^{\bar{s}} \kappa_{\bar{w}w} \kappa_w + \bar{s}\gamma_{\bar{w}m}^s \kappa_{\bar{w}w} \kappa_w \\ &- \kappa_{\bar{w}w}^2 \kappa_{\chi w\bar{w}} - \kappa_w \kappa_{\bar{w}} \kappa_{\chi \bar{w}w} + \kappa_{\chi w\bar{w}} \kappa_{\chi \bar{w}w}^2 \end{aligned} \tag{3.52d}$$

Using the reflection coefficients of Eqs. (3.52), the rotated-frame general solutions of

Eqs. (3.46) can be written in four unknowns as:

$$\begin{bmatrix} \hat{a}^+(\zeta) \\ \hat{b}^+(\zeta) \\ \hat{a}^-(\zeta) \\ \hat{b}^-(\zeta) \end{bmatrix} = \begin{bmatrix} 1 & r_{c2}^{b+} & r_{d3}^{a-} & r_{\chi 4}^{b-} \\ r_{c1}^{a+} & 1 & r_{\chi 3}^{a-} & r_{d4}^{b-} \\ r_{d1}^{a+} & r_{\chi 2}^{b+} & 1 & r_{c4}^{b-} \\ r_{\chi 1}^{a+} & r_{d2}^{b+} & r_{c3}^{a-} & 1 \end{bmatrix} \begin{bmatrix} a_1^+ e^{i\Theta_1 \zeta} \\ b_2^+ e^{i\Theta_2 \zeta} \\ a_3^- e^{i\Theta_3 \zeta} \\ b_4^- e^{i\Theta_4 \zeta} \end{bmatrix} . \tag{3.53}$$

Interrelations among a_1^+, b_2^+, a_3^-, and a_4^-

Interrelations among the constant coefficients a_1^+, b_2^+, a_3^-, and a_4^- are found by applying the boundary conditions that light is only injected into the $a_1^+(0)$, and thus $\hat{b}^+(0) = 0$, $\hat{a}^-(1) = 0$ and $\hat{b}^-(1) = 0$ where $\hat{a}^+(0)$. These boundary conditions assume that facet reflections are negligible. Substituting these boundary conditions into (3.53) yields

$$\begin{bmatrix} \hat{a}^+(0) \\ 0 \\ 0 \\ 0 \end{bmatrix} = \begin{bmatrix} 1 & r_{c2}^{b+} & r_{d3}^{a-} & r_{\chi 4}^{b-} \\ r_{c1}^{a+} & 1 & r_{\chi 3}^{a-} & r_{d4}^{b-} \\ r_{d1}^{a+} e^{i\Theta_1} & r_{\chi 2}^{b+} e^{i\Theta_2} & e^{i\Theta_3} & r_{c4}^{b-} e^{i\Theta_4} \\ r_{\chi 1}^{a+} e^{i\Theta_1} & r_{d2}^{b+} e^{i\Theta_2} & r_{c3}^{a-} e^{i\Theta_3} & e^{i\Theta_4} \end{bmatrix} \begin{bmatrix} a_1^+ \\ b_2^+ \\ a_3^- \\ b_4^- \end{bmatrix} , \tag{3.54}$$

where the rotated-frame kernels Θ_m, evaluated at their respective boundary points, have been pulled into the reflection coefficient matrix.

Non-zero values of $\hat{a}^+(0)$ allow for the study of the structures transmittivity behavior as it approaches lasing. The value of $\hat{a}^+(0)$ will become zero when lasing conditions are satisfied (i.e. transmittivity becomes infinite).

The lower three expressions of Eq. (3.54) are used to resolve three of our four remaining unknown coefficients. The coefficients a_1^+, b_2^+ and a_3^- are expressed in terms of the one remaining unknown coefficient b_4^- as

$$a_1^+ = \Gamma_1 b_4^- , \quad b_2^+ = \Gamma_2 b_4^- , \quad a_3^- = \Gamma_3 b_4^- , \tag{3.55}$$

where

$$\begin{aligned}\Gamma_1 = \Big(&\sigma_{(2,3)}(r^{b+}_{\chi 2} r^{a-}_{c3} r^{b-}_{d4} - r^{b+}_{d2} r^{b-}_{d4}) + \sigma_{(2,4)}(r^{b+}_{d2} r^{a-}_{\chi 3} r^{b-}_{c4} - r^{b+}_{\chi 2} r^{a-}_{\chi 3}) \\ &-\sigma_{(3,4)}(r^{a-}_{c3} r^{b-}_{c4} - 1)\Big)\,(-1)\eta^{-1},\end{aligned} \tag{3.56a}$$

$$\begin{aligned}\Gamma_2 = \Big(&\sigma_{(1,3)}(r^{a+}_{d1} r^{a-}_{c3} r^{b-}_{d4} - r^{a+}_{\chi 1} r^{b-}_{d4}) + \sigma_{(1,4)}(r^{a+}_{\chi 1} r^{a-}_{\chi 3} r^{b-}_{c4} - r^{a+}_{d1} r^{a-}_{\chi 3}) \\ &-\sigma_{(3,4)}(r^{a+}_{c1} r^{a-}_{c3} r^{b-}_{c4} - r^{a+}_{c1})\Big)\,\eta^{-1},\end{aligned} \tag{3.56b}$$

$$\begin{aligned}\Gamma_3 = \Big(&\sigma_{(1,2)}(r^{a+}_{d1} r^{b+}_{d2} r^{b-}_{d4} - r^{a+}_{\chi 1} r^{b+}_{\chi 2} r^{b-}_{d4}) + \sigma_{(1,4)}(r^{a+}_{\chi 1} r^{b-}_{c4} - r^{a+}_{d1}) \\ &-\sigma_{(2,4)}(r^{a+}_{c1} r^{b+}_{d2} r^{b-}_{c4} - r^{a+}_{c1} r^{b+}_{\chi 2})\Big)\,(-1)\eta^{-1},\end{aligned} \tag{3.56c}$$

$$\begin{aligned}\eta = &\,\sigma_{(1,2)}(r^{a+}_{d1} r^{b+}_{d2} r^{a-}_{\chi 3} - r^{a+}_{\chi 1} r^{b+}_{\chi 2} r^{a-}_{\chi 3}) + \sigma_{(2,3)}(r^{a+}_{c1} r^{b+}_{\chi 2} r^{a-}_{c3} - r^{a+}_{c1} r^{b+}_{d2}) \\ &- \sigma_{(1,3)}(r^{a+}_{d1} r^{a-}_{c3} - r^{a+}_{\chi 1}),\end{aligned} \tag{3.56d}$$

and $\sigma_{(j,k)} = e^{i(\Theta_j + \Theta_k)}$.

3.5.2 Electric-Field Expressions

The rotated-frame slowly varying amplitudes of Eq. (3.53) can be written in terms of the single unknown b_4^- using the expressions shown in Eq. (3.55) as

$$\begin{bmatrix} \hat{a}^+(\zeta) \\ \hat{b}^+(\zeta) \\ \hat{a}^-(\zeta) \\ \hat{b}^-(\zeta) \end{bmatrix} = b_4^- \begin{bmatrix} 1 & r^{b+}_{c2} & r^{a-}_{d3} & r^{b-}_{\chi 4} \\ r^{a+}_{c1} & 1 & r^{a-}_{\chi 3} & r^{b-}_{d4} \\ r^{a+}_{d1} & r^{b+}_{\chi 2} & 1 & r^{b-}_{c4} \\ r^{a+}_{\chi 1} & r^{b+}_{d2} & r^{a-}_{c3} & 1 \end{bmatrix} \begin{bmatrix} \Gamma_1 e^{i\Theta_1 \zeta} \\ \Gamma_2 e^{i\Theta_2 \zeta} \\ \Gamma_3 e^{i\Theta_3 \zeta} \\ e^{i\Theta_4 \zeta} \end{bmatrix} = b_4^- \begin{bmatrix} \hat{f}_a^+(\zeta) \\ \hat{f}_b^+(\zeta) \\ \hat{f}_a^-(\zeta) \\ \hat{f}_b^-(\zeta) \end{bmatrix}. \tag{3.57}$$

Each of the unidirectional quantities $f^{\pm}_{(a,b)}$ are closed form and are comprised of complex detunings and coupling coefficients.

3.5.3 Power, Transmittivity, and Reflectivity Expressions

Unidirectional Power Expressions

The power associated with each unidirectional slowly varying amplitudes $a^{\pm}(\zeta)$ and $b^{\pm}(\zeta)$ is given by

$$P_a^{\pm}(\zeta) = |a^{\pm}(\zeta)e^{\pm i\tilde{\beta}_a L\zeta}|^2 = |\hat{a}^{\pm}(\zeta)e^{i(\pm\tilde{\beta}_a L+\phi_a^{\pm})\zeta}|^2 = |\hat{a}^{\pm}(\zeta)|^2, \tag{3.58a}$$

$$P_b^{\pm}(\zeta) = |b^{\pm}(\zeta)e^{\pm i\tilde{\beta}_b L\zeta}|^2 = |\hat{b}^{\pm}(\zeta)e^{i(\pm\tilde{\beta}_b L+\phi_b^{\pm})\zeta}|^2 = |\hat{b}^{\pm}(\zeta)|^2. \tag{3.58b}$$

Normalizing each power expression by the reference value $P_a^+(1)$ eliminates the unknown coefficient b_4^-:

$$\mathbb{P}^{\pm}_{(a,b)}(\zeta) = \frac{P^{\pm}_{(a,b)}(\zeta)}{P_a^+(1)} = \frac{|b_4^-|^2|\hat{f}^{\pm}_{(a,b)}(\zeta)|^2}{|b_4^-|^2|\hat{f}_a^+(1)|^2} = \frac{|\hat{f}^{\pm}_{(a,b)}(\zeta)|^2}{|\hat{f}_a^+(1)|^2}. \tag{3.59}$$

With this final normalization, all unknown coefficients have been removed from the analytic solution to the CMEs.

Longitudinal Waveguide Power Expressions

The normalized longitudinal power in the A and B waveguides is the sum of the respective waveguides counter-propagating unidirectional powers shown in Eq. (3.59):

$$\mathbb{P}_A(\zeta) = \mathbb{P}_a^+(\zeta) + \mathbb{P}_a^-(\zeta) \quad \text{and} \quad \mathbb{P}_B(\zeta) = \mathbb{P}_b^+(\zeta) + \mathbb{P}_b^-(\zeta). \tag{3.60}$$

Transmittivity and Reflectivity

The structure of Fig. 3.1 has two transmittivity values and two reflectivity values. All four quantities are ratios of an output unidirectional power with respect to the input unidirectional power $P_a^+(0) = |\hat{a}^+(0)|^2$ as discussed in the sections above. For this work, transmittivity captures the forward-propagating power ratios while reflectivity captures the backward-propagating powers ratios as

$$T_a = \frac{\mathbb{P}_a^+(1)}{\mathbb{P}_a^+(0)} = \frac{|\hat{a}^+(1)|^2}{|\hat{a}^+(0)|^2} = \frac{|\hat{f}_a^+(1)|^2}{|\hat{f}_a^+(0)|^2}, \tag{3.61a}$$

$$T_b = \frac{\mathbb{P}_b^+(1)}{\mathbb{P}_a^+(0)} = \frac{|\hat{b}^+(1)|^2}{|\hat{a}^+(0)|^2} = \frac{|\hat{f}_b^+(1)|^2}{|\hat{f}_a^+(0)|^2}, \tag{3.61b}$$

$$R_a = \frac{\mathbb{P}_a^-(0)}{\mathbb{P}_a^+(0)} = \frac{|\hat{a}^-(0)|^2}{|\hat{a}^+(0)|^2} = \frac{|\hat{f}_a^-(0)|^2}{|\hat{f}_a^+(0)|^2}, \tag{3.61c}$$

$$R_b = \frac{\mathbb{P}_b^-(0)}{\mathbb{P}_a^+(0)} = \frac{|\hat{b}^-(0)|^2}{|\hat{a}^+(0)|^2} = \frac{|\hat{f}_b^-(0)|^2}{|\hat{f}_a^+(0)|^2}. \tag{3.61d}$$

Lasing threshold is found when *any* of these expressions reach infinity [50]. Physically, an infinite transmittivity or reflectivity corresponds to output power without an input power.

3.6 Conclusion

This chapter introduces a new lasing structure comprised of a lossy-passive waveguide coupled to a uniform diffraction grating coupled to an active-waveguide. Two sets of fourth-order coupled-mode equations and their closed-form electromagnetic-field, power, and transmittivity solutions capture the structures modal interactions and behaviors.

Simplified CMEs and their associated solutions are first developed which neglect evanescent coupling arguing that large waveguide separation and waveguide wavenumber detuning can result in a small and inefficient associated power transfer. Once the three-coupling solutions are developed, CMEs which include evanescent coupling are formulated and the four-coupling solutions derived. These CMEs consider the four independent coupling mechanisms, the four complex-detuning values, the active-region gain coefficient, each waveguide's loss coefficient, and the nonlinearity introduced through Henry's alpha α_H.

These closed-form solutions are expected to provide for physical insights into lasing behaviors though the parameterization of individual model quantities. The derived solutions allow for the design of lasing structures which achieve single-mode operation with desired and optimized characteristics. The photonic-bandgap behaviors, and specifically their placements for degenerate mode suppression, can be initially understood without including the additional complexity of evanescent coupling. Solutions which include evanescent coupling will be later used to understand lasing behaviors once the associated power-transfer efficiency assumptions no longer hold true and evanescent coupling cannot be ignored.

The models presented here properly reduce to solutions which describe a variety of single or dual waveguide, active or passive structures which may include a coupled diffraction grating. Such reduced structures embedded within our four-coupling model include directional couplers, traditional uniform-grating DFB lasers, contra-directional couplers, and filters.

4. Single-Mode DFB Lasing using Photonic-Bandgap Alignment: Lasing Behavior

4.1 Introduction

This chapter leverages the mathematical models and solutions of Chapter 3 to study lasing behavior. Note that the proposed single-mode lasing mechanism is entirely new. Earlier work reports using exchange-Bragg coupling to form the primary lasing modes and suggest using a $\lambda/4$ shift to improve single-mode performance [6]. However, geometries that rely on a $\lambda/4$ shift are expected to exhibit undesirable behaviors such as the gain-margin degradation problem due to poor longitudinal power flatness as discussed in Section 2.6. Using an at-threshold analysis of the previously derived closed-form solutions, both gain-margin and longitudinal power flatness of the described structure will be shown to surpasses that of the traditional $\lambda/4$-shifted DFB laser while also avoiding its complex grating geometries.

Since the proposed structure makes use of an active waveguide and passive waveguide pair, it is applicable to both III/V platforms and hybrid III/V-on-silicon platforms which may be satisfied by integrated-photonic or silicon-photonic circuit process designs. Early works in silicon-evanescent lasers use a $\lambda/4$-shifted diffraction grating sandwiched between an upper active III-V waveguide and a lower silicon waveguide to achieve single-mode lasing [12], [77], [78]. The gain margin and longitudinal power flatness of these lasers are therefor expected to suffer from the same limitations as described above. A DFB laser seeking to take advantage of exchange-Bragg coupling to provide both optical feedback and power coupling across an active and passive waveguide pair was shown to be compatible with a III-V laser stack and silicon-on-insulator (SOI) process, however, no mathematical model was presented to capture the underlying physics or associated lasing behaviors of the structure and a $\lambda/4$-phase shift was again required to achieve single-mode lasing behavior [6], [7].

In this chapter, the previously derived parameterized solutions are used to understand the proposed structure's underlying physics and optimize on its single-mode lasing behavior. Single-mode operation will be characterized by considering threshold gain, gain margin, and longitudinal power flatness as a function of direct-Bragg coefficient, exchange-Bragg coefficient, evanescent coupling coefficient, waveguide detuning, and Henry's alpha.

4.2 Photonic-Bandgap Alignment

Each of the Bragg-coupling processes produces a photonic bandgap. Direct-Bragg coupling produces photonic bandgaps PBG_a and PBG_b, for the A and B waveguides respectively, while exchange-Bragg coupling produces the photonic bandgap PBG_χ, capturing the exchange of power between counter-directional modes across the A and B waveguides. The center of each PBG is characterized by its low transmittivity through the structure, as seen in the general transmittivity for a two-port structure shown in Fig. 4.1.

Since waveguide A of the uniform grating DFB structure shown in Fig. 2.5(a) contains the active region, the modes of the associated PBG$_a$ are the strongest and dominate lasing considerations. Each edge of PBG$_a$ is inhabited by a transmission resonance, as shown in Fig. 4.1. These degenerate modes lead to a lasing mode spectrum without gain margin and result in a laser which is not single mode.

The detuning of the resonance from the center of the bandgap is denoted as ∇_a. The presence of optical gain will strengthen and shift these transmission resonances, which ultimately rise to infinity at lasing threshold. The distance of the resonance R_{+1} relative to the PBG$_a$ center depends upon the normalized coupling strength $\kappa_a L$ and the normalized gain coefficient $g_{net}L$ and is written as

$$R_{+1} = C_a + \nabla_a = \alpha_{_H} gL/2 + \nabla_a. \tag{4.1}$$

The location of this resonance pulls inward toward the PBG edge as gain increases from $gL = 0$ and the structure enters lasing. The change in resonance location as gain increases is shown as the rising dotted line in the Fig. 4.2(a).

The value of $g_{net}L = gL - \alpha_a L$ is the normalized net gain coefficient of the structure, gL is the normalized gain coefficient, and $\alpha_a L$ is the normalized loss coefficient associated with the active region, taken here as $\alpha_a L = 0.25$. The values along the dotted line represent the resonance detuning when the structure is operating at lasing threshold. The threshold separation can be approximated by a ∇_{est} using a simple linear expression

$$\nabla_{est} = (\kappa_a L/2 + 3\pi/4), \tag{4.2}$$

or by the more accurate second order polynomial

$$\nabla_{est} = 0.02322\ (\kappa_a L)^2 + 0.6526\ \kappa_a L + 1.985. \tag{4.3}$$

The error in ∇_{est} for the second-order-polynomial estimate is less than 0.005 when $T_p > 30$ dB for all $\kappa_a L$ as shown in Fig. 4.2(b).

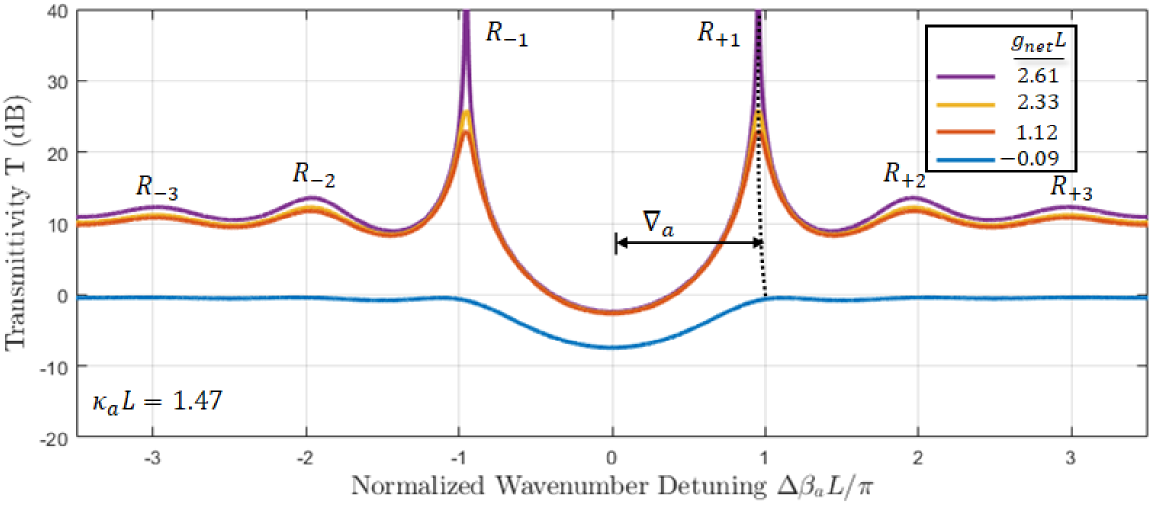

Figure 4.1 Transmittivity spectrum of the uniform-grating DFB lasing structure showing PBGs for various values of net gain coefficient $g_{net}L$ and coupling coefficient $\kappa_a L$. Resonances labeled as R_{+1}, R_{-1}, R_{+2}, and R_{-2}. $g_{net}L = gL - \alpha_a L$ where $\alpha_a L = 0.25$ is used as a representative normalized loss coefficient associated with an active region waveguide.

The center of each PBG, as placed along the $\Delta\beta_a L$ axis, is given as follows:

$$C_a = \alpha_H gL/2, \tag{4.4a}$$

$$C_\chi = \Delta\beta_{ab}L + \alpha_H gL/4, \tag{4.4b}$$

$$C_b = 2\Delta\beta_{ab}L. \tag{4.4c}$$

The center C_a of PBG$_a$ is due to direct-Bragg coupling in waveguide A, the center C_χ of PBG$_\chi$ is due to exchange-Bragg coupling, and the center C_b of PBG$_b$ is due to direct-Bragg coupling in waveguide B. Each center movement as wavguide-wavenumber detuning $\Delta\beta_{ab}L$ changes is illustrated in Fig. 4.3(a) for the nonlinearity $\alpha_H = 0$ and in Fig. 4.3(b) for the nonlinearity $\alpha_H \neq 0$.

In order to suppress the first-order degenerate mode R_{+1}, the center C_χ of the exchange-

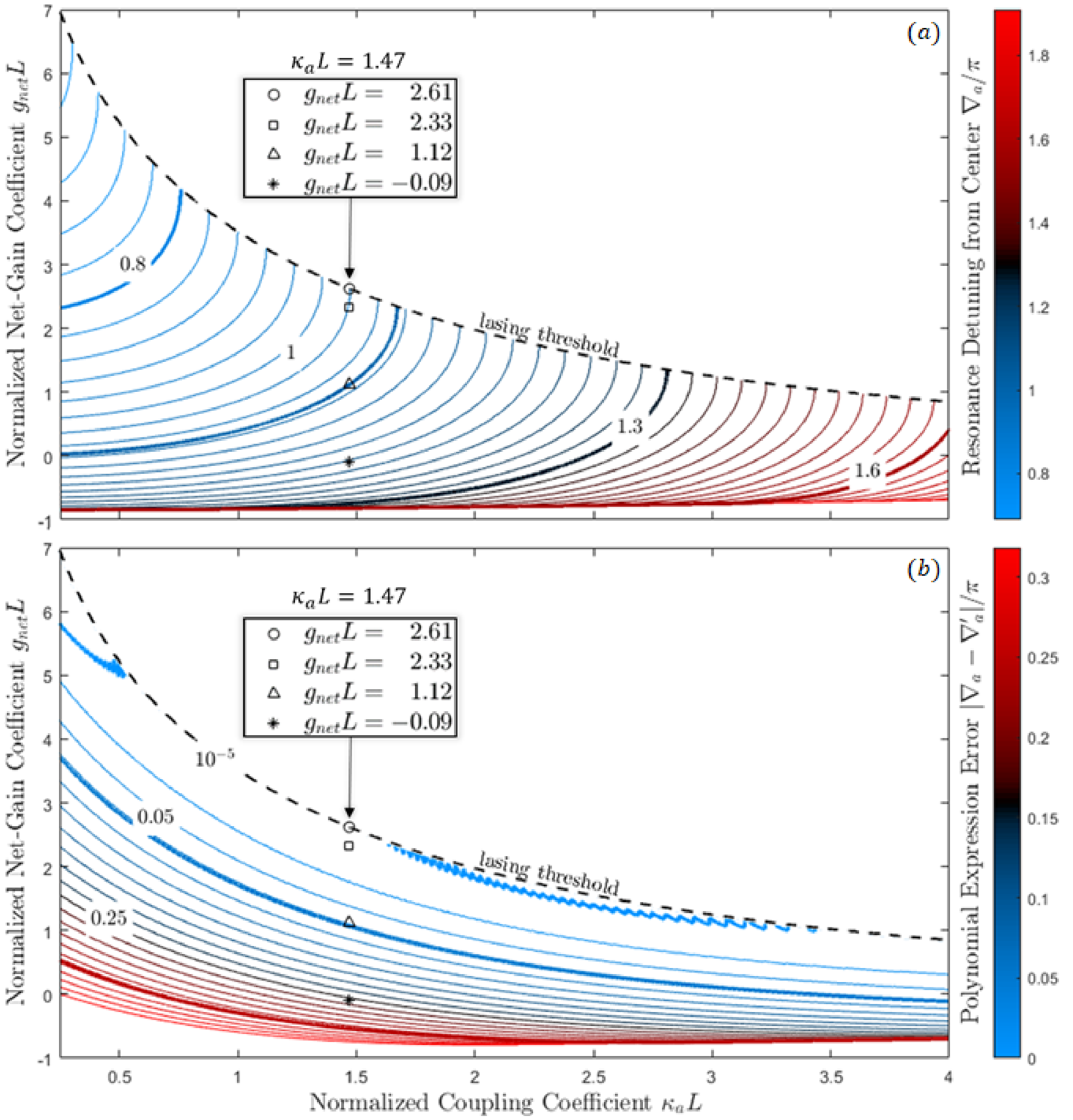

Figure 4.2 Location of the first-order degenerate resonance R_{+1} of a photonic bandgap PBG_a; this resonance will be suppressed by PBG_χ and so its position must be well understood. (a) Resonance separation from center $\nabla_a = R_{+1} - C_a$ of resonance R_{+1} from PBG_a center C_a, showing low variation with $\kappa_a L$ for gL near lasing threshold. (b)Difference between second-order estimated resonance separation ∇_{est} and actual ∇_a, showing low estimate error for gL near lasing threshold.

Bragg PBG$_\chi$ must be matched to its location:

$$C_\chi = R_{+1}, \tag{4.5a}$$

$$\alpha_H gL/4 + \Delta\beta_{ab}L = \nabla_a + \alpha_H gL/2, \tag{4.5b}$$

$$\Delta\beta_{ab}L = \nabla_a + \alpha_H gL/4, \tag{4.5c}$$

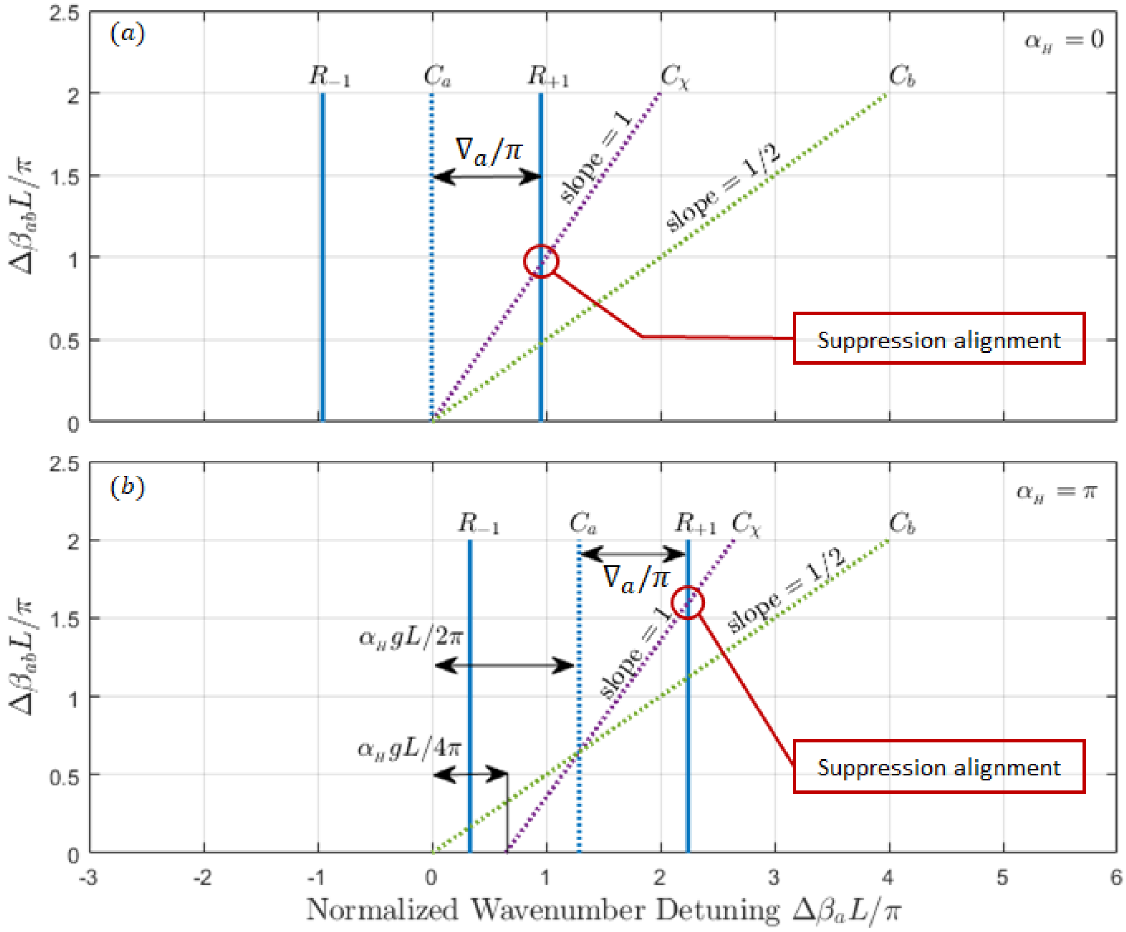

Figure 4.3 Suppression alignment, showing the positions of the photonic-bandgap centers C_a, C_χ, C_b and the $R_{\pm 1}$ degenerate resonances. (a) For $\alpha_H = 0$, the PBGs shift with respect to each other only due to the waveguide wavenumber detuning $\Delta\beta_{ab}L$. (b) α_H introduces a new relative shift of the PBGs. The suppression condition for PBG positioning is $C_\chi = \nabla_a$. $\kappa_a L = 1.47, gL = 2.61$.

where ∇_a is the approximate detuning from the center of PBG_a to its first-order degenerate lasing mode and the second term accounts for a relative PBG shift due to α_H. Thus, suppression alignment is achieved by knowing the resonance position ∇_a, which can be taken from a look-up table of exact values as plotted in Fig. 4.2, found using an estimate ∇_{est} such as that in Eq. (4.3), or be found using an alternate approximation approach. In general, the alignment methods will be some function of gain, semiconductor nonlinearity, and direct-Bragg coupling $\kappa_a L$.

Breaking the degeneracy and achieving single-mode lasing is accomplished by offsetting the PBGs with respect to each other such that suppression alignment occurs when operating at threshold gain $g_{th}L$. The introduced mismatch in wavenumber between the modes in opposite waveguides, as characterized by the waveguide wavenumber detuning $\Delta\beta_{ab}$:

$$\Delta\beta_{ab} = (\beta_a - \beta_b)/2, \tag{4.6}$$

must be such that the conditions of Eq. (4.5) are satisfied when $gL = g_{th}L$.

The offset detuning between PBGs can be further accentuated by noting the interrelation among the four wavenumber detuning quantities; specifically, any two quantities can be used to express the other two. For this work, all equation and figure detunings will use the two quantities $\Delta\beta_a$ and $\Delta\beta_{ab}$; knowing the detuning relationships $\Delta\beta_a = \beta_a - \Lambda$, $\Delta\beta_\chi = \beta_\chi - \Lambda$, and that shown in Eq. (4.6), the remaining detunings $\Delta\beta_b$ and $\Delta\beta_\chi$ can be expressed as

$$\Delta\beta_b = \Delta\beta_a - 2\Delta\beta_{ab}, \tag{4.7a}$$

$$\Delta\beta_\chi = \Delta\beta_a - \Delta\beta_{ab}. \tag{4.7b}$$

Since the nonlinearity $\alpha_{_H}$ only changes the wavenumber of the optical mode in waveguide A, it impacts the relative position of each PBG differently. Specifically, the wavenumber detunings become

$$\Delta\beta_a' = \beta_a' - \beta_\Lambda = \Delta\beta_a - \alpha_{_H} g/2, \tag{4.8a}$$

$$\Delta\beta_\chi' = \beta_\chi' - \beta_\Lambda = \frac{\beta_a' + \beta_b}{2} - \beta_\Lambda = \Delta\beta_\chi - \frac{\alpha_{_H} g}{4}, \tag{4.8b}$$

and $\Delta\beta_b$ is unchanged from Eq. (3.5b). Thus, as the gain is increased, PBG_a will shift by $\beta_{_H} = \alpha_{_H} g/2$, PBG_χ will shift by $\beta_{_H}/2$, and PBG_b will remained fixed in place. These relative shifting must be accounted for to achieve single-mode lasing when operating at lasing threshold.

Note that the modal wavenumber detuning $\Delta\beta_{ab}$ is also associated with evanescent, co-directional coupling between the waveguides, as found in standard directional couplers.

Variation from zero can be understood in terms of a variation in effective refractive index n_a and n_b of either waveguide, where

$$\beta_a = 2\pi n_a/\lambda_0, \qquad \beta_b = 2\pi n_b/\lambda_0, \tag{4.9}$$

and λ_0 is the free-space wavelength. The evanescent coupling efficiency weakens with the deviation from zero $\Delta\beta_{ab}$, as is required for this single-mode lasing mechanism. For this reason, evanescent, co-directional coupling will be discounted from the first model of PBG-based single-mode lasing for structures assuming small evanescent coupling strengths $\kappa_e L < 0.25$. [50]

4.3 Mode Spectrum

Lasing threshold $g_{th}L$ and the normalized active-waveguide threshold detuning $\Delta\beta_{a_{th}}L$ are found by increasing the normalized gain coefficient gL above zero until the transmittivity of Eq. (3.22) becomes infinite, as depicted in Fig. 4.4(a), where the highest value $gL = 2.60 = g_{th}L$. As gL increases, the lasing resonance rises smoothly to infinity whereas all other resonances remain weak. Parameter values for these plots are $\alpha_H = \pi$ and $\kappa_a L = \kappa_\chi L = \kappa_b L/2$, where $\kappa_\chi L = \kappa_{\chi ab} L = \kappa_{\chi ba} L$. In addition, $\alpha_a L = 0.25$ and $\alpha_b L = 0.09$, appropriate values for III/V and silicon waveguides, respectively.

The photonic bandgaps PBG$_\chi$ & PBG$_b$ enable single-mode lasing by suppressing degenerate direct-Bragg resonances of the active waveguide A. To see this action, each underlying PBG is depicted in isolation in Fig. 4.4(b) by setting only its associated coupling coefficient nonzero. PBG$_\chi$ & PBG$_b$ are positioned near the first- and second-order degenerate lasing resonances of PBG$_a$, respectively, by setting $\Delta\beta_{ab}L = 5.13$. Here, the *linear* approximation $\nabla_{est} = (\kappa_a L/2 + 3\pi/4)$ is used which results in the waveguide-wavenumber detuning $\Delta\beta_{ab}L$ shown as a dashed line in Fig. 4.5. The approximate detuning for a given coupling $\kappa_a L$ is taken at gain threshold $gL = g_{th}L$ assuming a Henry's alpha of $\alpha_H = \pi$.

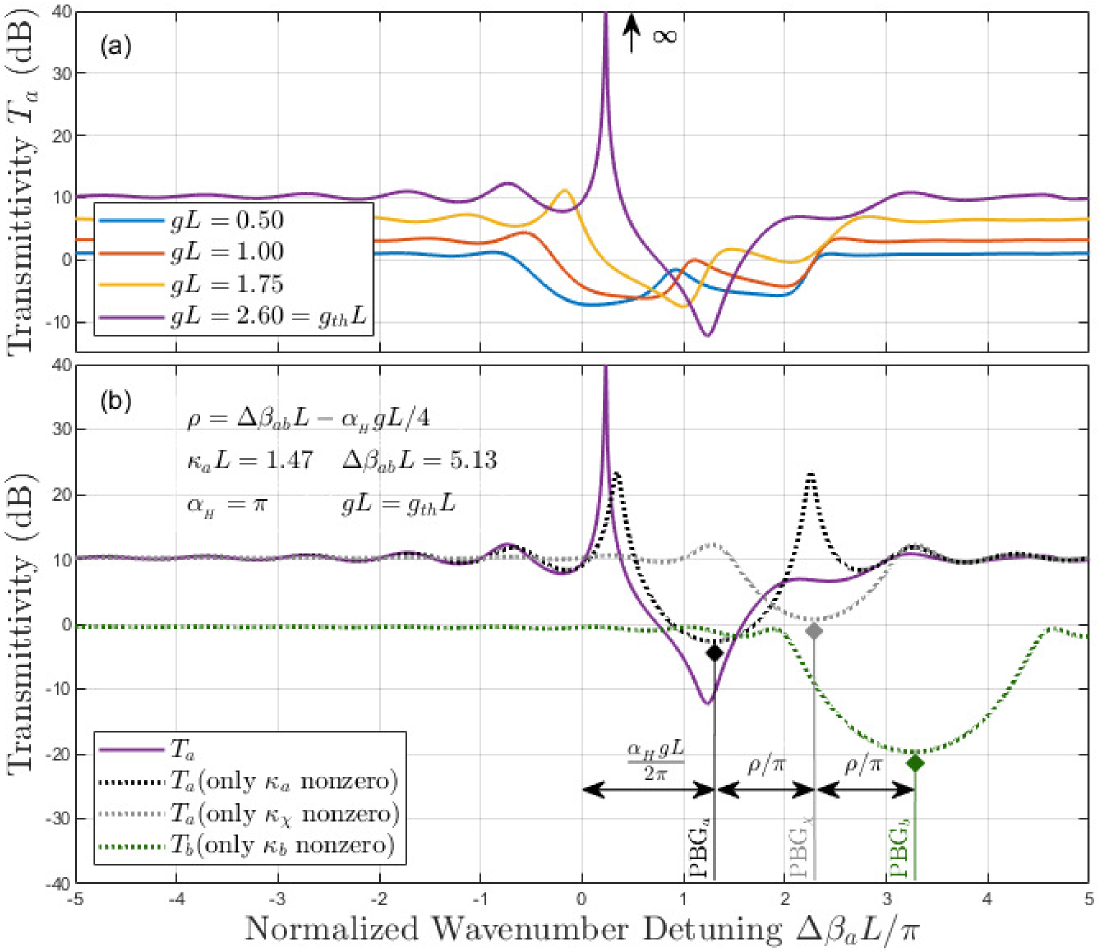

Figure 4.4(a) A single resonance dominates the transmittivity spectrum as gL increases to lasing threshold $g_{th}L$. (b) The transmittivity at $gL = g_{th}L$ for each separate coupling process shows that PBG$_\chi$ and PBG$_b$ can be centered near degenerate lasing modes, thereby suppressing them, by setting $\Delta\beta_{ab}L$.

Determining the threshold gain $g_{th}L$, the threshold wavenumber detuning $\Delta\beta_{ath}L$, and the required waveguide wavenumber detuning $\Delta\beta_{ab}L$ for a structure of fixed coupling is an iterative process. The initial estimate of threshold values $g^0_{th}L$ and $\Delta\beta^0_{ath}L$ is determined by ramping gain gL up from zero until the transmittivity first goes to ∞ for a structure where all coupling values but the desired $\kappa_a L$ have been set to zero. This initial structure is essentially a uniform-grating DFB laser; the lower $\Delta\beta_a L$ degenerate mode will be preserved and is used as the initial estimated value for $\Delta\beta^0_{ath}L$.

An initial waveguide wavenumber detuning $\Delta\beta^0_{ab}L$ is then found using Eq. (4.5c) by

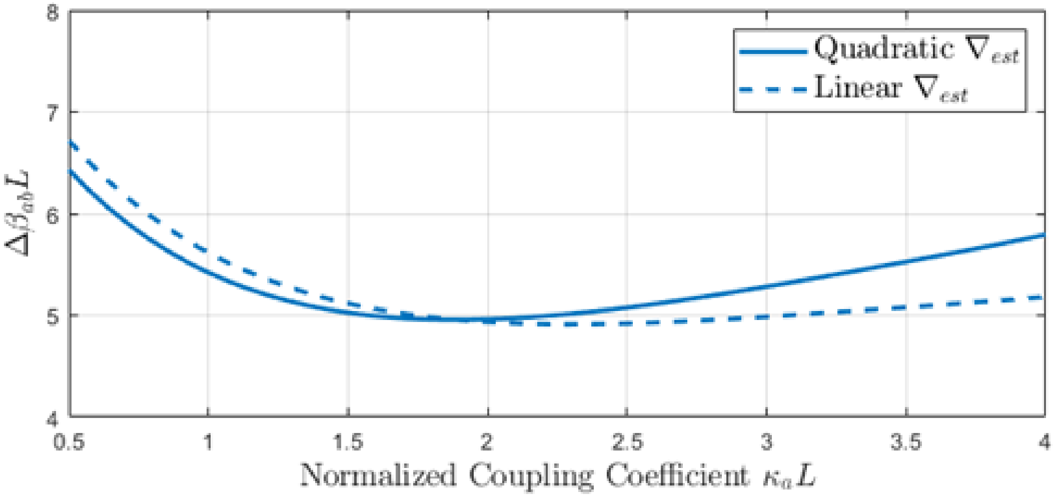

Figure 4.5 The quadratic (solid) and linear (dahed) approximations of the resonance position ∇_{est} used to determine the required waveguide wavenumber detuning $\Delta\beta_{ab}L$ which aligns PBG$_\chi$ over the degenerate mode to realize single-mode lasing. Values used in figure: $gL = g_{th}L,\ \alpha_H = \pi,\ \alpha_a L = 0.25,\ \alpha_b L = 0.09$.

substituting $g^0_{th}L \to gL$. All coupling values of the structure are then reintroduced to their non-zero values and, with the estimated $\Delta\beta^0_{ab}L$, the gain is again increased from zero until lasing occurs. This results in new estimated values of $g^1_{th}L$ and $\Delta\beta^1_{ath}L$. An updated $\Delta\beta^1_{ab}$ is calculated using $g^1_{th}L$ and the process repeats until the value of $g_{th}L$ changes less than 1% per iteration. Stabilization typically occurs after about five iterations of this process.

The set of all threshold pairs for each mode across a range of $\kappa_a L$ produces the mode spectrum plot shown in Fig. 4.6. The purple curve captures the fundamental mode and the black curve the next highest mode. Recalling that, for this structure, $\kappa_a L = \kappa_\chi L = \kappa_b L/2$; in the coupling region $R_2 \in (0.5 \leq \kappa_a L \leq 0.98)$, PBG$_\chi$ does not have sufficient strength to suppress the degenerate lasing mode. As $\kappa_a L$ increases further, so does $\kappa_\chi L$ and PBG$_\chi$'s suppression strength. The secondary lasing mode then shifts from the opposite side to the same side as the fundamental lasing mode at $\kappa_a L = 0.98$. This transition is marked by red dotted line and the R_2 and R_1 regions in Fig. 4.6, respectively.

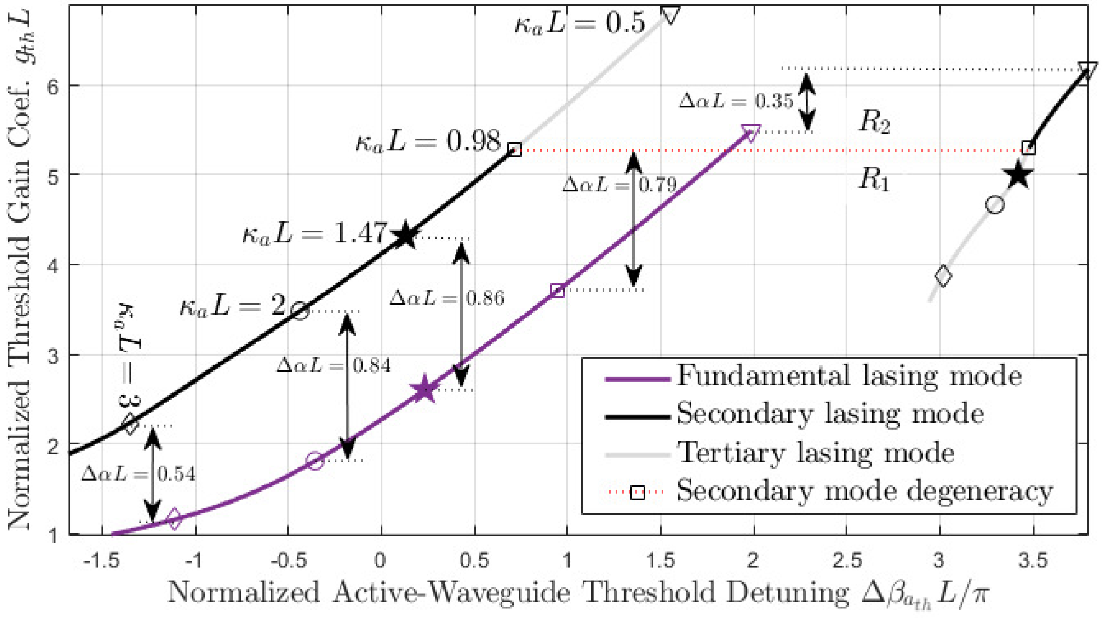

Figure 4.6 Lasing-mode spectrum showing threshold values for 200 values of $\kappa_a L$, five of which are labelled with markers. A large normalized gain margin $\Delta\alpha L = 0.86$ occurs at $\kappa_a L = 1.47$ with threshold values $g_{th}L = 2.60$ and $\Delta\beta_{a_{th}}L = 0.234\pi$.

4.4 Gain Margin

A transmittivity heat map of the structure, shown in Fig. 4.7, demonstrates the fundamental and secondary lasing modes which are found by extending gL through and above $g_{th}L$ to allow each lasing mode to rise for a single fixed value of $\kappa_a L = \kappa_\chi L = \kappa_b L$. Lasing is indicated by bright red, the total-structure PBG is blue, and the shifting of the resonances as gL increases is due to α_H.

Using this figure, a normalized gain margin $\Delta\alpha L = \Delta gL/2 = (g_{th2}L - g_{th}L)/2 = 0.86$ is found at the coupling value of $\kappa_a L = 1.47$ which exceeds the reported limit of 0.735 for $\lambda/4$-shifted DFB lasers and its phase-shift variants at lasing threshold, shown in Fig. 1.4. [34]–[36], [38], [47], [49]. The high gain margin of the proposed structure is due to having both lasing modes on the *same* side of the mode spectrum. The same values of lasing threshold $g_{th}L$ and normalized gain margin $\Delta\alpha L$ are found from transmittivity or reflectivity expressions between any ports of the four-port structure (not shown).

In general, the normalized gain margin is a measure of single-mode stability [35], and,

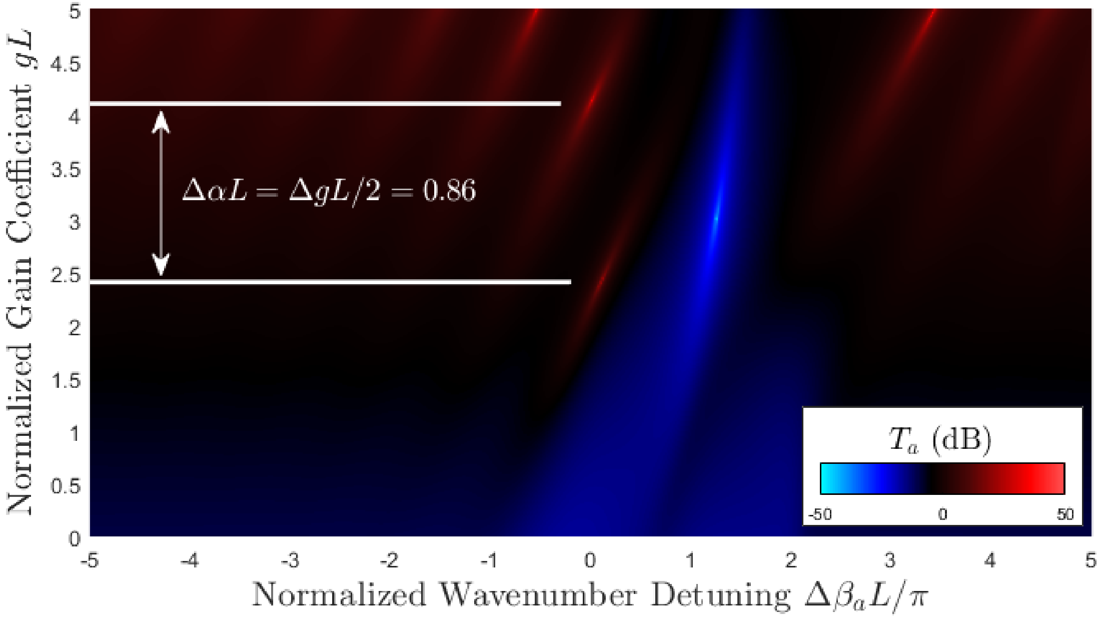

Figure 4.7 Normalized gain margin $\Delta\alpha L = 0.86$ between lasing modes (red) on the same side of the mode spectrum as seen by sweeping the transmittivity T_a over gL to form a transmittivity heat map. The low-order degenerate lasing modes at higher detuning are suppressed. The values used to generate this figure are $\kappa_a L = \kappa_\chi L = \kappa_b L/2 = 1.47$ and $\alpha_H = \pi$.

for a given direct-Bragg coupling $\kappa_a L$ on the mode-spectrum plot of Fig. 4.6, is determined by finding the difference in gain threshold of each low-order mode. This can be visualized as tracing the difference in the purple curve and black curve across this mode-spectrum plot. The region shift from R_2 to R_1 is noted in both figures with the dotted red line.

The gain-margin $\Delta\alpha L$ values for the proposed structure across a span of $\kappa_a L$ are shown in Fig. 4.8. The proposed structure realizes $\Delta\alpha L = 0.87$ at its peak which outperforms the $\lambda/4$-shifted structure peaking at $\Delta\alpha L = 0.735$ [35]. These high gain margins of the proposed lasing structure are due to having both lasing modes on the *same* side of the mode spectrum centered on the amplifying waveguide Bragg wavenumber β_a. The value of waveguide wavenumber detuning $\Delta\beta_{ab} L$ used for each $\kappa_a L$ is shown in Fig. 4.5.

The decline in gain margin for the proposed structure for larger values of $\kappa_a L > 2$ occurs as the fundamental lasing mode enters compression, allowing for the secondary lasing mode to “catch up” as $\kappa_a L$ continues to increase. The transition between regions R_2 and R_1 in the

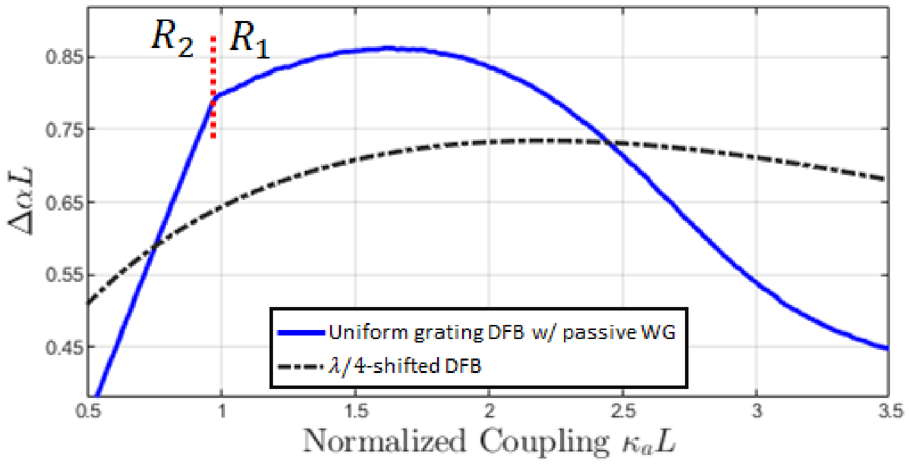

Figure 4.8 At-threshold normalized gain margin $\Delta\alpha L$ for a range of $\kappa_a L$. The new laser structure outperforms the $\lambda/4$-shifted DFB laser. Values used in figure: $\kappa_a L = \kappa_\chi L = \kappa_b L/2$, $gL = g_{th}L$, $\alpha_H = \pi$, $\alpha_a L = 0.25$, $\alpha_b L = 0.09$.

mode-spectrum plot given in Fig. 4.6 correlates to the location of the kink in the gain-margin plot. The fundamental lasing mode compression can be seen in the purple curve of Fig. 4.6 for increasing values of $\kappa_a L$.

4.5 Longitudinal Power Flatness

The power profiles along the active and passive waveguides of the proposed structure are shown at lasing threshold in Fig. 4.9(a) and (b) respectively. The active-waveguide profiles of the uniform-grating and $\lambda/4$-shifted DFB laser structures are also shown in Fig. 4.9(a) for comparison; the poor flatness of the latter degrades its gain margin above lasing threshold [35]. This flatness correlates to the degree of spatial-hole burning occurring for above-threshold operation. High flatness values indicate a non-uniform distribution of optical power in the waveguide. Areas of high photon density along the length of the laser cavity consume free carriers and present localized changes in the index of refraction, worsening as laser output power increases.

The variation in flatness F as a function of $\kappa_a L$ is shown in Fig. 4.10, where again $F = \int_0^1 (\mathbb{P}_A(\zeta) - \mu)^2 d\zeta/\mu^2$, and $\mu = \int_0^1 \mathbb{P}_A(\zeta)\ d\zeta$ [35]. The $\kappa_a L$ value that yields the

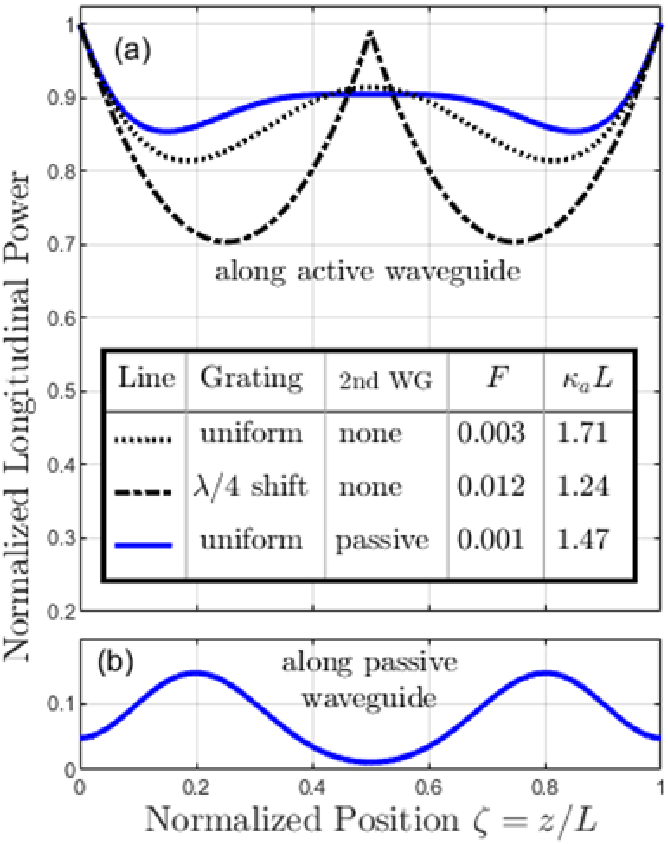

Line	Grating	2nd WG	F	$\kappa_a L$
⋯⋯	uniform	none	0.003	1.71
- · -	$\lambda/4$ shift	none	0.012	1.24
—	uniform	passive	0.001	1.47

Figure 4.9 At-threshold longitudinal power along (a) active waveguide A and (b) passive waveguide B. The power profiles for the $\lambda/4$-shifted DFB and the (degererate) uniform-grating DFB laser are provided for reference. Values used in figure: $\kappa_a L = \kappa_\chi L = \kappa_b L/2,\ gL = g_{th}L,\ \alpha_H = \pi,\ \alpha_a L = 0.25,\ \alpha_b L = 0.09.$

minimum flatness for each lasing structure was used to generate the curves shown in Fig. 4.9.

For the proposed structure, the minimum flatness corresponds to the same local direct-Bragg coupling $\kappa_a L$ region as the peak gain margin, unlike the $\lambda/4$-shifted DFB laser where the two local extrema are separated by larger span of $\kappa_a L$. At minimum flatness, the proposed structure with $\Delta\alpha L = 0.86$ & $F = 0.001$ outperforms the $\lambda/4$-shifted structure with $\Delta\alpha L = 0.68$ & $F = 0.012$. At its slightly higher peak gain margin of $\Delta\alpha L = 0.87$, as shown in Fig. 4.8, the proposed structure realizes a flatness $F = 0.006$, which also outperforms the $\lambda/4$-shifted structure at its gain-margin peak $\Delta\alpha L = 0.735$ and corresponding flatness of $F = 0.25$ [35].

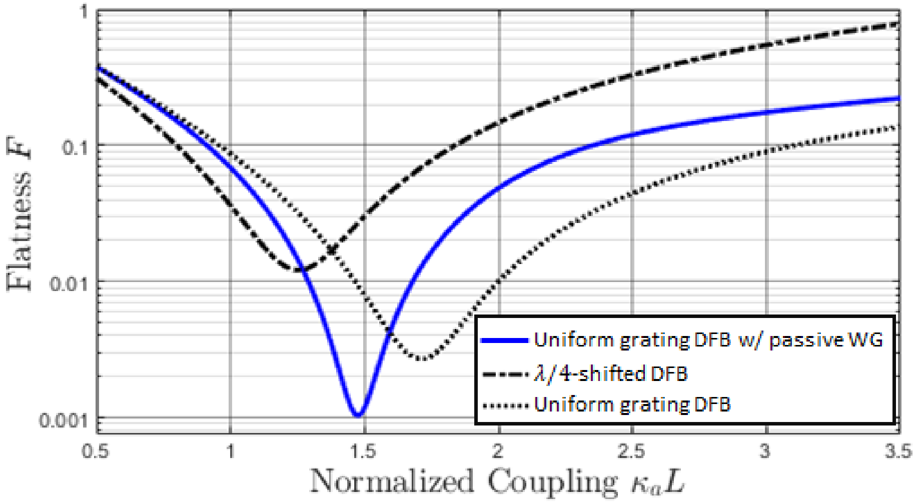

Figure 4.10 The active-waveguide power flatness across normalized direct-Bragg coupling $\kappa_a L$. The minimum flatness of the proposed structure is $F = 0.001$ and occurs simultaneously with the gain margin value of $\Delta\alpha L = 0.86$ out performing the $\lambda/4$-shifted structure whose flatness is $F = 0.012$ with a corresponding gain margin of $\Delta\alpha L = 0.68$. Values used in figure: $\kappa_a L = \kappa_\chi L = \kappa_b L/2,\ gL = g_{th}L,\ \alpha_{_H} = \pi,\ \alpha_a L = 0.25,\ \alpha_b L = 0.09$.

4.6 Impact of Exchange-Bragg Coupling

In the previous section, a relationship between Bragg based coupling coefficients was established as $\kappa_a L = \kappa_\chi L = \kappa_b L/2$. For the remainder of this chapter no such interdependent relationship will continue and coupling values will be independently set and explicitly called out. The values for the normalized loss coefficients of the active waveguide $\alpha_a = 0.25$ and passive waveguide $\alpha_b = 0.09$ will remain unchanged and have been selected based on expected values for III-V and silicon waveguides, respectively. A Henry's alpha $\alpha_{_H} = \pi$ will be used for the rest of this work because it closely matches multi-quantum well gain media [41]. The impact of the exchange-Bragg coupling $\kappa_\chi L = \kappa_{\chi ab} L = \kappa_{\chi ba} L$ on lasing behavior is studied assuming $\kappa_b L = 2.94$, and $\kappa_{ab} L = \kappa_{ba} L = 0$; the impact of the latter evanescent coupling coefficients $\kappa_{ab} L$ and $\kappa_{ba} L$ are studied independently in 4.7 below.

Additionally, photonic bandgap alignment is improved by migrating to the *quadratic* approximation model for ∇_{est} as given in Eq. 4.3. The quadratic waveguide-wavenumber detuning approximation model used moving forward in this work is shown as the solid line

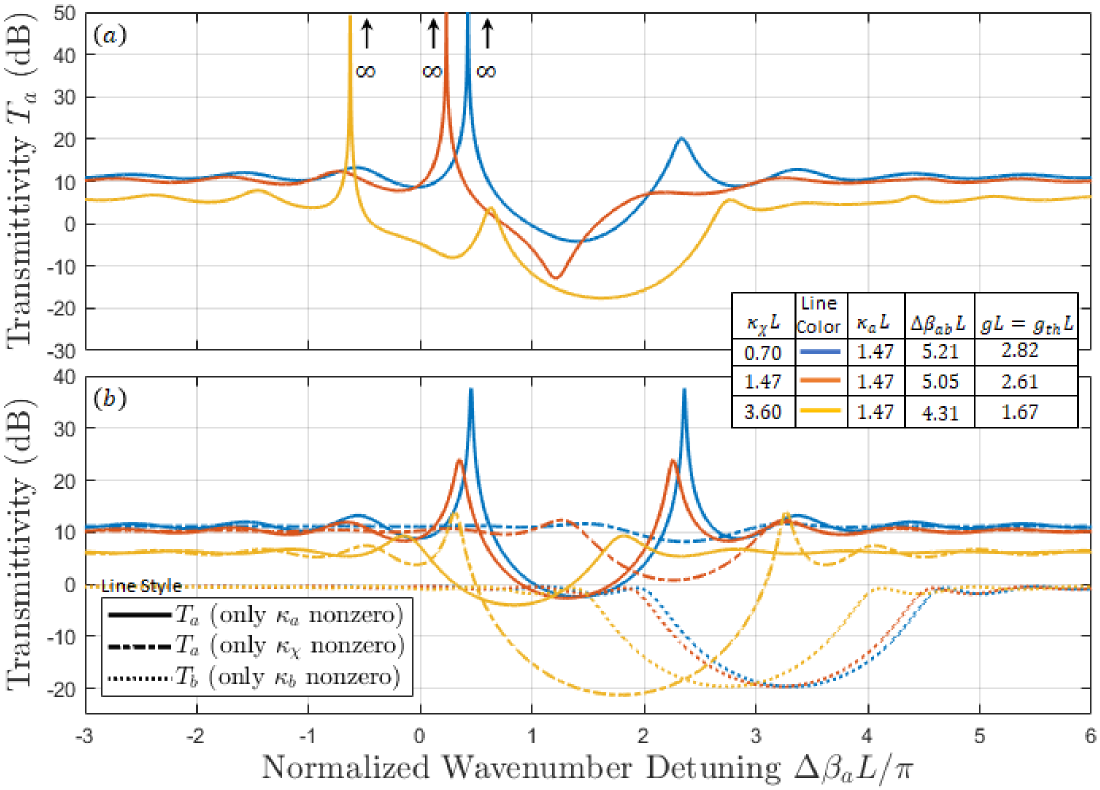

Figure 4.11 Single-mode lasing performance over $\kappa_\chi L$ for three values of $\kappa_a L$. (a) Net spectrum, showing single-mode behavior at lasing threshold. (b) Underlying PBGs at lasing threshold. For all parts: $\kappa_b L = 2.94, \kappa_e L = 0, \alpha_H = \pi, \alpha_a L = 0.25, \alpha_b L = 0.09$.

in Fig. 4.5. The small subtle change in threshold gain between this section at $g_{th}L = 2.61$ and the previous at $g_{th}L = 2.60$ is due to the adoption of the refined alignment estimate function for ∇_{est}.

4.6.1 Single-Mode Lasing and Photonic-Bandgap Alignment

Exchange-Bragg coupling produces the PBG that is used to suppress the degenerate lasing mode. The strength of this suppression is set by the normalized exchange-Bragg coupling coefficient $\kappa_\chi L$. This section explores the dependence of the single-mode laser performance on $\kappa_\chi L$.

The single-mode nature of the lasing structure is evident in the transmittivity at lasing threshold as shown in Fig. 4.11(a) for three different values of exchange-Bragg coupling

$\kappa_\chi L \in \{0.7,\ 1.47,\ 3.60\}$ and a fixed value of $\kappa_a L = 1.47$. For a fixed value of $\kappa_a L$, increasing the $\kappa_\chi L$ of the structure lowers the gain threshold $g_{th}L$ and shifts the lasing resonance in negative $\Delta\beta_a L$.

For the small value of $\kappa_\chi L = 0.70$, suppression of the degenerate mode is marginal even though proper PBG alignment has been achieved. The family of blue curves in Fig. 4.14(b) demonstrates this as T_a for κ_χ (dot-dashed line) is seen properly aligned to the degenerate mode of T_a for $\kappa_a L$ (solid line) but does not have sufficient bandgap depth to fully suppress the lasing mode.

Increasing $\kappa_\chi L = 1.47$ fully suppresses the degenerate mode and results in the clean single-mode transmittivity, shown in red, of Fig. 4.14(a). The family of red curves in Fig. 4.11(b) shows both alignment and suppression strength of PBG$_\chi$ against the degenerate lasing mode.

Further increase of $\kappa_\chi L = 3.60$ continues to demonstrate single-mode lasing behavior, however, a new degenerate mode begins to form in the yellow transmittivity plot of Fig. 4.14(a). The family of yellow curves shown in Fig. 4.14(b) demonstrate an aligned PBG$_\chi$ that has grown in width and resonant strength due to the increased exchange-Bragg coupling coefficient. The new degenerate mode forming in the composite lasing transmittivity plot is due to the exchange-Bragg resonance itself approaching lasing as seen by the increased peaks on each side of PBG$_\chi$.

The photonic bandgap PBG_b remains relatively unchanged as the increase in the coupling $\kappa_\chi L$ has no direct impact on the isolated PBG$_b$. The slight shift in the curves is due to the required change in waveguide wavenumber detuning $\Delta\beta_{ab}L$ to maintain PBG_χ alignment.

4.6.2 Mode Spectrum & Gain Margin

The mode spectrum is now taken for increasing $\kappa_\chi L$ between 0.5 (square marker) and 4.0 (triangle marker) and is shown in Fig. 4.12, for a fixed $\kappa_a = 1.47$. The fundamental lasing mode, shown in purple, traces a contiguous path as κ_χ is varied. However, the secondary

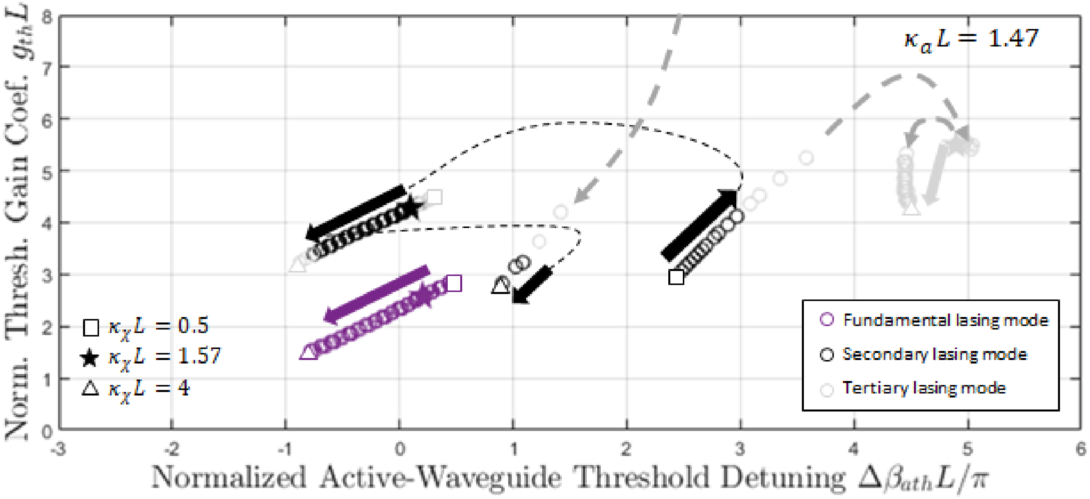

Figure 4.12 The mode spectrum over 200 values of $\kappa_\chi L$ for a fixed value of $\kappa_a L$. $\kappa_b L = 2.94, \kappa_{ab} L = 0, \kappa_{ba} L = 0, \alpha_H = \pi, \alpha_a L = 0.25, \alpha_b L = 0.09$.

lasing mode, shown in black, jumps between three different resonances as κ_χ is varied, producing three distinctive regions.

For the mid range of $\kappa_\chi L$ between 1.07 and 3.07, the secondary mode is located near a detuning $\Delta\beta_{ath}L = 0$ and corresponds to a PBG_a resonance on the same side of as the fundamental mode. This region is characterized by a high gain margins above 0.77 that increase with an increase in κ_χ, shown in Fig. 4.13(a). The gain margin reaches a peak value of $\Delta\alpha L = 1.05$ at $\kappa_\chi L = 3.14$ for the red $\kappa_a L = 1.14$ case.

The weaker values of $\kappa_\chi L$ below 1.07, do not result in a strong enough PBG_χ to completely suppress the degenerate mode R_{+1}. Therefore the secondary mode corresponds to the degenerate R_{+1} resonance, occurring on the *opposite* side of PBG_a as the fundamental mode and near a detuning $\Delta\beta_{ath}L = 3$ in the mode spectrum of Fig. 4.12. Accordingly, this region is associated with the gain margin that drops precipitously at low values of $\kappa_a L$, as seen in Fig. 4.13(a).

As mentioned above, for stronger values of $\kappa_\chi L$ above 3.07, PBG_χ becomes so strong that, although it completely suppresses the degenerate mode R_{+1}, it builds a resonances of its own that takes over as the secondary lasing mode. This new mode occurs within PBG_a

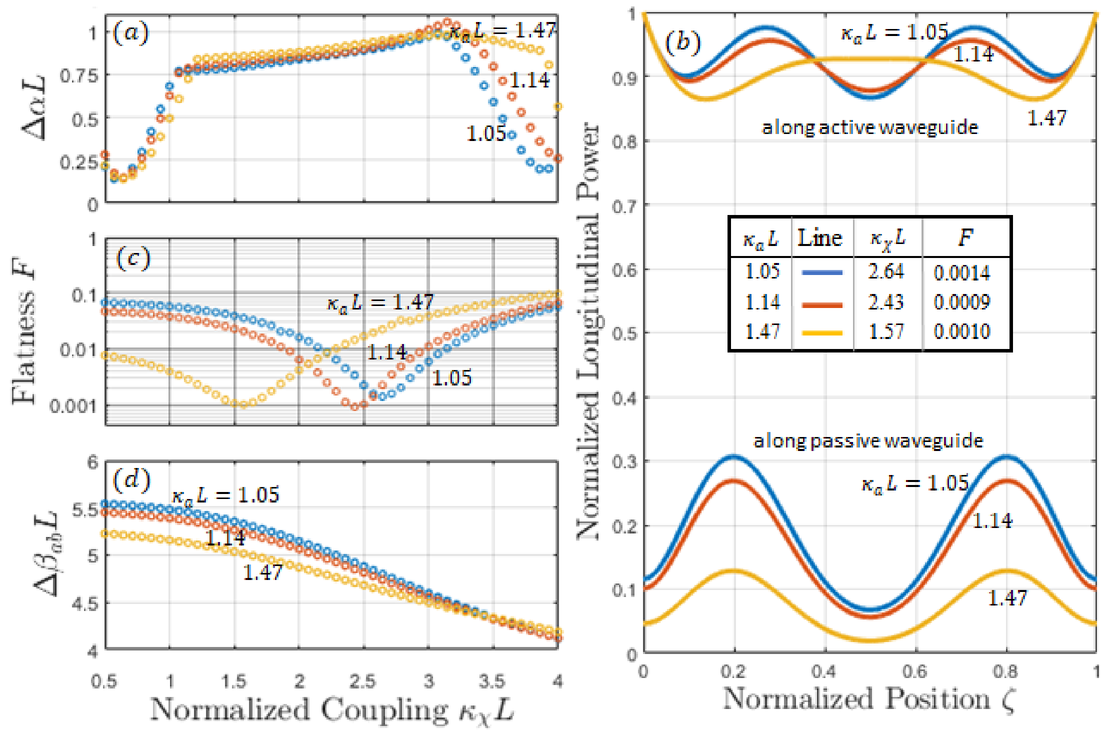

Figure 4.13 Lasing behaviors over three values of $\kappa_\chi L$ showing (a) gain-margin, (b) longitudinal power profiles, (c) flatness, and (d) required waveguide wavenumber detuning using the *quadratic* ∇_{est} approximation. For all figures: $\kappa_b L = 2.94, \kappa_{ab} L = 0, \kappa_{ba} L = 0, \alpha_H = \pi, \alpha_a L = 0.25, \alpha_b L = 0.09$.

and at a detuning $\Delta\beta_{ath} L$ near 1 in the mode-spectrum figure. Thus, strong values of $\kappa_\chi L$ are associated with a sharp reduction in gain margin, as seen in Fig. 4.13(a). Note that as $\kappa_a L$ is increased, PBG_a itself works to suppress this unwanted resonance of PBG_χ, resulting in the extended gain margin as seen by the yellow “○” curve in Fig. 4.13(a).

4.6.3 Longitudinal-Power Profiles & Flatness

The minimum longitudinal-power profiles are shown in Fig. 4.13(b) for the three selected values of $\kappa_a L$. In all cases the power flatness in the active region is exceptionally low, reaching a minimum value of $F = 0.0009$ for $\kappa_a L = 1.14$ and $\kappa_\chi L = 2.43$. The required exchange-Bragg coupling $\kappa_\chi L$ to realize minimum flatness decreases as direct-Bragg coupling $\kappa_a L$ increases.

The variation in flatness F as a function of $\kappa_\chi L$ and for three values of $\kappa_a L$ is shown in Fig. 4.13(c). As $\kappa_a L$ is decreased, the minimum-flatness point shifts to higher values of $\kappa_\chi L$; accordingly, the minimum-flatness point is associated with higher gain margin. The minimum flatness $F = 0.0009$ for the $\kappa_a L = 1.14$ curve occurs at an exchange-Bragg coupling value of $\kappa_\chi L = 2.43$ and corresponds to a large gain margin value of $\Delta\alpha L = 0.89$. Moreover, the peak gain margin $\Delta\alpha L = 1.05$ at $\kappa_\chi L = 3.14$ occurs with a $\kappa_a L = 1.14$ and results in a longitudinal power-flatness of $F = 0.017$. For comparison, the *minimum* flatness $F = 0.012$ of the traditional $\lambda/4$-shifted DFB laser has an associated gain margin of only $\Delta\alpha L = 0.68$.

4.6.4 Waveguide-Wavenumber Detuning

The required waveguide wavenumber detuning $\Delta\beta_{ab}L$ to maintain suppression and which satisfies Eq. (4.5c) varies only slightly across the three values of $\kappa_a L$, as seen in Fig. 4.13(d). The decrease in threshold gain $g_{th}L$ as $\kappa_\chi L$ increases, seen in the purple curve of Fig. 4.12, causes $\Delta\beta_{ab}L$ to decline due to the relatively large Henry's alpha $\alpha_H = \pi$.

4.7 Impact of Evanscent Coupling

Evanescent coupling can cause power transfer between waveguides, and is the basis for the well-known directional coupler [68]. Such coupling is most efficient when the waveguides have matching wavenumbers, referred to as synchronous operation and expressed as $\Delta\beta_{ab}L = 0$. This efficiency is decreased in asynchronous operation, where the waveguide wavenumbers no longer match [68]. In the context of the proposed laser structure, where asynchronous operation of $\Delta\beta_{ab}L \approx 5$ is required for relative PBG alignment, evanescent coupling has been neglected provided $\kappa_e L \leq 0.25$ [50], where $\kappa_e L = \sqrt{\kappa_{ab}L\kappa_{ba}L}$ [79]. In this case, the power-transfer efficiency of the evanescent coupling structure taken in isolation is held to 1%. This section explores the dependence of the single-mode laser performance on the evanescent coupling strength $\kappa_e L$ beyond 0.25.

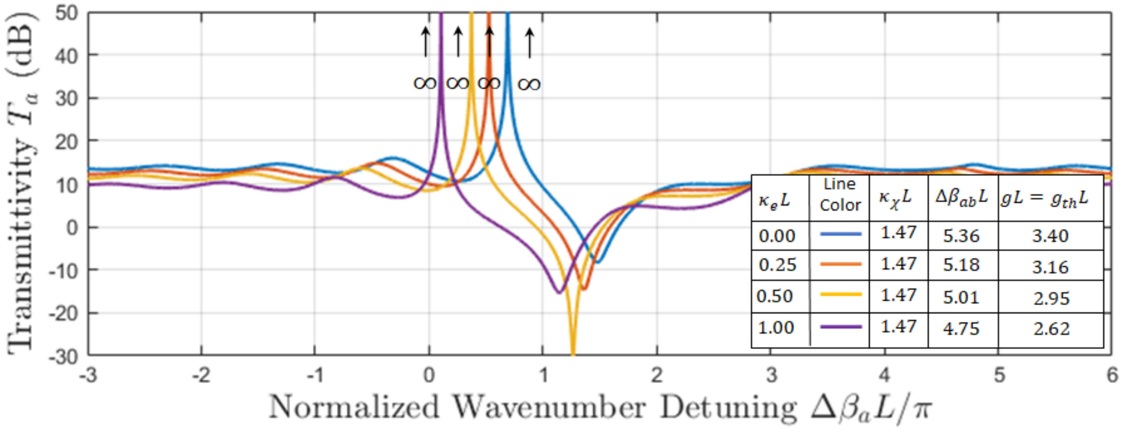

$\kappa_e L$	Line Color	$\kappa_\chi L$	$\Delta\beta_{ab} L$	$gL = g_{th} L$
0.00	🟦	1.47	5.36	3.40
0.25	🟧	1.47	5.18	3.16
0.50	🟨	1.47	5.01	2.95
1.00	🟪	1.47	4.75	2.62

Figure 4.14 Single-mode lasing performance over $\kappa_\chi L$ for four values of evanescent coupling $\kappa_e L$. (a) Underlying PBGs at lasing threshold. (b) Net spectrum, showing single-mode behavior at lasing threshold. For all parts: $\kappa_a L = 1.05$, $\kappa_b L = 2.94$, $\alpha_H = \pi$, $\alpha_a L = 0.25$, $\alpha_b L = 0.09$.

The inclusion of a non-zero $\kappa_e L$ adds a second coupling method to transfer power between the A and B waveguides. Unlike exchange-Bragg coupling which transfers power between contra-propagating waves of each waveguide, evanescent coupling transfers power between co-propagating waves of each waveguide. This exchange of power through two separate but co-dependent coupling mechanisms complicates the longitudinal-power profiles.

4.7.1 Single-Mode Lasing & Gain Margin

The impact of evanescent coupling on the single-mode lasing spectrum is illustrated in Fig. 4.14. Increasing $\kappa_e L$ does not prohibit lasing, but actually decreases the gain threshold $g_{th} L$, as listed in the figure table. This lower gain level results in a shift in the lasing mode to lower values of $\Delta\beta_a L$ due to α_H as expressed by Eq. (4.4a). In this section, $\kappa_a L = 1.05$, the case which provides the worst minimum flatness F in Fig. 4.13(c). It will be seen below, that evanescent coupling can work to improve this flatness value.

The mode spectrum of the proposed lasing structure without evanescent coupling (i.e. $\kappa_e L = 0.0$) and direct-Bragg coupling of $\kappa_a L = 1.05$ for an increasing $\kappa_\chi L$ is shown in Fig. 4.15(a). The regions of suppression are shown as the three black curves starting on the

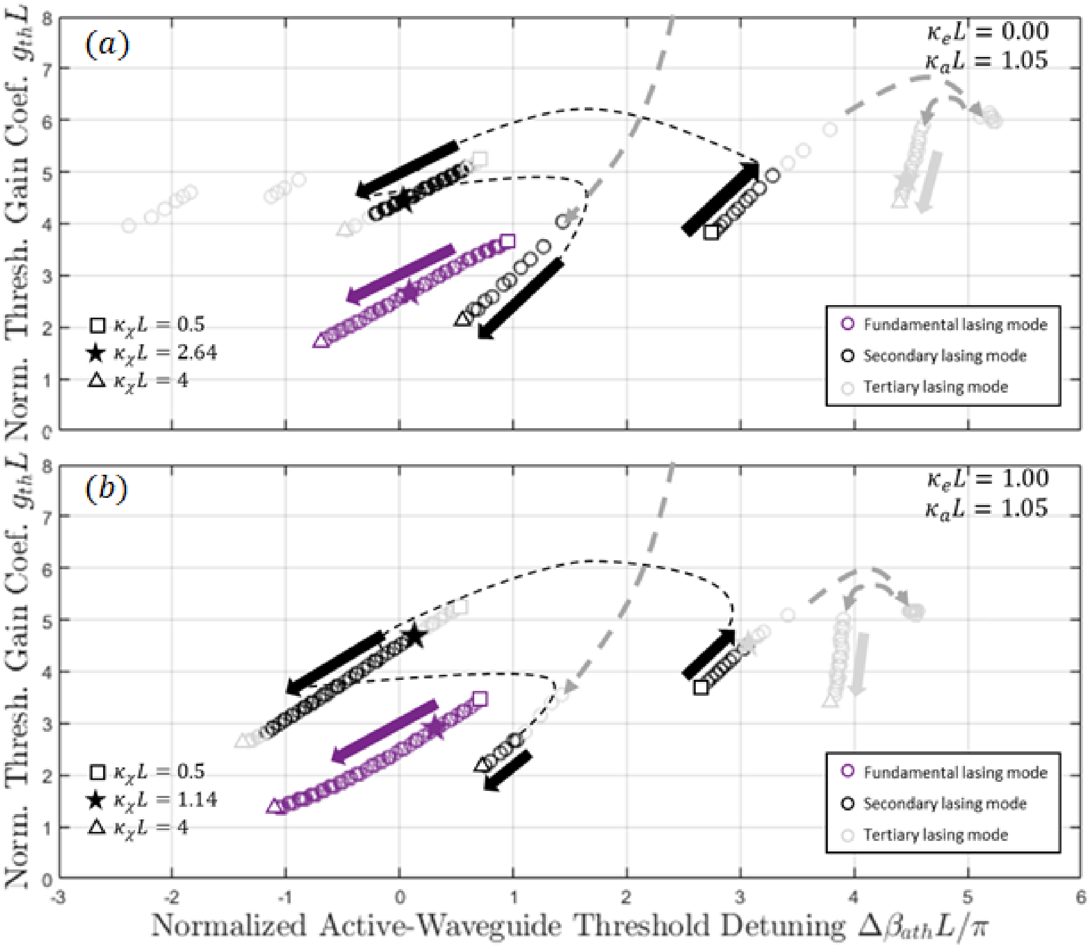

Figure 4.15 The mode spectrum over 200 values of $\kappa_\chi L$ for (a) $\kappa_e L = 0.00$ and (b) $\kappa_e L = 1.00$. For all parts: $\kappa_a L = 1.05,\ \kappa_b L = 2.94,\ \alpha_H = \pi, \alpha_a L = 0.25, \alpha_b L = 0.09$.

opposite-side mode and ending on the exchange-Bragg resonance at the center of the figure. The desired region of operation is the same-side resonance covering the $\kappa_\chi L \in (1.25, 3.20)$ span where gain margin will be at its highest and flatness at its lowest. The point of minimum flatness occurs at $\kappa_\chi L = 2.64$ and is noted with the black star.

Increasing evanescent coupling to $\kappa_e L = 1.0$ shows that sufficient suppression starts slightly later at $\kappa_\chi L = 1.14$ but ends further out at $\kappa_\chi L = 3.60$ thereby increasing the span over which same-side operation occurs. With the inclusion of evanescent coupling, the minimum flatness location shifts up to $\kappa_\chi L = 1.14$. Finally, it is noted that the fundamental mode shifts down in threshold gain entering compression earlier and reducing the structures gain margin for larger $\kappa_\chi L$.

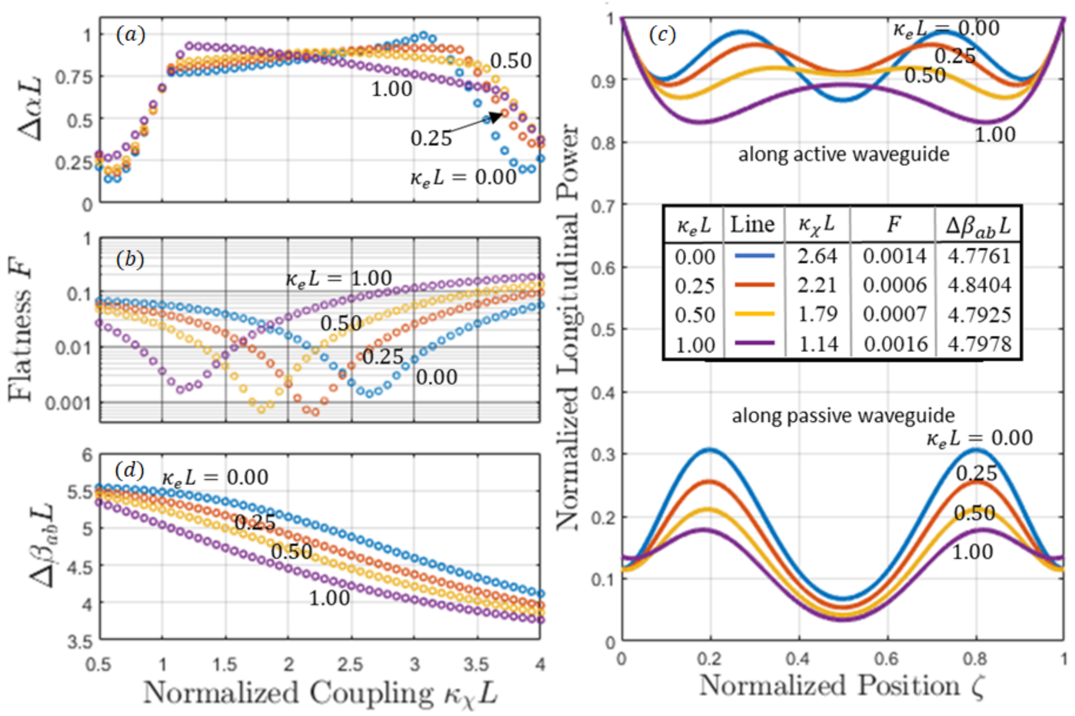

$\kappa_e L$	Line	$\kappa_\chi L$	F	$\Delta\beta_{ab} L$
0.00	🟦	2.64	0.0014	4.7761
0.25	🟧	2.21	0.0006	4.8404
0.50	🟨	1.79	0.0007	4.7925
1.00	🟪	1.14	0.0016	4.7978

Figure 4.16 Lasing behaviors over four values of $\kappa_e L$ showing (a) gain-margin, (b) flatness, (c) longitudinal power profiles, and (d) required waveguide wavenumber detuning. For all parts: $\kappa_a L = 1.05,\ \kappa_b L = 2.94,\ \alpha_H = \pi, \alpha_a L = 0.25, \alpha_b L = 0.09$.

The gain margin for the four values of $\kappa_e L \in \{0.0,\ 0.25,\ 0.5,\ 1.0\}$ are plotted across exchange-Bragg coupling strength $\kappa_\chi L$ in Fig. 4.16(a). For the center region characterized by relatively high gain margin, evanescent coupling has the effect of tilting the slope of the gain margin with respect to $\kappa_\chi L$. Whereas $\kappa_e L = 0.0$ produces a positive slope, an increase in $\kappa_e L$ above zero adds negative slope, with pivot point of negligible gain-margin change near $\kappa_\chi L = 2.21$. Notably, $\kappa_e L = 0.5$ provides a relatively consistent gain-margin within 0.07 of 0.89 over a wide span of $\kappa_\chi L \in (1.1, 3.5)$. Furthermore, an increase in evanescent coupling pushes out the kink in gain margin at higher levels of $\kappa_\chi L$; evanescent coupling weakens the degenerate mode strength of PBG_χ which dominates as the secondary lasing mode at high $\kappa_\chi L$.

4.7.2 Longitudinal-Power Profiles & Flatness

The impact of evanescent coupling on the power flatness F is illustrated in Fig. 4.16(b) by plotting over a range of $\kappa_\chi L$ and for several values of $\kappa_e L$. For the baseline case of $\kappa_e L = 0$, the minimum flatness value $F = 0.0014$ occurs at $\kappa_\chi L = 2.64$. As $\kappa_e L$ is increased above zero, the point of minimum flatness shifts to a lower value of $\kappa_\chi L$. The value of minimum flatness actually drops below 0.001, being 0.0006 and 0.0007 for $\kappa_e L = 0.25$ and 0.5, respectively, as seen in Fig. 4.16(b).

The shift in the point of minimum flatness F tracks well with the rise in gain margin, as evident by comparing Figs. 4.16(a) and (b). For $\kappa_e L = \{0.0,\ 0.25,\ 0.5,\ 1.0\}$, $\Delta\alpha L = \{0.906,\ 0.880,\ 0.872,\ 0.876\}$. All of these values exceed the gain margin of 0.65 for an optimal flatness of $F = 0.012$ for the reference $\lambda/4$-shifted DFB laser.

The longitudinal power profiles corresponding to the minimum flatness F for each value of $\kappa_e L$ are shown in Fig. 4.16(c). Within the active waveguide, $\kappa_e L = 0$ corresponds to a power profile having a valley in the center of the structure ($\zeta = 0.5$); as evanescent coupling increases, this valley flattens and ultimately inverts for $\kappa_e L = 1$. The interim values of $\kappa_e L$ exhibit the lowest values of flatness F. It can be concluded that evanescent coupling as small as $\kappa_e L = 0.25$ will appreciably impact both gain margin and flatness.

4.7.3 Waveguide-Wavenumber Detuning

The waveguide-wavenumner detuning $\Delta\beta_{ab} L$ required to achieve degenerate-mode suppression via Eq. (4.5c) is shown in Fig. 4.16(d) for all values of $\kappa_e L$. As $\kappa_e L$ is increased above zero, lasing threshold decreases and the required waveguide-wavenumber detuning to maintain suppression correspondingly shifts to lower values of $\Delta\beta_{ab} L$.

4.8 Conclusion

This chapter studies a new means of achieving single-mode lasing by suppressing degenerate modes on one side of the uniform-grating DFB lasing spectrum. The high gain margin $\Delta\alpha L = 0.86$ at lasing threshold, low power flatness $F = 0.001$ in the active region, and lack of a $\lambda/4$ shift are promising for good gain margin above lasing threshold.

Single-mode lasing has been explored for a dual-waveguide direct-Bragg, exchange-Bragg, and evanescently coupled distributed feedback structure. This lasing structure introduces a second coupled waveguide to the original single-waveguide uniform diffraction-grating laser introduced in [4]. This approach takes advantage of the exchange-Bragg photonic bandgap, created with the introduction of the second waveguide, to suppress the degenerate mode and, by doing so, avoids the peaky longitudinal power profile such as seen in the ubiquitous $\lambda/4$-shifted DFB laser.

It has been shown that exchange-Bragg photonic bandgap PBG_χ can be aligned to the degenerate lasing mode through the proper selection of waveguide wavenumber detuning $\Delta\beta_{ab}L$, resulting in a single-mode laser which avoids the undesired phase-shift associated with the ubiquitous $\lambda/4$-shifted DFB laser. This alignment can be maintained even as Henry's alpha α_H is introduced. Furthermore, the suppression strength of PBG_χ is controlled through the exchange-Bragg coupling value $\kappa_\chi L$, resulting in a single-mode laser capable of very high gain margin $\Delta\alpha L = 1.05$ and low longitudinal power-profile flatness $F = 0.017$.

The models inclusion of evanescent coupling demonstrated that values as small as $\kappa_e L = 0.25$ impact laser performance and, in some cases, can be used to improve on both gain margin and power flatness. Evanescent coupling can be used to maintain consistent gain margin across a span of $\kappa_\chi L$. Furthermore, increasing $\kappa_e L$ serves to delay the unwanted mode associated with PBG_χ, which occurs at larger values of $\kappa_\chi L$, extending the same-side secondary lasing-mode span. A structure with an evanescent coupling coefficient of $\kappa_e L = 0.25$, can have a flatness as low as $F = 0.0006$ and a gain margin of $\Delta\alpha L = 0.87$, both values which exceed those of the industry standard $\lambda/4$-shifted DFB laser.

5. Single-Mode DFB Lasing using a Coupled NIM Waveguide: Theory

5.1 Introduction

This chapter lays the foundation for a second new type of distributed feedback (DFB) lasing mechanism whose optical feedback is due to the evanescent coupling between an active positive-index material (PIM) waveguide and a lossy negative-index metamaterial (NIM) waveguide. Because optical feedback is accomplished though an evanescent coupling process and does not employ a diffraction grating, the $\lambda/4$-shift, which is often used to achieve single-mode lasing in traditional DFB lasers, and its associated nonlinear behaviors, can be avoided [5], [35]. Active PIM-NIM coupled-mode equations are presented and solved to characterize the dispersion relation, resonant optical gain, and lasing.

A new method for achieving DFB has been recently proposed and modeled based on the evanescent coupling of a positive-index material (PIM) waveguide to a negative-index metamaterial (NIM) waveguide [51]–[53]. Metamaterials offer remarkable electrodynamic behavior stemming from a *negative* refractive index [54]; despite having a negative refractive index, a NIM sandwiched between PIM has been predicted to support the propagation of a guided optical mode [55]–[57]. Notably, the Poynting vector of an optical field traveling through a NIM waveguide can have the direction *opposite* as the associated wave vector [53], [55]. Such a NIM waveguide, when evanescently coupled to PIM waveguide, creates a

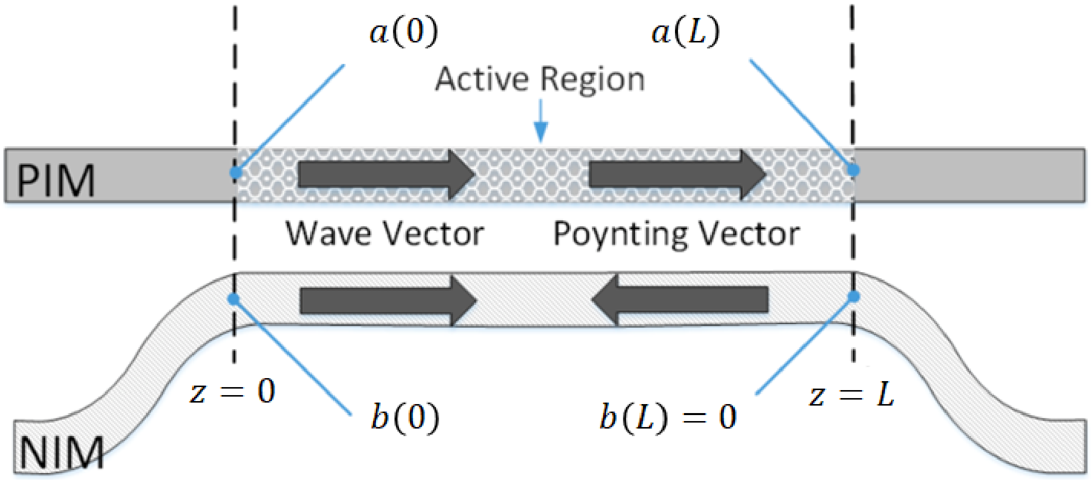

Figure 5.1 Single-mode coupled NIM lasing structure, where the active region of a PIM waveguide is evanescently coupled to a lossy NIM waveguide over length L. The (white) cladding regions surrounding the waveguides are PIM. The counter-directional nature of the Poynting vectors in either waveguide results in distributed feedback, resonant optical gain, and, ultimately, lasing.

distributed coupling region where power flows in either longitudinal direction [51].

Coupled-mode equations for the PIM-NIM structure were first presented for passive, lossless waveguides and revealed a reflectivity spectrum characteristic of DFB [51]. Coupled-mode equations were then extended to the case of a nonlinear lossless PIM-NIM structure and used to study optical bistability [52]. These studies were performed for *passive* structures.

In the proposed structure, PIM-NIM DFB is leveraged to form a new kind of DFB laser. Specifically, an *active* PIM-NIM structure in which the gain is provided by the PIM waveguide over the length of the coupling region L is considered, as shown in Fig. 5.1. To study this active structure, the PIM-NIM coupled-mode equations are extended to include gain for the PIM waveguide and loss for the NIM waveguide. This model predicts the occurrence of lasing with unique dependencies on waveguide parameters not found in traditional active DFB structures.

5.2 Coupled-Mode Equations

The electric field for the composite A (PIM) and B (NIM) waveguide structure shown in Fig. 5.1 is given by:

$$\mathbf{E}(x,y,z,t) = \left(\mathbf{E}_A(x,y,z) + \mathbf{E}_B(x,y,z)\right) e^{-i\omega t}, \tag{5.1}$$

where

$$\mathbf{E}_A(x,y,z) = a(z)\mathbf{e}_a(x,y)e^{i\tilde{\beta}_p^a z}, \tag{5.2a}$$

$$\mathbf{E}_B(x,y,z) = b(z)\mathbf{e}_b(x,y)e^{i\tilde{\beta}_p^b z}. \tag{5.2b}$$

The expressions $a(z)$ and $b(z)$ are the longitudinally varying amplitudes for the A and B waveguides respectively, $\tilde{\beta}_p^a = \beta_p^a - ig/2$ and $\tilde{\beta}_p^b = \beta_p^b + i\alpha_b/2$ are the associated complex-valued wavenumbers of the unperturbed modes, β_p^a and β_p^b are real-valued modal wavenumbers for the A and B waveguides respectively, g is the modal net-gain coefficient of the active region in the A (PIM) waveguide, α_b is the loss coefficient of the B (NIM) waveguide, and ω is the angular frequency. The quantities $\mathbf{e}_a(x,y)$ and $\mathbf{e}_b(x,y)$ are the unperturbed transverse mode profiles for each waveguide in isolation. The approximation is made that the unperturbed modes match the actual mode profiles and are orthogonal. These approximations have previously allowed for insightful modeling of evanescently coupled PIM and NIM waveguide structures [52].

Making the substitutions $\beta_a \equiv \beta_p^a$ and $\beta_b \equiv \beta_p^b$ where $\beta_a = 2\pi n_a/\lambda_0$ is the wavenumber of the A waveguide n_a is the effective refractive index of the A waveguide, and $\beta_b = 2\pi n_b/\lambda_0$ is the wavenumber of the B waveguide n_b is the effective refractive index of the B waveguide, and λ_0 is the wavelength, yields:

$$\mathbf{E}_A(x,y,z) = a(z)\mathbf{e}_a(x,y)e^{i\tilde{\beta}_a z}, \tag{5.3a}$$

$$\mathbf{E}_B(x,y,z) = b(z)\mathbf{e}_b(x,y)e^{i\tilde{\beta}_b z}. \tag{5.3b}$$

The electric-field amplitudes in the PIM and NIM waveguides can be written in a rotated frame given by $\mathbf{E}_A(z) = a(z)e^{-i\Delta\tilde{\beta}z}$ and $\mathbf{E}_B(z) = b(z)e^{i\Delta\tilde{\beta}z}$, respectively, where A & B are the slowly varying complex-field amplitudes of a relative rotating frame, and $\Delta\tilde{\beta} = (\tilde{\beta}_a - \tilde{\beta}_b)/2$ is the detuning parameter. By doing so, the rotated-frame electric-field expressions become:

$$\mathbf{E}_A(x,y,z) = a(z)e^{-i\Delta\tilde{\beta}z}\mathbf{e}_a(x,y)e^{i\bar{\beta}z}, \tag{5.4a}$$

$$\mathbf{E}_B(x,y,z) = b(z)e^{i\Delta\tilde{\beta}z}\mathbf{e}_b(x,y)e^{i\bar{\beta}z}, \tag{5.4b}$$

where $\bar{\beta} = (\beta_a + \beta_b)/2$.

The coupled-mode equations (CMEs) for the PIM-NIM structure can be written from Eq. (2.17) as

$$\frac{da}{dz} = i\,\mathrm{sgn}(\mathbb{S}_a)\kappa_{np}b(z)e^{-i2\Delta\tilde{\beta}z}, \tag{5.5a}$$

$$\frac{db}{dz} = i\,\mathrm{sgn}(\mathbb{S}_b)\kappa_{pn}a(z)e^{i2\Delta\tilde{\beta}z}, \tag{5.5b}$$

where sgn returns the sign associated with the direction of modal power flow. Resolving the sgn function and moving the resulting sign to the left-hand side results in:

$$\frac{da}{dz} = i\kappa_{np}b(z)e^{-i2\Delta\tilde{\beta}z}, \tag{5.6a}$$

$$-\frac{db}{dz} = i\kappa_{pn}a(z)e^{i2\Delta\tilde{\beta}z}. \tag{5.6b}$$

The coupled-mode equations for the optical-field amplitudes A and B within the PIM-NIM structure are written using rotating frames as:

$$\frac{da}{dz} = \left(i\Delta\beta + \frac{g}{2}\right) a + i\kappa_{np} b, \tag{5.7a}$$

$$-\frac{db}{dz} = \left(i\Delta\beta - \frac{\alpha_b}{2}\right) b + i\kappa_{pn} a, \tag{5.7b}$$

where $\Delta\beta = (\beta_a - \beta_b)/2$ is the real valued waveguide wavenumber detuning, g is the net gain coefficient of the PIM, α_b is the loss coefficient of the NIM, and κ_{pn} and κ_{np} are the coupling coefficients for coupling into the NIM and PIM, respectively. It is assumed that the anisotropy of each waveguide is small, a common assumption for coupled-mode equations and for previous modeling work in PIM-NIM couplers [51]–[53].

These coupled-mode equations are similar in form to those of a traditional DFB laser as seen in Eq. 2.79, whose counter-propagating A and B field amplitudes traverse a *single* waveguide and are coupled via a diffraction grating [72], [80]. One significant difference is that for the traditional DFB laser, the detuning parameter $\Delta\beta = \beta_a - \beta_\Lambda$ where β_a is the wavenumber of both optical modes, $\beta_\Lambda = \pi/\Lambda$ is the Bragg wavenumber, and Λ is the period of the diffraction grating. Also, since the counter-propagating modes traverse the *same* active waveguide, they each experience the gain coefficient g [i.e., $\alpha_b \rightarrow -g$ in Eq. (5.7b)]. For the PIM-NIM structure, the exclusive appearance of g or α_b in either equation results in important sum and difference expressions that govern the resonant amplification and lasing behavior.

Evanescent Coupling Coefficients

The coupling coefficients for evanescent-coupling in the PIM-NIM CMEs above consider the alternate waveguide as the region of perturbation. The change in relative permittivity $\Delta\bar{\varepsilon}$

is due to the sending-mode's waveguide perturbation as:

$$\Delta\bar{\varepsilon} = \bar{\varepsilon}_s - \bar{\varepsilon}_1, \tag{5.8}$$

where $\bar{\varepsilon}_s$ is the relative permittivity of the sending-mode's waveguide and $\bar{\varepsilon}_1$ is the relative permittivity of the cladding. These values are both constant across the transverse mode profile coordinates x and y and can be pulled out of the double integral. In general, $\bar{\varepsilon} = n^2$ where n is the refractive index, the coupling coefficient expression of Eq. (2.21) becomes:

$$\kappa_{sr} = \frac{\omega\varepsilon_0(n_s^2 - n_1^2)}{2} \int\limits_{-\infty}^{\infty} \int\limits_{-\infty}^{\infty} \mathbf{e}_s(x,y) \cdot \mathbf{e}_r^*(x,y)\; dy\; dx. \tag{5.9}$$

The evanescent-coupling coefficients for the PIM-NIM then become:

$$\kappa_{pn} = \frac{\omega\varepsilon_0(n_p^2 - n_1^2)}{2} \iint_A \mathbf{e}_p(x,y) \cdot \mathbf{e}_n^*(x,y) dx\; dy \tag{5.10a}$$

$$\kappa_{np} = \frac{\omega\varepsilon_0(n_n^2 - n_1^2)}{2} \iint_B \mathbf{e}_n(x,y) \cdot \mathbf{e}_p^*(x,y) dx\; dy, \tag{5.10b}$$

where $n_{(p,n)}$ is the constant material refractive index of the respective waveguide, n_1 is the refractive index of the cladding, ω is the angular frequency, ε_0 is the permittivity of free space, A is the region bounded by the A waveguide, and B is the region bounded by the B waveguide. For a negative-index material, both the permittivity ε and the permeability μ are negative resulting in a material-index of refraction for the NIM waveguide that is also negative [81].

5.3 Analytic Solution

5.3.1 General Solution

As the coupled mode equations in Eq. (5.7) are written in their rotated-frame form, they can be rewritten in a matrix notation as:

$$\frac{d\vec{v}}{dz} = i\mathbb{A}\vec{v}, \tag{5.11}$$

where

$$\mathbb{A} = \begin{bmatrix} \Delta\beta - ig/2 & \kappa_{np} \\ -\kappa_{pn} & -(\Delta\beta - i\alpha_b/2) \end{bmatrix}, \tag{5.12}$$

$\vec{v} = [A \;\; B]^\dagger$, and † is the matrix transpose function.

The eigenvalues $q_\pm$ of the coupled-mode equations describe the behavior of the PIM-NIM structure and are solved as the roots of the characteristic polynomial

$$q^2 + pq + r = 0, \tag{5.13}$$

where $p = -(a+d),\ r = (ad - bc),\ a = \Delta\beta - ig/2,\ b = \kappa_{np},\ c = \kappa_{pn},$ and $d = -(\Delta\beta - i\alpha_b/2)$, and are given as:

$$q_+ = \frac{\delta}{4} + i\sqrt{\left(\Delta\beta - i\frac{\sigma}{4}\right)^2 - \kappa^2}, \tag{5.14a}$$

$$q_- = \frac{\delta}{4} - i\sqrt{\left(\Delta\beta - i\frac{\sigma}{4}\right)^2 - \kappa^2}, \tag{5.14b}$$

where

$$\kappa = \sqrt{\kappa_{pn}\kappa_{np}}, \qquad \sigma = g - \alpha_b, \qquad \delta = g + \alpha_b, \tag{5.15}$$

The quantity σ is the *round-trip* gain coefficient for light that propagates down the full length of the PIM waveguide followed by a return trip down the full length of the

NIM waveguide (without evanescent coupling throughout). The quantity δ is the disparity from transparency and equals zero only for passive, lossless waveguides. Compared to the eigenvalues of a traditional DFB laser [72], [80], $\sigma/2$ takes the place of the traditional DFB gain coefficient, the δ term is entirely new, and κ is due to evanescent coupling instead of diffraction.

The eigenvalues given by Eq. (5.14a) and Eq. (5.14b) form the following general solutions of the amplitudes a and b:

$$a(\zeta) = a_1 e^{q_+ L\zeta} + a_2 e^{q_- L\zeta}, \tag{5.16a}$$

$$b(\zeta) = b_1 e^{q_+ L\zeta} + b_2 e^{q_- L\zeta}, \tag{5.16b}$$

where $\zeta = z/L$ is the normalized longitudinal spatial coordinate and $A_1, A_2, B_1,$ and B_2 are constant coefficients.

5.3.2 Electric-Field, Power, Transmittivity, and Reflectivity Expressions

Amplification of optical power between the ends of the PIM waveguide is studied by disallowing an optical signal in the NIM waveguide at $z = L$; i.e., $b(\zeta = 1) = 0$. Applying this boundary condition after substituting the eigenvalue Eq. (5.14a) and Eq. (5.14b) into the amplitude Eq. (5.16a) and Eq. (5.16b) yields:

$$a(\zeta) = -\frac{2B_1 e^{(\delta L/4)\zeta}}{e^{-i\tilde{\eta}L}\kappa_{pn}L}\left[\tilde{\psi}L\sinh\left(i\tilde{\eta}L(\zeta-1)\right) + \tilde{\eta}L\cosh\left(i\tilde{\eta}L(\zeta-1)\right)\right], \tag{5.17a}$$

$$b(\zeta) = \frac{2B_1 e^{(\delta L/4)\zeta}}{e^{-i\tilde{\eta}L}}\sinh\left(i\tilde{\eta}L(\zeta-1)\right), \tag{5.17b}$$

where the following quantities do not depend on the disparity δ:

$$\tilde{\eta} = \sqrt{\psi^2 - \kappa^2}, \qquad \tilde{\psi} = \Delta\beta - i\frac{\sigma}{4}. \tag{5.18}$$

The field amplitudes at the ends of the PIM-NIM structure are determined by a substitution of the appropriate value of ζ:

$$a(\zeta = 0) = \frac{2B_1}{e^{-i\tilde{\eta}L}\kappa_{pn}L}\left[\tilde{\psi}L\sinh\left(i\tilde{\eta}L\right) - \tilde{\eta}L\cosh\left(i\tilde{\eta}L\right)\right], \tag{5.19a}$$

$$a(\zeta = 1) = -\frac{2B_1 e^{\delta L/4}\tilde{\eta}L}{e^{-i\tilde{\eta}L}\kappa_{pn}L}, \tag{5.19b}$$

$$b(\zeta = 0) = -\frac{2B_1}{e^{-i\tilde{\eta}L}}\sinh\left(i\tilde{\eta}L\right). \tag{5.19c}$$

The transmittivity T and reflectivity R expressions are found from the ratio of field amplitudes as follows:

$$t = \frac{a(\zeta = 1)}{a(\zeta = 0)} = \frac{-e^{(\delta L/4)}\,\tilde{\eta}L}{\tilde{\psi}L\sinh\left(i\tilde{\eta}L\right) - \tilde{\eta}L\cosh\left(i\tilde{\eta}L\right)}, \tag{5.20a}$$

$$r = \frac{b(\zeta = 0)}{a(\zeta = 0)} = \frac{-\kappa_{pn}L\sinh\left(i\tilde{\eta}L\right)}{\tilde{\psi}L\sinh\left(i\tilde{\eta}L\right) - \tilde{\eta}L\cosh\left(i\tilde{\eta}L\right)}, \tag{5.20b}$$

$$T = |t|^2 = \frac{e^{(\delta L/2)}\left|\tilde{\eta}L\right|^2}{\left|\tilde{\psi}L\sinh\left(i\tilde{\eta}L\right) - \tilde{\eta}L\cosh\left(i\tilde{\eta}L\right)\right|^2}, \tag{5.21a}$$

$$R = |r|^2 = \frac{\left|\kappa_{pn}L\right|^2\left|\sinh\left(i\tilde{\eta}L\right)\right|^2}{\left|\tilde{\psi}L\sinh\left(i\tilde{\eta}L\right) - \tilde{\eta}L\cosh\left(i\tilde{\eta}L\right)\right|^2}. \tag{5.21b}$$

5.3.3 Transcendental Lasing Conditions

The threshold and detuning of lasing modes for DFB resonators can be obtained by deeper consideration of the transmittivity expression [80]. Eq. (5.21a) for T becomes infinite when its denominator becomes zero, which happens in the non-trivial case when

$$\tilde{\psi}_{th}L\sinh\left(i\tilde{\eta}_{th}L\right) = \tilde{\eta}_{th}L\cosh\left(i\tilde{\eta}_{th}L\right), \tag{5.22}$$

where the subscripts explicitly indicate that the quantities $\tilde{\psi}$ and $\tilde{\eta}$ are at their lasing-threshold values. Expanding the square of Eq. (5.22), applying Eqs. (5.18), and applying the identity $\cosh^2 x - \sinh^2 x = 1$ yields, after some manipulation,

$$\frac{\sigma_{th}L}{4} + i\Delta\beta_{th}L = \pm i\kappa L\cosh\left(i\tilde{\eta}_{th}L\right). \tag{5.23}$$

Substitution of Eq. (5.23) back into Eq. (5.22) ultimately generates the following transcendental equation relating $\tilde{\eta}_{th}L$ to the normalized coupling coefficient κL:

$$\kappa L = \pm\frac{\tilde{\eta}_{th}L}{\sinh\left(i\tilde{\eta}_{th}L\right)}. \tag{5.24}$$

The solution pairs $\{\kappa L,\ \tilde{\eta}_{th}L\}$ are found from Eq. (5.24) by a numerical solver. These solution pairs are then fed into the right-hand side of Eq. (5.23), and the real and imaginary parts are used to determine $\sigma_{th}L$ and $\Delta\beta_{th}L$. This approach to studying lasing also shows that the lasing threshold $\sigma_{th}L$ is independent of the NIM loss $\mathscr{L}$ and disparity δ.

5.4 Conclusion

This chapter presented the coupled-mode equations and associated solutions for the second novel type of DFB laser, one based on the evanescent coupling between an active PIM waveguide and a lossy NIM waveguide. The eigenvalues of the new structure are reminiscent of the traditional uniform-grating DFB laser where the gain coefficient g has been replaced with a round-trip gain coefficient σ and the diffraction based coupling coefficient has been replaced instead with an evanescent coupling process. An entirely new term δ representing the disparity from transparency acts as a bias to the eigenvalue solution.

6. Single-Mode DFB Lasing using a Coupled NIM Waveguide: Lasing Behavior

6.1 Introduction

This chapter leverages the model and solutions introduced in Chapter 5 to study lasing behavior. Traditional distributed feedback (DFB) lasers rely on a first-order diffraction grating to provide feedback along the length of the active region; as was previously shown, this DFB produces a degenerate pair of lowest-threshold lasing modes, one on either side of the photonic bandgap [80]. To realize a *single-mode* laser, this degeneracy is commonly broken by shifting the mode spectrum via, for example, fabricating a phase shift in the grating or optimizing facet reflectivities.

It will be shown that the photonic bandgap and single-mode lasing behavior of the coupled NIM waveguide structure depends on the difference between modal wavenumbers of the PIM and NIM waveguides, its behavior is not restricted by a grating-defined Bragg wavenumber; single-mode operation is predicted by tailoring the wavenumber difference to avoid mode degeneracy.

6.2 Photonic Bandgap

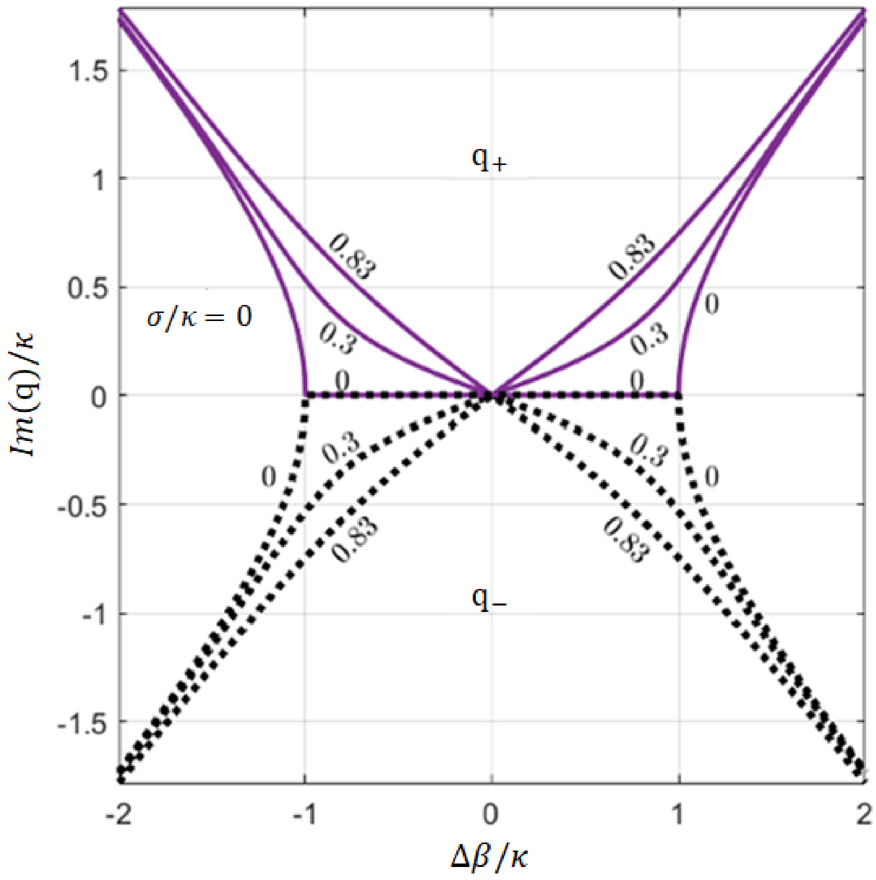

Figure 6.1 Dispersion relations for the q_+ eigenvalue (upper half-plane) and q_- eigenvalue (lower half-plane) for $\sigma/\kappa = 0, 0.3$, and $2.5/3$. A photonic bandgap is clearly seen for $\sigma = 0$, and the disparity quantity δ does not impact the dispersion relations.

The imaginary portion of either eigenvalue $q_\pm$ directly reveals the photonic bandgap nature of the active PIM-NIM structure, as illustrated in Fig. 6.1 for several values of the round-trip gain σ normalized by κ. For $\sigma = 0$, a photonic bandgap occurs between $\Delta\beta = \pm\kappa$ wherein optical fields exponentially decay in the direction of the Poynting vector. Increasing σ produces oscillatory, decaying optical fields within the photonic bandgap, as is the case for the traditional DFB laser [80]. For the PIM-NIM structure, the dispersion relations are independent of the disparity quantity δ.

For a PIM-NIM DFB laser, $\Delta\beta = (\beta_a - \beta_b)/2$, and so the center of the photonic bandgap is achieved only if the modal wavenumbers β_a and β_b are equal. Thus, $\Delta\beta$ is akin to that of the traditional photonic *directional coupler* despite the occurrence of DFB along the hybrid PIM-NIM structure.

6.3 Transmittivity

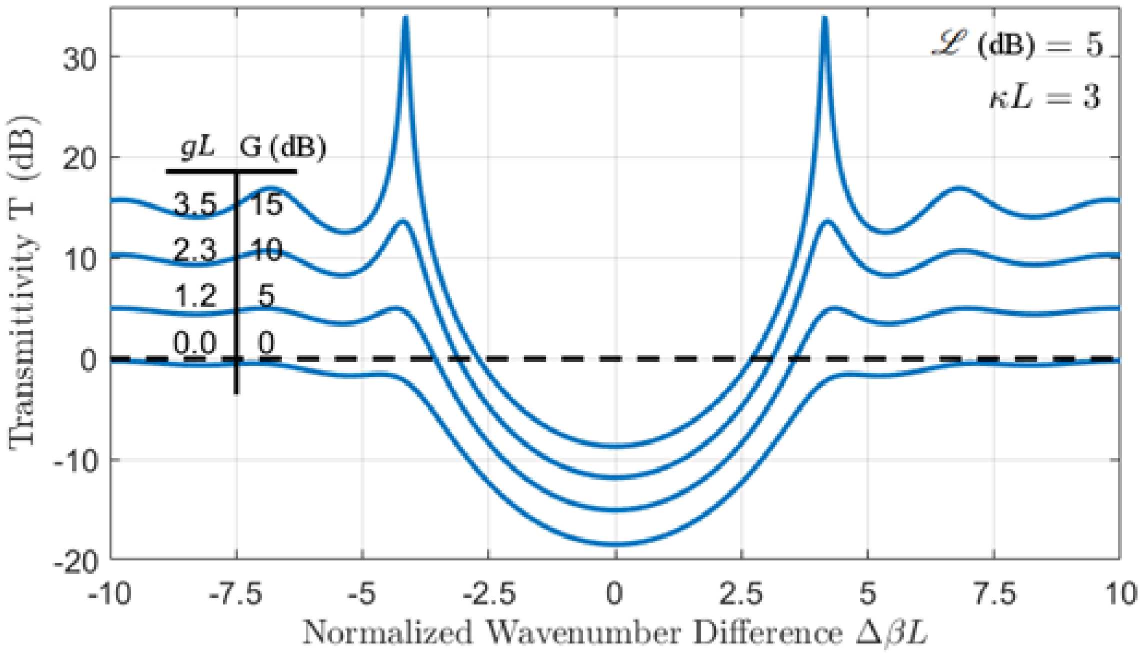

Figure 6.2 Resonant optical-amplification route to lasing threshold. The transmittivity spectrum for a NIM loss of 5 dB reveals resonant optical amplification at the edges of the photonic bandgap. Increasing the PIM gain increases the strength of the resonances. Transmittivity far from $\Delta\beta L = 0$ is at the level of an uncoupled, active PIM.

The transmittivity T of an active PIM-NIM structure is shown in Fig. 6.2 for $\kappa L = 3$ and a NIM-waveguide loss $\mathscr{L} = 5$ dB, where $\mathscr{L} = \exp(-\alpha L)$. Resonant amplification is exhibited on either side of the photonic bandgap. The resonances increase in strength as the value of the PIM-waveguide gain $G = \exp(gL)$ is increased, and their peak transmittivity exceeds 30 dB for G = 15 dB. For detuning $\Delta\beta L$ away from the photonic bandgap, the dissimilarity in modal wavenumbers prevents efficient coupling between waveguides; this inefficiency results in a transmittivity T that is equivalent to the gain G of the uncoupled

PIM waveguide.

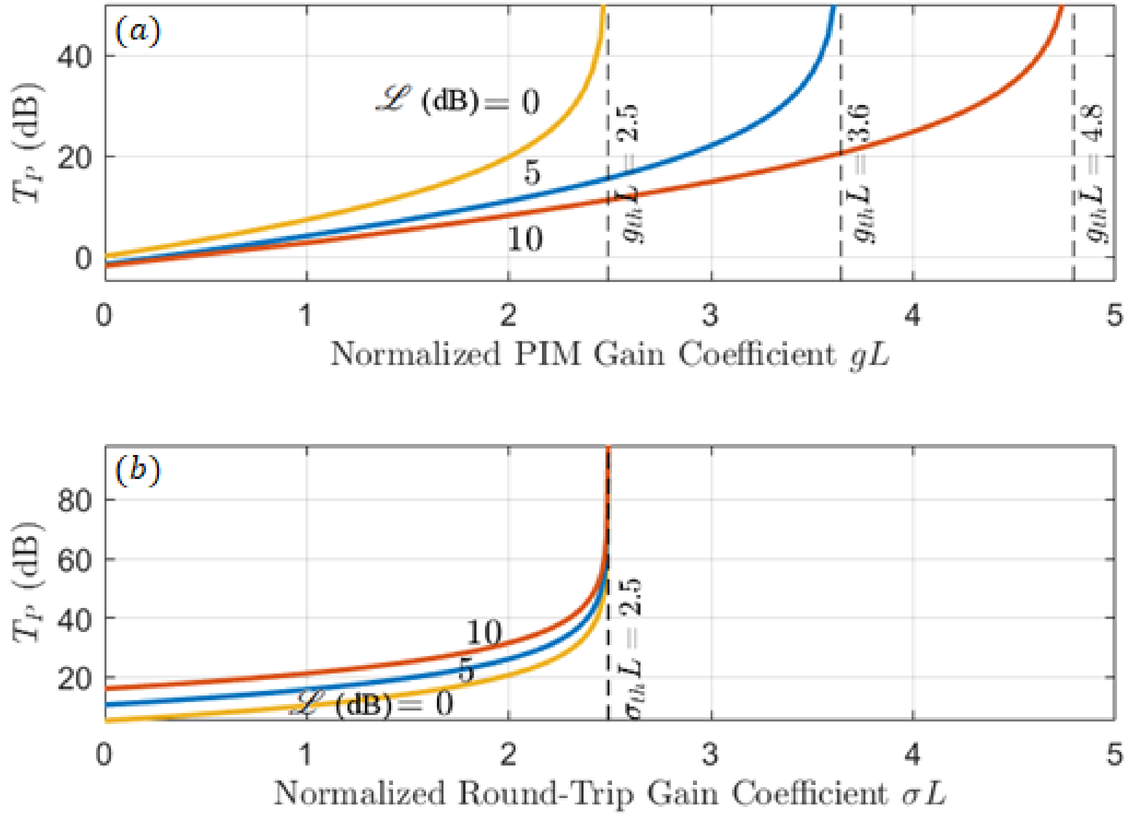

Figure 6.3 Ramping structure gain reveals lasing threshold. (a) Peak transmittivity T_P as a function of PIM gain coefficient gL for three values of NIM loss $\mathscr{L}$. Lasing threshold $g_{th}L$ occurs when $T_P = \infty$ and depends on the NIM loss. (b) T_P as a function of normalized round-trip gain $\sigma_{th}L$ is independent of the NIM loss $\mathscr{L}$ and disparity δ. $\kappa L = 3$ for all parts.

Lasing is achieved when the transmittivity peak T_p reaches infinity, physically corresponding to obtaining an optical output power without an optical input power [72]. The increase in T_p as a function of the normalized PIM gain coefficient gL is shown in Fig. 6.3(a) for $\kappa L = 3$ and several values of NIM loss $\mathscr{L}$. T_p is seen to increase at a low rate for small gL and eventually rises in an extreme manner as gL approaches the lasing-threshold value $g_{th}L$. The threshold $g_{th}L$ increases as the NIM loss $\mathscr{L}$ increases.

The relation between lasing-threshold values across different NIM-loss cases is seen clearly when the peak transmittivity T_p is considered in terms of the round-trip gain σL. As shown in Fig. 6.3(b), the value of $\sigma_{th}L$ is the *same* regardless of the amount of the NIM loss $\mathscr{L}$. Since the disparity $\delta = \sigma + 2\alpha$ [from Eqs. (5.15)], each curve in Fig. 6.3(b) corresponds to a unique value of δL, and therefore the lasing threshold $\sigma_{th}L$ is independent of δL.

6.4 Mode Spectrum

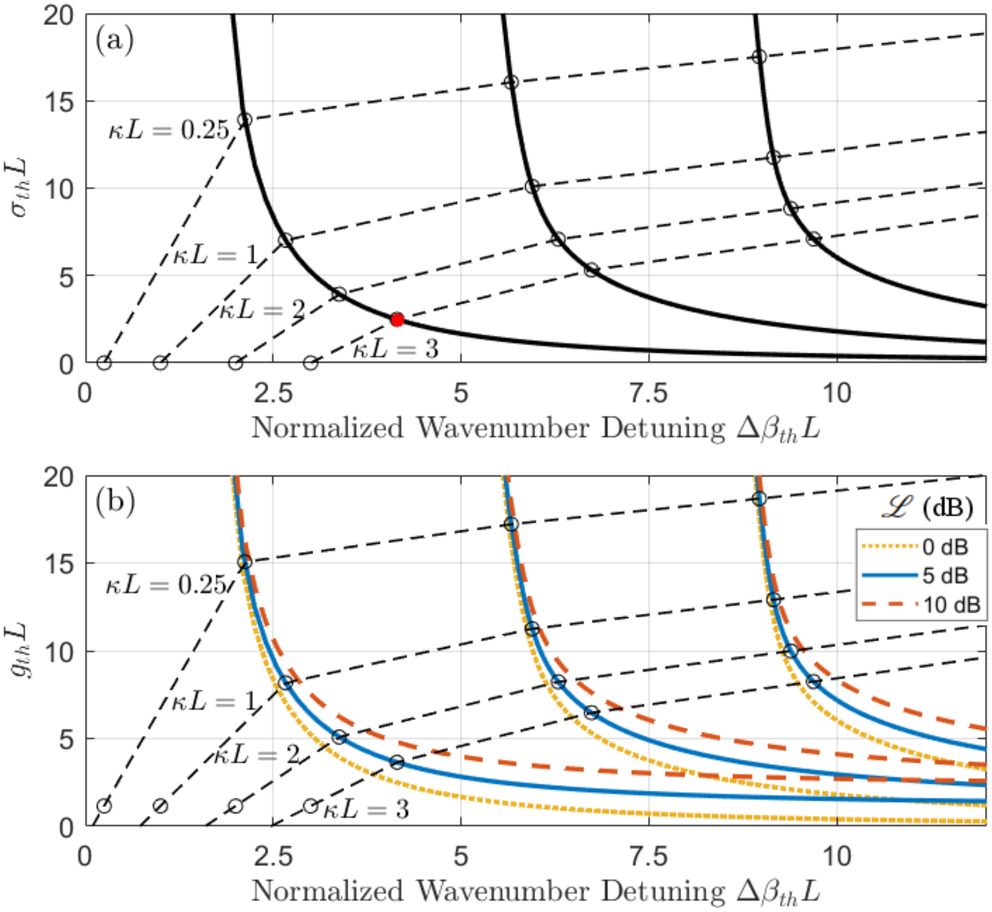

Figure 6.4 The lasing-mode spectrum as a function of coupling κL using transcendental Eqs. (5.23) and (5.24); the three lowest lasing-threshold modes are shown for positive $\Delta\beta_{th}L$ (symmetric modes for negative $\Delta\beta_{th}L$ not shown). (a) Lasing threshold $\sigma_{th}L$ and wavenumber detuning $\Delta\beta_{th}L$ solution pairs for specific coupling-coefficient values, several of which are highlighted using dashed lines. (b) Lasing threshold expressed as $g_{th}L$ and for three values of NIM loss $\mathscr{L}$, where $\mathscr{L} = 5$ dB has been used for the κL highlight lines.

The threshold values $\sigma_{th}L$ and $\Delta\beta_{th}L$ of the three lowest lasing-threshold modes are shown in Fig. 6.4(a), where only the curves for positive $\Delta\beta_{th}L$ are shown (a symmetric set occurs for negative $\Delta\beta_{th}L$). Each point on a mode curve is associated with a specific value of the normalized coupling coefficient κL, and constant-coupling examples across the mode spectra are indicated using dashed lines. The red solid marker in the figure represents the lasing threshold that limits the amplification behavior shown in Fig. 6.4(a). The impact of the NIM loss $\mathscr{L}$ can be made explicit by applying $g_{th} = \sigma_{th} + \alpha$ (from Eqs. (5.15)) to the data of Fig. 6.4(a). Doing so yields the threshold $g_{th}L$ and $\Delta\beta_{th}L$ pairs shown in Fig. 6.4(b); each lasing mode is now represented by multiple curves, one for each value of NIM loss.

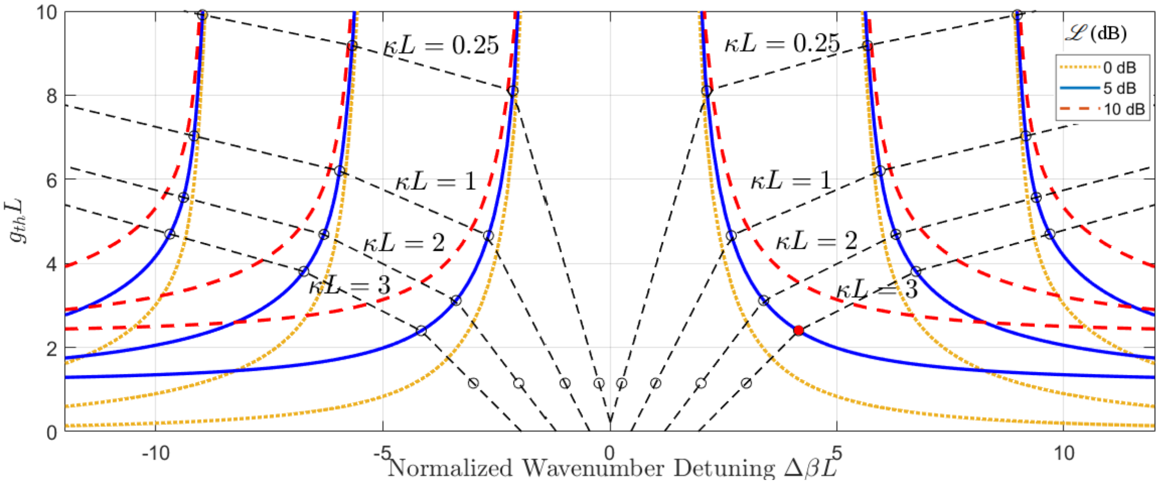

Figure 6.5 PIM-NIM DFB laser mode spectra as a function of normalized evanescent coupling κL and NIM loss $\mathscr{L}$. Mode degeneracy is broken by design of normalized detuning $\Delta\beta L$.

The full upper and lower sides of the lasing mode spectrum for the three value of NIM loss $\mathscr{L}$ is captured in Fig. 6.5. Although the shown lasing-threshold curves are similar in form to those of the traditional DFB laser [80], a significant difference in the behavior of either kind of DFB laser is rooted in the definition of $\Delta\beta_{th}L$. For a traditional DFB laser, $\Delta\beta = \beta - \frac{\pi}{\Lambda}$, and so the center of the photonic bandgap ($\Delta\beta L = 0$) is achieved when the free-space wavelength λ matches the Bragg wavelength $\lambda_B = 2n\Lambda$, where n is the modal index. Since the photonic bandgap spans only up to a couple of nanometers, the lowest lasing-threshold mode on either side of the photonic bandgap experiences similar gain, leading to the undesirable dual-lasing-mode nature of these devices [5], [80], [82].

For a PIM-NIM DFB laser, $\Delta\beta \propto \beta_a - \beta_b$, and so the *center* of the photonic bandgap ($\Delta\beta L = 0$) is achieved only if the modal wavenumbers β_a and β_b are equal; equivalently, since $\beta_a - \beta_b = \frac{2\pi}{\lambda}(n_a - n_b)$, the center of the photonic bandgap is achieved only if the modal indexes n_a and n_b are equal. Matching the wavenumbers to yield $\Delta\beta L = 0$ is commonly achieved in traditional directional couplers (DCs) made of two PIM waveguides [68]. For the PIM-NIM DFB laser, it may be possible to design the waveguides so that the wavenumbers *never* match over the gain spectrum. Doing so would force $\Delta\beta L$ to be solely positive or solely negative, thereby breaking the lasing-threshold mode degeneracy and giving rise to a single-mode laser.

6.5 Conclusion

A new method for achieving DFB lasing has been proposed and modeled based on the evanescent coupling between an active positive-index material (PIM) waveguide and a negative-index metamaterial (NIM) waveguide. In this hybrid structure, the opposing nature of the Poynting vector in either waveguide gives rise to DFB while the active PIM waveguide provides for optical gain.

Coupled-mode equations are formed for the lasing structure and closed-form solutions are derived. The eigenvalues of the second-order system demonstrate similarities to those of the traditional diffraction grating based DFB lasers but introduce the new quantity of disparity and update the definition of gain to include the round-trip gain and loss coefficients of the PIM and NIM waveguides respectively. Coupling occurs in the new lasing structure using an evanescent coupling process as opposed to a diffraction based process.

Closed form transmittivity solutions provide for gain and detuning threshold pairs which generate a mode spectrum reminiscent of a traditional uniform-grating DFB laser. These traditional lasers exhibit degenerate mode spectra which is broken by introducing non-uniformities into the diffraction grating, tuning facet reflectivity, or by part sampling and down selection.

Single-mode operation of the proposed NIM-PIM lasing structure is predicted by a means not available to traditional DFB lasers though a tailoring of waveguide wavenumber detuning. By designing the waveguide's refractive indexes such that the difference remains positive or negative across wavelength, $\Delta\beta L$ can be made to be one sided. Forcing the waveguide detuning to remain on one side of the mode spectrum breaks the lasing-mode degeneracy and results in single-mode lasing behavior. If the difference between refractive indexes can be made constant across wavelength, the single-mode broadband lasing may be realized.

The lasing threshold values are found by solving a transcendental equation which only depends upon coupling, detuning, and round-trip gain. Though the disparity term is entirely new it does not impact the threshold values of the structure.

7. Concluding Remarks

7.1 Overview

This dissertation introduces and explores two single-mode DFB lasing concepts, both of which are new to the field. One single-mode lasing concept is based on the offset alignment of multiple photonic bandgaps and the other is based on the counter-propagating nature of light in a negative-index material waveguide. Each concept is explored via mathematical models derived using coupled-mode theory. Closed-form analytic solutions are found for each concept using a combination of traditional mathematical techniques as well as a newly-developed solution process capable of handling the fourth-order coupled-mode equations. Furthermore, the expected performance of one lasing concept is predicted to out perform the industry standard $\lambda/4$-shifted DFB laser in both gain margin and longitudinal power flatness.

The work developed and presented in this dissertation is guide-star research at low technology readiness level. The predicted performance motivates further research; the established mathematical models and closed-form solutions are tools to aide in that work.

7.2 Single-Mode DFB Lasing using Photonic-Bandgap Alignment

Single-mode lasing for a dual-waveguide direct-Bragg, exchange-Bragg, and evanescently coupled distributed feedback structure is explored using coupled-mode equations. The lasing structure introduces a second coupled waveguide to the original single-waveguide uniform diffraction-grating laser introduced in Ref. [4]. This approach takes advantage of the exchange-Bragg photonic bandgap, created with the introduction of the second waveguide, to suppress the degenerate lasing mode and, by doing so, seeks to avoid the nonlinear effects introduced by a peaky longitudinal power profile such as seen in the ubiquitous $\lambda/4$-shifted DFB laser.

New fourth-order coupled mode equations are developed which describe waveguide mode interactions with the uniform diffraction grating and each waveguide. These CMEs consider the four independent coupling mechanisms, the four wavenumbers, the active-region gain, each waveguide loss, and the active-region refractive-index nonlinearity.

A new method is developed to arrive at solutions to the fourth-order CMEs, resulting in fully parameterized, normalized closed-form expressions of the lasing structures electromagnetic fields, longitudinal power profiles, and transmittivity and reflectivity responses. The derived solutions allow for the understanding of fundamental underlying physical principles of the lasing structure by enabling the observation of behaviors though isolated changes in well-defined model parameters. Confidence in this model is achieved because, through the proper selection of parameter values, the provided closed-form solutions can model a variety of two or four port, active or passive, and grating or gratingless structures.

The exchange-Bragg photonic bandgap PBG_χ can be aligned to the degenerate lasing mode through the proper selection of waveguide-wavenumber detuning $\Delta\beta_{ab}L$, resulting in single-mode lasing whose structure avoids the undesired phase shift associated with the $\lambda/4$-shifted DFB laser. This alignment can be accomplished even as Henry's alpha α_H

is introduced. Furthermore, the suppression strength of PBG_χ is controlled through the exchange-Bragg coupling value $\kappa_\chi L$, resulting in a single-mode laser capable of very high gain margin $\Delta\alpha L = 1.05$ and low longitudinal power-profile flatness $F = 0.017$.

Additionally, Exchange-Bragg coupling's impact on the competition between secondary lasing modes is revealed. Small values of $\kappa_\chi L$ are not sufficient to suppress the degenerate mode. Increasing the exchange-Bragg coupling coefficient serves to effectively suppress the degenerate mode, but, gives rise to a resonance that ultimately dominates as the secondary mode for high values of $\kappa_\chi L$. Viable exchange-Bragg coupling coefficient values are therefore bounded between these two extremes which are themselves dependent on the structure's direct-Bragg coupling and evanescent coupling strengths.

The model's inclusion of evanescent coupling demonstrates that single-mode lasing survives as $\kappa_e L$ is introduced; in some cases evanescent coupling can be used to improve on both gain margin and power flatness, and maintain consistent gain margin across a span of $\kappa_\chi L$. Furthermore, increasing $\kappa_e L$ serves to delay the unwanted mode associated with PBG_χ occurring at larger values of $\kappa_\chi L$ and extends the same-side secondary lasing-mode span. A structure with an evanescent coupling coefficient of $\kappa_e L = 0.25$ was shown to result in a single-mode laser with a best-in-class flatness of $F = 0.0006$ along with a gain margin of $\Delta\alpha L = 0.87$, both values exceeding those of the industry standard $\lambda/4$-shifted DFB laser ($F = 0.012$ & $\Delta\alpha L = 0.682$ for best flatness or $F = 0.215$ & $\Delta\alpha L = 0.735$ for best gain margin). Unlike current lasing structures where the minimum flatness and high gain margin occur for distinct direct-Bragg coupling values, the presented approach outperforms in both quantities simultaneously for the same optimized structure.

7.3 Single-Mode DFB Lasing Concept using a Coupled NIM Waveguide

Single-mode lasing for a structure which evanescently couples a lossy negative-index material (NIM) waveguide to a positive-index material (PIM) waveguide with gain is explored using coupled-mode equations. The Poynting vector associated with the NIM waveguide points in the direction opposite to its wavevector indicating power flow in opposition to the field direction of propagation. As with a traditional PIM-PIM directional coupler, optimal evanescent coupling occurs when detuning conditions are met. However, *unlike* the traditional PIM-PIM directional coupler, the counter-directional nature of the flow of power in the NIM waveguide establishes a feedback mechanism within the coupled PIM-NIM structure.

New second-order coupled mode equations are developed which describe each waveguide mode interactions. These CMEs consider the evanescent-coupling mechanisms, the two wavenumbers, the PIM's active-regions net gain, and the NIM waveguide's loss.

For the PIM-NIM DFB laser, the waveguide-wavenumber detuning $\Delta\beta \propto \beta_A - \beta_B$, and so the *center* of the photonic bandgap ($\Delta\beta L = 0$) is achieved only if the modal wavenumbers β_A and β_B are equal; equivalently, since $\beta_A - \beta_B = \frac{2\pi}{\lambda}(n_A - n_B)$, the center of the photonic bandgap is achieved only if the modal indexes n_A and n_B are equal. Matching the wavenumbers to yield $\Delta\beta L = 0$ is commonly achieved in traditional directional couplers (DCs) made of two PIM waveguides [68]. For the PIM-NIM DFB laser, it may be possible to design the waveguides so that the wavenumbers *never* match over the gain spectrum. Doing so would force $\Delta\beta L$ to be solely positive or negative, thereby breaking the lasing-threshold mode degeneracy and giving rise to a single-mode laser.

7.4 Future Work

Future work on the two novel lasing concepts can encompass extending the presented mathematical modeling research or pushing into higher TRL research activities through FDTD modeling, fabrication, or experimentation.

7.4.1 Facet Reflections

Reflections can occur at the facets of standalone structures. For both lasing structures, research may be performed to quantify and optimize on behaviors when facet reflections are non-zero valued. The grating phase at non-zero facet reflections alters the position of the dominant lasing mode and reduces the gain margin in traditional $\lambda/4$-shifted DFB lasers. In stand-alone devices, these reflections are typically mitigated through anti-reflection coatings or angled cuts at the laser facet edge.

7.4.2 Above-Threshold Operation

The mathematical modeling and behavior analysis of both lasing structures in this dissertation was performed at-threshold. Above-threshold analysis to understand the degradation in gain margin, side-mode suppression ratio, output optical power, and other behaviors would further characterize each lasing structure's performance expectations. Thermal effects and wavelength tunability could also be included in such a study.

7.4.3 FDTD Modeling, Fabrication, and Experiment

Future work, more readily for the single-mode lasing structure using photonic-bandgap alignment, may include the development of an experimental prototype. Initial prototypes could be pursued in a monolithic III-V material process such as InP or InGaAsP, however, longer-term heterogeneous integration with silicon-photonic platforms is desired. As a precursor to any such tapeout, a high-level design and simulation using a finite-difference time-domain (FDTD) method could be pursued to verify that available gain media, waveguide materials, and fabrication processes support the κ and $\Delta\beta$ values determined by this dissertations for single-mode operation. Furthermore, a study on the impact of material and process variance on waveguide wavenumber detuning and, ultimately, mode suppression could be considered. Detailed modeling and simulation of the various structures using the selected foundry process design kit (PDK) would build confidence and address first-level issues prior to experimental fabrication and test.

Future work for the PIM-NIM lasing structure may continue to explore the single-mode capability of the structure through the dispersion design of the NIM waveguide. A lower TRL experimental research effort in negative-index material waveguides could precede a prototype effort of the PIM-NIM lasing structure. Continued investment in the mathematical model is justifiable as NIM waveguides continue to mature.

7.4.4 $\mathscr{PT}$-Symmetry

The dual-waveguide feedback structure of the PIM-NIM supports both coupling and independent gain and loss subsystems as required of $\mathscr{PT}$-symmetric structures. These parameters are captured by its CMEs 2×2 Hamiltonian matrix $\mathbb{A}$. Further research exploring the PIM-NIM concept may yield interesting behaviors when considering both unbroken (in dynamic equilibrium) or broken (not in dynamic equilibrium) states around the structure's exceptional point. The unique properties captured by the PIM-NIM mathematical model presented in this dissertation have already proven to be compelling for the $\mathscr{PT}$-symmetry research community [83], [84].

Bibliography

[1] H. Ghafouri-Shiraz, *Distributed Feedback Laser Diodes and Optical Tunable Filters*. John Wiley & Sons, 2003.

[2] A. Takada, T. Sugie, and M. Saruwatari, "High-speed picosecond optical pulse compression from gain-switched 1.3-μm distributed feedback-laser diode (DFB-LD) through highly dispersive single-mode fiber," *Journal of Lightwave Technology*, vol. 5, no. 10, pp. 1525–1533, 1987.

[3] *400G ZR & ZR+: A systems engineering company's perspective*, `https://www.precisionot.com/400gzr_systems_engineering/`, Accessed: 2023-03-24.

[4] H. Kogelnik and C. Shank, "Coupled-wave theory of distributed feedback lasers," *Journal of Applied Physics*, vol. 43, no. 5, pp. 2327–2335, 1972.

[5] H. Haus and C. Shank, "Antisymmetric taper of distributed feedback lasers," *IEEE Journal of Quantum Electronics*, vol. 12, no. 9, pp. 532–539, 1976.

[6] T. Dupont, L. Grenouillet, A. Chelnokov, and P. Viktorovitch, "Contradirectional coupling between III–V stacks and silicon-on-insulator corrugated waveguides for laser emission by distributed feedback effect," *IEEE Photonics Technology Letters*, vol. 22, no. 19, pp. 1413–1415, 2010.

[7] T. Dupont, L. Grenouillet, A. Chelnokov, and P. Viktorovitch, "III-V on Si distributed-feedback lasers based on exchange bragg contradirectionnal coupling," in *Proceedings of ECIO*, 2010.

[8] F. J. Blanco, M. Agirregabiria, J. Berganzo, *et al.*, "Microfluidic-optical integrated CMOS compatible devices for label-free biochemical sensing," *Journal of Micromechanics and Microengineering*, vol. 16, no. 5, p. 1006, 2006.

[9] M. Hochberg, N. C. Harris, R. Ding, *et al.*, "Silicon photonics: The next fabless semiconductor industry," *IEEE Solid-State Circuits Magazine*, vol. 5, no. 1, pp. 48–58, 2013.

[10] S. Kanazawa, T. Fujisawa, K. Takahata, *et al.*, "Flip-chip interconnection lumped-electrode EADFB laser for 100-Gb/s/λ transmitter," *IEEE Photonics Technology Letters*, vol. 27, no. 16, pp. 1699–1701, 2015.

[11] T. Shi, H. Wang, R. Meng, L. Xu, T. Wang, and W. Zheng, "Flip-chip bonded evanescently coupled III-V-on-Si single-mode laser with slotted feedback structure," *IEEE Photonics Technology Letters*, vol. 33, no. 14, pp. 739–742, 2021.

[12] S. Stankovic, R. Jones, M. N. Sysak, J. M. Heck, G. Roelkens, and D. Van Thourhout, "Hybrid III–V/Si distributed-feedback laser based on adhesive bonding," *IEEE Photonics Technology Letters*, vol. 24, no. 23, pp. 2155–2158, 2012.

[13] S. Keyvaninia, S. Verstuyft, L. Van Landschoot, *et al.*, "Heterogeneously integrated III-V/silicon distributed feedback lasers," *Optics Letters*, vol. 38, no. 24, pp. 5434–5437, 2013.

[14] T. Okumura, T. Maruyama, M. Kanemaru, S. Sakamoto, and S. Arai, "Single-mode operation of GaInAsP/InP-membrane distributed feedback lasers bonded on silicon-on-insulator substrate with rib-waveguide structure," *Japanese Journal of Applied Physics*, vol. 46, no. 12L, p. L1206, 2007.

[15] Y. Wang, Z. Lu, M. Ma, *et al.*, "Compact broadband directional couplers using subwavelength gratings," *IEEE Photonics Journal*, vol. 8, no. 3, pp. 1–8, 2016.

[16] A. Gallet, G. Levaufre, A. Accard, *et al.*, "Hybrid III-V on silicon integrated distributed feedback laser and ring resonator for 25 Gb/s future access networks," *Journal of Lightwave Technology*, vol. 36, no. 8, pp. 1498–1502, 2018.

[17] J. Durel, T. Ferrotti, A. Chantre, *et al.*, "Realization of back-side heterogeneous hybrid III-V/Si DBR lasers for silicon photonics," in *Integrated Optics: Devices, Materials, and Technologies XX*, SPIE, vol. 9750, 2016, pp. 106–117.

[18] T. L. Thiessen, "Backside-integrated III-V-on-silicon lasers and modulators," Ph.D. dissertation, University of Toronto (Canada), 2021.

[19] B. Haq, S. Kumari, J. Zhang, *et al.*, "Micro-transfer-printed III-V-on-silicon distributed feedback lasers," in *2020 Optical Fiber Communications Conference and Exhibition (OFC)*, IEEE, 2020, pp. 1–3.

[20] B. Haq, J. R. Vaskasi, J. Zhang, *et al.*, "Micro-transfer-printed III-V-on-silicon C-band distributed feedback lasers," *Optics Express*, vol. 28, no. 22, pp. 32 793–32 801, 2020.

[21] J. Zhang, B. Haq, J. O'Callaghan, *et al.*, "Transfer-printing-based integration of a III-V-on-silicon distributed feedback laser," *Optics Express*, vol. 26, no. 7, pp. 8821–8830, 2018.

[22] P. J. De Groot, "A review of selected topics in interferometric optical metrology," *Reports on Progress in Physics*, vol. 82, no. 5, p. 056 101, 2019.

[23] M. U. Khan, S. A. A. Zaidi, A. Ishtiaq, S. U. R. Bukhari, S. Samer, and A. Farman, "A comparative survey of lidar-slam and lidar based sensor technologies," in *2021 Mohammad Ali Jinnah University International Conference on Computing (MAJICC)*, IEEE, 2021, pp. 1–8.

[24] J. He, B. Xu, X. Xu, C. Liao, and Y. Wang, "Review of femtosecond-laser-inscribed fiber bragg gratings: Fabrication technologies and sensing applications," *Photonic Sensors*, vol. 11, pp. 203–226, 2021.

[25] S. A. Al-Gailani, M. F. M. Salleh, A. A. Salem, *et al.*, "A survey of free space optics (fso) communication systems, links, and networks," *IEEE Access*, vol. 9, pp. 7353–7373, 2020.

[26] A. Bernatskyi and M. Sokolovskyi, "History of military laser technology development in military applications," *History of science and technology*, vol. 12, no. 1, pp. 88–113, 2022.

[27] R. Soref, "The past, present, and future of silicon photonics," *IEEE Journal of Selected Topics in Quantum electronics*, vol. 12, no. 6, pp. 1678–1687, 2006.

[28] G. Roelkens, J. Van Campenhout, J. Brouckaert, *et al.*, "III-V/Si photonics by die-to-wafer bonding," *Materials Today*, vol. 10, no. 7-8, pp. 36–43, 2007.

[29] B. Shi, B. Song, A. A. Taylor, S. S. Brunelli, and J. Klamkin, "Selective area heteroepitaxy of low dislocation density antiphase boundary free GaAs microridges on flat-bottom (001) Si for integrated silicon photonics," *Applied Physics Letters*, vol. 118, no. 12, p. 122 106, 2021.

[30] Z. Wang, B. Tian, M. Pantouvaki, *et al.*, "Room-temperature InP distributed feedback laser array directly grown on silicon," *Nature Photonics*, vol. 9, no. 12, pp. 837–842, 2015.

[31] W. Bogaerts and L. Chrostowski, "Silicon photonics circuit design: Methods, tools and challenges," *Laser & Photonics Reviews*, vol. 12, no. 4, p. 1 700 237, 2018.

[32] M. Lončar, T. Doll, J. Vučković, and A. Scherer, "Design and fabrication of silicon photonic crystal optical waveguides," *Journal of Lightwave Technology*, vol. 18, no. 10, p. 1402, 2000.

[33] L. Chrostowski and M. Hochberg, *Silicon Photonics Design: From Devices to Systems*. Cambridge University Press, 2015.

[34] M. Okai, N. Chinone, H. Taira, and T. Harada, "Corrugation-pitch-modulated phase-shifted DFB laser," *IEEE Photonics Technology Letters*, vol. 1, no. 8, pp. 200–201, 1989.

[35] H. Soda, Y. Kotaki, H. Sudo, H. Ishikawa, S. Yamakoshi, and H. Imai, "Stability in single longitudinal mode operation in GaInAsP/InP phase-adjusted DFB lasers," *IEEE Journal of Quantum Electronics*, vol. 23, no. 6, pp. 804–814, 1987.

[36] G. Agrawal and A. Bobeck, "Modeling of distributed feedback semiconductor lasers with axially-varying parameters," *IEEE Journal of Quantum Electronics*, vol. 24, no. 12, pp. 2407–2414, 1988.

[37] C. Henry, "Theory of the linewidth of semiconductor lasers," *IEEE Journal of Quantum Electronics*, vol. 18, no. 2, pp. 259–264, 1982.

[38] H. Ghafouri-Shiraz, B. Lo, and C. Chu, "Structural dependence of three-phase-shift distributed feedback semiconductor laser diodes at threshold using the transfer matrix method," *Semiconductor Science and Technology*, vol. 9, no. 5, p. 1126, 1994.

[39] J. B. Boavida, J. A. Morgado, and C. A. Fernandes, "Optimisation of a corrugation-pitch-modulated DFB laser structure with inhomogeneous coupling coefficient for stable single longitudinal mode operation," *The European Physical Journal Applied Physics*, vol. 48, no. 3, 2009.

[40] J. M. Miloszewski, M. Wartak, P. Weetman, and O. Hess, “Analysis of linewidth enhancement factor for quantum well structures based on ingaasn/gaas material system,” *Journal of Applied Physics*, vol. 106, no. 6, p. 063 102, 2009.

[41] Z. Zhang, D. Jung, J. C. Norman, W. W. Chow, and J. E. Bowers, “Linewidth enhancement factor in InAs/GaAs quantum dot lasers and its implication in isolator-free and narrow linewidth applications,” *IEEE Journal of Selected Topics in Quantum Electronics*, vol. 25, no. 6, pp. 1–9, 2019.

[42] G. Morthier and P. Vankwikelberge, *Handbook of distributed feedback laser diodes*. Artech House, 2013.

[43] P. W. Epperlein, *Semiconductor Laser Engineering, Reliability and Diagnostics: A Practical Approach to High Power and Single Mode Devices*. John Wiley & Sons, 2013.

[44] Q. Li and K. M. Lau, “Epitaxial growth of highly mismatched III-V materials on (001) silicon for electronics and optoelectronics,” *Progress in Crystal Growth and Characterization of Materials*, vol. 63, no. 4, pp. 105–120, 2017.

[45] Y. Han, Z. Yan, W. K. Ng, Y. Xue, K. S. Wong, and K. M. Lau, “Bufferless 1.5 μm III-V lasers grown on Si-photonics 220 nm silicon-on-insulator platforms,” *Optica*, vol. 7, no. 2, pp. 148–153, 2020.

[46] Y. Shi, M. Pantouvaki, J. Van Campenhout, *et al.*, “Loss-coupled DFB nano-ridge laser monolithically grown on a standard 300-mm Si wafer,” *Optics Express*, vol. 29, no. 10, pp. 14 649–14 657, 2021.

[47] G. Morthier, K. David, P. Vankwikelberge, and R. Baets, “A new DFB-laser diode with reduced spatial hole burning,” *IEEE Photonics Technology Letters*, vol. 2, no. 6, pp. 388–390, 1990.

[48] G. Morthier and R. Baets, “Design of index-coupled DFB lasers with reduced longitudinal spatial hole burning,” *Journal of Lightwave Technology*, vol. 9, no. 10, pp. 1305–1313, 1991.

[49] M. Okai, “Spectral characteristics of distributed feedback semiconductor lasers and their improvements by corrugation-pitch-modulated structure,” *Journal of Applied Physics*, vol. 75, no. 1, pp. 1–29, 1994.

[50] B. A. Tennant and D. N. Maywar, “Single-mode distributed feedback lasing using photonic bandgaps to suppress degenerate modes,” *Optics Letters*, vol. 47, no. 13, pp. 3367–3370, 2022.

[51] A. Alu and N. Engheta, “An overview of salient properties of planar guided-wave structures with double negative (DNG) and single negative (SNG) layers,” in *Negative-Refraction Metamaterials: Fundamental Principles and Applications*, G. V. Eleftheriades and K. G. Balmain, Eds., John Wiley & Sons, 2005, ch. 9, pp. 339–375.

[52] N. M. Litchinitser, I. R. Gabitov, and A. I. Maimistov, “Optical bistability in a nonlinear optical coupler with a negative index channel,” *Physical Review Letters*, vol. 99, no. 11, p. 113 902, 2007.

[53] W. Yan, L. Shen, Y. Yuan, and T. J. Yang, "Interaction between negative and positive index medium waveguides," *Journal of Lightwave Technology*, vol. 26, no. 21, pp. 3560–3566, 2008.

[54] V. G. Veselago, "The electrodynamics of substances with simultaneously negative values of and μ," *Soviet Physics Uspekhi*, vol. 10, no. 4, p. 509, 1968.

[55] I. V. Shadrivov, A. A. Sukhorukov, and Y. S. Kivshar, "Guided modes in negative-refractive-index waveguides," *Physical Review E*, vol. 67, no. 5, p. 057 602, 2003.

[56] T. Amemiya, S. Yamasaki, M. Tanaka, *et al.*, "Demonstration of slow-light effect in silicon-wire waveguides combined with metamaterials," *Optics Express*, vol. 27, no. 10, pp. 15 007–15 017, 2019.

[57] T. Amemiya, T. Kanazawa, S. Yamasaki, and S. Arai, "Metamaterial waveguide devices for integrated optics," *Materials*, vol. 10, no. 9, p. 1037, 2017.

[58] D. Marcuse, "Coupled-mode theory for anisotropic optical waveguides," *The Bell System Technical Journal*, vol. 54, no. 6, pp. 985–995, 1975.

[59] D. Marcuse, "Directional couplers made of nonidentical asymmetric slabs. part II: Grating-assisted couplers," *Journal of Lightwave Technology*, vol. 5, no. 2, pp. 268–273, 1987.

[60] R. März and H. Nolting, "Spectral properties of asymmetrical optical directional couplers with periodic structures," *Optical and Quantum Electronics*, vol. 19, no. 5, pp. 273–287, 1987.

[61] H. A. Haus and Y. Lai, "Narrow-band distributed feedback reflector design," *Journal of Lightwave Technology*, vol. 9, no. 6, pp. 754–760, 1991.

[62] H. A. Haus and Y. Lai, "Narrow-band optical channel-dropping filter," *Journal of Lightwave Technology*, vol. 10, no. 1, pp. 57–62, 1992.

[63] R. R. Syms, "Optical directional coupler with a grating overlay," *Applied Optics*, vol. 24, no. 5, pp. 717–726, 1985.

[64] R. Syms, "Improved coupled-mode theory for codirectionally and contradirectionally coupled waveguide arrays," *JOSA A*, vol. 8, no. 7, pp. 1062–1069, 1991.

[65] T. Erdogan, "Optical add–drop multiplexer based on an asymmetric Bragg coupler," *Optics Communications*, vol. 157, no. 1-6, pp. 249–264, 1998.

[66] R. Syms, "Multiple-waveguide distributed feedback lasers," *IEEE Journal of Quantum Electronics*, vol. 22, no. 3, pp. 411–418, 1986.

[67] B. A. Tennant, R. Ara, A. Atwiri, G. P. Agrawal, N. M. Litchinitser, and D. N. Maywar, "Distributed feedback lasing based on a negative-index metamaterial waveguide," *Optics Letters*, vol. 44, no. 18, pp. 4586–4589, 2019.

[68] D. L. Lee, *Electromagnetic Principles of Integrated Optics*. Wiley, 1986.

[69] J. Hong and W. Huang, "Coupled-waveguide exchange-Bragg resonator filters: Coupled-mode analysis with loss and gain," *Journal of Lightwave Technology*, vol. 11, no. 2, pp. 226–233, 1993.

[70] J.-L. Archambault, P. S. J. Russell, S. Barcelos, P. Hua, and L. Reekie, “Grating-frustrated coupler: A novel channel-dropping filter in single-mode optical fiber,” *Optics Letters*, vol. 19, no. 3, pp. 180–182, 1994.

[71] P. Yeh and H. Taylor, “Contradirectional frequency-selective couplers for guided-wave optics,” *Applied Optics*, vol. 19, no. 16, pp. 2848–2855, 1980.

[72] D. N. Maywar and G. P. Agrawal, “Transfer-matrix analysis of optical bistability in DFB semiconductor laser amplifiers with nonuniform gratings,” *IEEE Journal of Quantum Electronics*, vol. 33, no. 11, pp. 2029–2037, 1997.

[73] D. Marcuse, *Theory of Dielectric Optical Waveguides*. Elsevier, 2013.

[74] W. Shi, X. Wang, C. Lin, *et al.*, “Silicon photonic grating-assisted, contra-directional couplers,” *Optics Express*, vol. 21, no. 3, pp. 3633–3650, 2013.

[75] P. Pesic, *Abel’s Proof*. MIT press Cambridge, MA, 2003.

[76] S. Neumark, *Solution of Cubic and Quartic Equations*. Elsevier, 2014.

[77] A. W. Fang, E. Lively, Y.-H. Kuo, D. Liang, and J. E. Bowers, “A distributed feedback silicon evanescent laser,” *Optics Express*, vol. 16, no. 7, pp. 4413–4419, 2008.

[78] S. Srinivasan, A. W. Fang, D. Liang, J. Peters, B. Kaye, and J. E. Bowers, “Design of phase-shifted hybrid silicon distributed feedback lasers,” *Optics Express*, vol. 19, no. 10, pp. 9255–9261, 2011.

[79] G. P. Agrawal, *Lightwave Technology: Telecommunication Systems*. John Wiley & Sons, 2005.

[80] H. Kogelnik and C. Shank, “Coupled-wave theory of distributed feedback lasers,” *Journal of Applied Physics*, vol. 43, no. 5, pp. 2327–2335, 1972.

[81] P. W. Milonni, *Fast light, slow light and left-handed light*. CRC Press, 2004.

[82] T. Matsuoka, Y. Yoshikuni, and G. Motosugi, “Dependence of single-longitudinal-mode probability on DFB laser facet structure,” *Electronics Letters*, vol. 21, no. 24, pp. 1151–1152, 1985.

[83] S. V. Raja, A. Govindarajan, A. Mahalingam, and M. Lakshmanan, “Tailoring inhomogeneous PT-symmetric fiber-Bragg-grating spectra,” *Physical Review A*, vol. 101, no. 3, p. 033 814, 2020.

[84] A. Govindarajan, B. A. Malomed, and M. Lakshmanan, “Tunable nonlinear spectra of anti-directional couplers,” *Optics Letters*, vol. 45, no. 7, pp. 1918–1921, 2020.